DISSERTATIONES
CHIMICAE
UNIVERSITATIS
TARTUENSIS
247

SILVER JUVANEN

Non-precious metal catalysts based on biomass-derived carbon for electrocatalytic applications

DISSERTATIONES CHIMICAE UNIVERSITATIS TARTUENSIS
247

DISSERTATIONES CHIMICAE UNIVERSITATIS TARTUENSIS
247

SILVER JUVANEN

Non-precious metal catalysts based on biomass-derived carbon for electrocatalytic applications

UNIVERSITY OF TARTU
Press
1632

Institute of Chemistry, Faculty of Science and Technology, University of Tartu, Estonia

The dissertation is accepted for the commencement of the degree of *Doctor Philosophiae* in Chemistry on 9 June 2026 by the Council of Institute of Chemistry, Faculty of Science and Technology, University of Tartu.

Supervisors: Assoc. Prof Ave Sarapuu
Institute of Chemistry, University of Tartu, Estonia

Prof. Kaido Tammeveski
Institute of Chemistry, University of Tartu, Estonia

Opponent: Dr. Dulce M. Morales
Engineering and Technology Institute Groningen (ENTEG), University of Groningen, The Netherlands

Commencement: 3 September 2026 at 10:15, Ravila 14a, Tartu (Chemicum)

ISSN 1406-0299 (print) ISSN 2806-2159 (pdf)
ISBN 978-9908-57-263-5 (print) ISBN 978-9908-57-264-2 (pdf)

Copyright: Silver Juvanen, 2026

University of Tartu Press
www.tyk.ee

TABLE OF CONTENTS

1. LIST OF ORIGINAL PUBLICATIONS 6
2. ABBREVIATIONS AND SYMBOLS 8
3. INTRODUCTION 10
4. LITERATURE OVERVIEW 12
   - 4.1. Polymer electrolyte fuel cells 12
   - 4.2. Rechargeable zinc-air batteries 14
   - 4.3. Non-precious metal electrocatalysts 17
   - 4.4. Electrochemical characterization methods 20
5. EXPERIMENTAL 22
   - 5.1. Synthesis of biomass-derived electrocatalysts 22
     - 5.1.1. Synthesis of electrocatalysts from glucose 22
     - 5.1.2. Synthesis of electrocatalysts from rapeseed press cake 22
     - 5.1.3. Ionothermal synthesis of electrocatalysts 24
   - 5.2. Physicochemical characterization 25
   - 5.3. Electrochemical characterization 27
     - 5.3.1. RDE and RRDE experiments 27
     - 5.3.2. GDE experiments 28
     - 5.3.3. RZAB experiments 28
     - 5.3.4. AEMFC experiments 29
6. RESULTS AND DISCUSSION 31
   - 6.1. Electrocatalysts derived from glucose 31
   - 6.2. Electrocatalysts derived from rapeseed press cake 37
     - 6.2.1. Electrocatalysts synthesized using DCDA and metal salts .. 37
     - 6.2.2. Templated electrocatalysts for AEMFC 43
     - 6.2.3. Templated electrocatalysts for RZAB 49
     - 6.2.4. Ionothermally synthesized electrocatalysts for RZAB 60
     - 6.2.5. Ionothermally synthesized electrocatalysts for AEMFC 72
7. SUMMARY 78
8. REFERENCES 80
9. SUMMARY IN ESTONIAN 96
10. ACKNOWLEDGEMENTS 98
11. PUBLICATIONS 99
12. CURRICULUM VITAE 184
13. ELULOOKIRJELDUS 186

1. LIST OF ORIGINAL PUBLICATIONS

This thesis consists of six original articles, which are listed below. The articles are referred to by Roman numerals I–VI.

[I] **S. Juvanen**, A. Sarapuu, S. Vlassov, M. Kook, V. Kisand, M. Käärik, A. Treshchalov, J. Aruväli, J. Kozlova, A. Tamm, J. Leis, K. Tammeveski, Iron-Containing Nitrogen-Doped Carbon Nanomaterials Prepared via NaCl Template as Efficient Electrocatalysts for the Oxygen Reduction Reaction. ChemElectroChem 8 (12) (2021) 2288–2297.

[II] **S. Juvanen**, A. Sarapuu, M. Mooste, M. Käärik, U. Mäeorg, A. Kikas, V. Kisand, J. Kozlova, A. Treshchalov, J. Aruväli, J. Leis, A. Tamm, K. Tammeveski, Electroreduction of Oxygen on Iron- and Cobalt-Containing Nitrogen-Doped Carbon Catalysts Prepared from the Rapeseed Press Cake. J. Electroanal. Chem. 920 (2022) 116599.

[III] **S. Juvanen**, A. Sarapuu, K. Kisand, M. Käärik, A. Kikas, J. Kozlova, A. Treshchalov, J. Aruväli, J. Leis, V. Kisand, K. Kukli, K. Tammeveski, Templated Rapeseed-Press-Cake-Based Materials as Efficient Oxygen Reduction Reaction Electrocatalysts. ACS Sustain. Resour. Manag. 2 (3) (2025) 446–454.

[IV] **S. Juvanen**, A. Sarapuu, M. Käärik, A. Kikas, J. Kozlova, A. Treshchalov, J. Aruväli, J. Leis, V. Kisand, K. Kukli, K. Tammeveski, Investigation of Rechargeable Zinc-Air Battery Performance Using a Bifunctional Biomass-Derived Catalyst Material for the Air Electrode. J. Energy Storage 148 (2026) 120293.

[V] **S. Juvanen**, A. Sarapuu, M. Käärik, A. Kikas, J. Kozlova, A. Treshchalov, J. Aruväli, J. Leis, V. Kisand, K. Kukli, K. Tammeveski, Bifunctional Bimetallic Biomass-Derived Electrocatalyst Materials for Usage as Air Electrode Catalysts in Rechargeable Zinc-Air Batteries, Energy & Fuels 40 (20) (2026) 11116–11127.

[VI] **S. Juvanen**, A. Sarapuu, M. Käärik, A. Kikas, J. Kozlova, M. Kõiv, A. Treshchalov, J. Aruväli, J. Leis, V. Kisand, K. Kukli, K. Tammeveski, Biomass-derived catalyst materials prepared via ionothermal synthesis for oxygen reduction reaction in anion-exchange membrane fuel cells (manuscript).

Author's contributions:

Paper I: The author was responsible for the synthesis of the electrocatalysts, electrochemical characterization, data analysis, and initial interpretation of the results. The author also participated in the writing of the manuscript.

Paper II: The author was responsible for the synthesis of the electrocatalysts, electrochemical characterization (except for fuel cell measure-

ments), data analysis, and initial interpretation of the results. The author also participated in the writing of the manuscript.

Paper III: The author was responsible for the synthesis of the electrocatalysts, electrochemical characterization (except for fuel cell measurements), data analysis, and overall interpretation of the results. The author was also primarily responsible for writing the manuscript.

Paper IV: The author was responsible for the synthesis of the electrocatalysts, electrochemical characterization, rechargeable zinc-air battery measurements, data analysis, and overall interpretation of the results. The author was also primarily responsible for writing the manuscript.

Paper V: The author was responsible for the synthesis of the electrocatalysts, electrochemical characterization, rechargeable zinc-air battery measurements, data analysis, and overall interpretation of the results. The author was also primarily responsible for writing the manuscript.

Paper VI: The author was responsible for the synthesis of the electrocatalysts, electrochemical characterization, fuel cell measurements, data analysis, and overall interpretation of the results. The author was also primarily responsible for writing the manuscript.

2. ABBREVIATIONS AND SYMBOLS

AEI	anion-exchange ionomer
AEM	anion-exchange membrane
AEMFC	anion-exchange membrane fuel cell
at%	atom percentage
BET	Brunauer-Emmett-Teller
BF	bright field
CA	chronoamperometry
C_{dl}	double-layer capacitance
C_{O2}	concentration of dissolved oxygen
DCDA	dicyandiamide
DFT	density functional theory
D_{O2}	diffusion coefficient of oxygen
EDX	energy-dispersive X-ray spectroscopy
ΔE	potential difference between $E_{1/2}$ and $E_{j=10}$
E_0	standard potential
$E_{1/2}$	half-wave potential
$E_{j=10}$	potential at a current density of 10 mA cm^{-2}
E_{onset}	onset potential
F	Faraday constant
FC	fuel cell
GC	glassy carbon
GDE	gas diffusion electrode
GDL	gas diffusion layer
g-C_3N_4	graphitic carbon nitride
HAADF	high-angle annular dark field
HOR	hydrogen oxidation reaction
HR-STEM	high-resolution scanning transmission electron microscopy
I/C	ionomer-to-carbon ratio
I_d	disk current
I_r	ring current
j	current density
j_d	diffusion-limited current density
j_k	kinetic current density
K-L	Koutecký-Levich
MEA	membrane-electrode assembly
M-N_x	metal-nitrogen coordinated sites
M@N-C	metal-containing sites surrounded by N-doped carbon shells
MP-AES	microwave plasma atomic emission spectroscopy
n	number of electrons transferred
N	collection efficiency of the platinum ring electrode
NLPM	normal liters per minute
OCV	open circuit voltage

OER	oxygen evolution reaction
ORR	oxygen reduction reaction
PEMFC	proton-exchange membrane fuel cell
PGM	platinum-group metal
P_{max}	peak power density
PSD	pore size distribution
PTFE	polytetrafluoroethylene
QSDFT	quenched solid density functional theory
RDE	rotating disk electrode
RH	relative humidity
RHE	reversible hydrogen electrode
RRDE	rotating ring-disk electrode
RZAB	rechargeable zinc-air battery
S_{BET}	specific surface area according to BET theory
SSA	specific surface area
SCE	saturated calomel electrode
SEM	scanning electron microscopy
STEM	scanning transmission electron microscopy
v	scan rate
V_{tot}	total pore volume
V_{μ}	micropore volume
wt%	weight percentage
XPS	X-ray photoelectron spectroscopy
XRD	X-ray diffraction
ZAB	zinc-air battery
ν	kinematic viscosity
ω	electrode rotation rate

3. INTRODUCTION

In pursuit of a sustainable future, the European Commission has set a target of achieving net-zero emissions of greenhouse gases by 2050 through the European Green Deal [1]. This requires a significant transformation of the current fossil-fuel-based energy production system. Electrolytically produced hydrogen using renewable electricity resources such as solar and wind power is considered a key priority in achieving this goal [2,3]. Hydrogen fuel cells (FCs) are devices that can convert hydrogen and oxygen from air directly into electricity, producing heat and water as byproducts, thereby offering a sustainable alternative to fossil fuels.

Of the multiple types of FCs, proton-exchange membrane fuel cell (PEMFC) technology is the most mature and already commercially used in fuel cell electric vehicles such as the Toyota Mirai [4,5]. Anion-exchange membrane fuel cell (AEMFC) technology is not yet commercially viable, although significant progress has been made during the last decade [5,6]. The wider adoption of both types of FCs is hindered by the scarcity and high price of platinum-group metals (PGMs), with platinum being the most widely used catalyst material [5,7]. It is possible to use PGM-free cathode catalysts for AEMFCs, as these materials tend to have higher activity and stability in alkaline conditions compared to the acidic environment of PEMFCs [8,9]. Highly active PGM-free catalysts have been described in the literature, but achieving optimal performance combined with high stability in practical AEMFCs remains challenging [5,7,10].

Another requirement for the wider use of renewable electricity is inexpensive and sustainable energy storage. While solar and wind power are generally cheap, the production of electricity from intermittent sources does not always coincide with demand, which leads to wide daily variations in price [11]. Battery storage is one possible option to smooth out the price curve, but current lithium-based battery technologies are expensive, with prices over 100$ per kWh of storage [11]. Rechargeable zinc-air battery (RZAB) technology is a promising option for cheaper energy storage. RZABs require a bifunctional air electrode catalyst for optimal performance, which needs to be active for both charging and discharging the battery [12]. Like FCs, current state-of-the-art bifunctional catalysts contain platinum and ruthenium, which are, once again, too expensive for the commercialization of RZABs [13].

It is possible to use biomass as a precursor for producing PGM-free electrocatalysts, which is attractive from the viewpoints of cost and waste valorization [14,15]. The purpose of the research presented in this thesis was to develop and characterize highly active and inexpensive biomass-derived PGM-free electrocatalysts for usage as cathode catalysts in AEMFCs [I–III, VI], as well as bifunctional air electrode catalysts for usage in RZABs [IV, V]. For this purpose, glucose [I] and hot-pressed rapeseed press cake [II–VI] were used as biomass sources for the preparation of active electrocatalysts for the oxygen reduction reaction (ORR) or bifunctional electrocatalysts active for both ORR and oxygen evolution reaction (OER). The catalysts were synthesized by pyrolysis of the

corresponding biomass source together with nitrogen and transition metal sources. Additionally, the effect of adding magnesium-based template precursors into the pyrolysis mixture was investigated, with the aim of optimizing the porous structure and corresponding electrochemical performance of the electrocatalysts [III–VI]. The electrocatalytic performance and nanostructure of the catalysts were thoroughly investigated using various electrochemical and physical characterization methods. Finally, the performance of the electrocatalysts in AEMFC [II, III, VI] and RZAB [IV, V] test systems was investigated.

4. LITERATURE OVERVIEW

4.1. Polymer electrolyte fuel cells

Fuel cells are devices that convert chemical energy from fuels into electricity. In that sense, their working principle is similar to that of batteries, except that they work continuously, as long as an external fuel supply is provided [16]. There is a wide variety of fuel cell technologies, including proton-exchange membrane fuel cells (PEMFCs), anion-exchange membrane fuel cells (AEMFCs), solid-oxide fuel cells, phosphoric acid fuel cells, molten carbonate fuel cells, direct methanol fuel cells, and others [16,17]. Depending on the type of fuel cell, different fuels like hydrogen, methanol, and natural gas (methane) may be used [17]. Additionally, it is possible to transform hydrocarbon-containing fuels into a stream of hydrogen, carbon dioxide, and/or carbon monoxide, with the product composition depending on the specific reforming reaction, after which the resulting gas mixture can be used as a fuel [18]. An additional benefit of fuel cells is their high efficiency, which can reach up to 60–70%, compared to 30–40% of internal combustion engines [19]. For transportation applications like vehicles, low-temperature (less than 100 °C) polymer electrolyte fuel cells, such as PEMFCs and AEMFCs, are preferable due to their low operating temperatures and rapid start-up [19]. Polymer electrolyte fuel cells consist of an ion exchange membrane sandwiched between catalyst-coated gas diffusion layers (GDLs) (Figure 1). The membrane-electrode assembly (MEA) is placed between plates that contain flow fields for the transport of reactants and water vapor, and which also provide electrical contact to the external load.

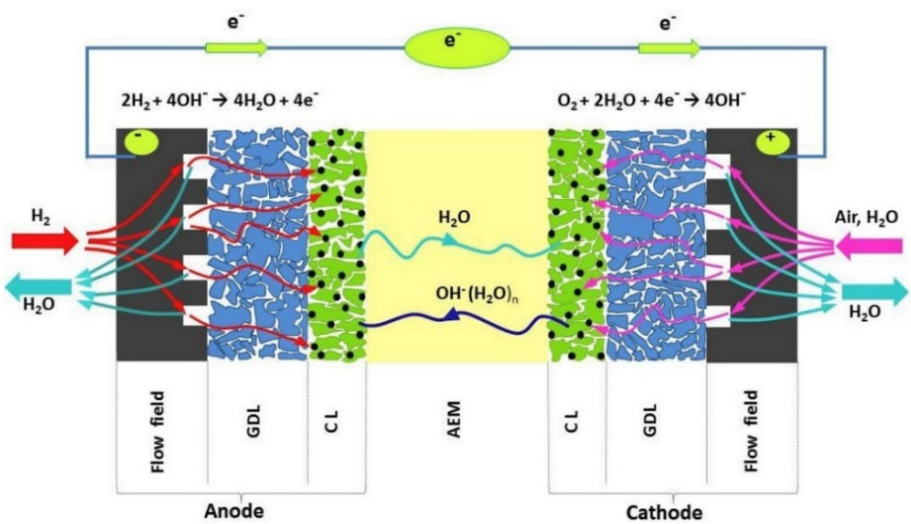

Figure 1. Schematic of AEMFC, adapted from ref. [20].

For fuel cells using hydrogen as a fuel, the overall reaction appears simple – two equivalents of hydrogen react with one equivalent of oxygen, forming two equivalents of water:

$$2H_2 + O_2 \rightarrow 2H_2O \quad (1)$$

This reaction is separated into half-reactions occurring on the anode and the cathode of the fuel cell. On the FC cathode, the electrochemical oxygen reduction reaction (ORR) occurs. In alkaline aqueous media, which are relevant for AEMFC, the ORR mainly proceeds via a 4-electron pathway [6]:

$$O_2 + 2H_2O + 4e^- \rightarrow 4OH^- \qquad E_0 = 0.401\ V \quad (2)$$

The ORR can also proceed via a 2-electron pathway:

$$O_2 + H_2O + 2e^- \rightarrow OH^- + HO_2^- \qquad E_0 = -0.065\ V \quad (3)$$

Reaction (3) may be followed by the reduction of the hydroperoxide anion (2×2 electron pathway):

$$HO_2^- + H_2O + 2e^- \rightarrow 3OH^- \qquad E_0 = 0.867\ V \quad (4)$$

or by the disproportionation of the hydroperoxide anion:

$$2HO_2^- \rightarrow 2OH^- + O_2 \quad (5)$$

The 2-electron pathway is generally undesirable due to the detrimental effects of the hydroperoxide anion on practical fuel cell devices, as it may react with the components of the fuel cell [6]. Furthermore, less energy can be obtained from the 2-electron reaction than from the 4-electron reaction (2). The relative amount of HO_2^- anions produced is specific to the catalyst and the operating conditions. For example, it has been shown that HO_2^- anions may be further reduced to OH^- during HO_2^- diffusion through thick catalyst layers [21].
On the anode of AEMFCs, the hydrogen oxidation reaction (HOR) occurs [22]:

$$H_2 + 2OH^- \rightarrow 2H_2O + 2e^- \qquad E_0 = -0.83\ V \quad (6)$$

In alkaline media, one mole of water is consumed at the cathode (2) for every two moles produced at the anode (6). This has major implications for practical AEMFC devices, which must carefully balance the water conditions on both the anode and cathode. Overproducing water on the anode or using highly humidified gases may lead to cell flooding, which impedes gas transport and therefore reduces the fuel cell performance [23]. Dry conditions may limit the availability of reactants and/or dry out the anion-exchange membrane (AEM), again lowering the performance of the fuel cell. This water management issue is a major complication for the practical operation of AEMFC devices [23,24].

The ORR is kinetically sluggish, leading to high overpotential and requiring highly active electrocatalysts [10,25]. In contrast, the HOR typically exhibits much lower overpotential, which is why researchers have generally focused on improving ORR electrocatalysts [25,26]. However, HOR is *ca* two orders of magnitude slower in alkaline than in acidic media, and PGM-based HOR

catalysts are still required in AEMFCs [9,27]. As ORR remains the rate-limiting reaction, the development of efficient and cost-effective ORR catalysts is crucial. Biomass-derived catalysts have been successfully used as cathode catalysts for AEMFCs in numerous studies, as summarized in Table 1.

Table 1. AEMFC performance of biomass-derived cathode catalyst materials.

Catalyst	Biomass source	P_{max}, mW cm^{-2}	Ref.
FeCoNCR-a	Rapeseed press cake	131	[II]
FeNCR-MgAc-3-1	Rapeseed press cake	355	[III]
MnIC FeMnIC FeIC	Rapeseed press cake	222 267 289	[VI]
SNBC12	Bamboo stems	217	[28]
Zn/Fe$_{SA}$-PC/950/NH3	Pig blood	352	[29]
Fe-N-C	Sucrose	118	[30]
Fe–N-PDC-HA	Peat	1060	[31]
L FeMn	Lignin	261	[32]
Fe-N-(FeTC-R0.5)	Mimosa tannin	242	[33]
FeNC(Mg)	Lignin	615	[34]
FeCoNC(Mg)	Lignin	833	[34]
LNOC-900	Corn-cob-derived lignin	1050	[35]
SiFe–N–C	Pinecones	250	[36]
Co_3O_4@NC	Neem leaves	43	[37]

4.2. Rechargeable zinc-air batteries

Rechargeable zinc-air batteries (RZAB) use oxygen from the air and zinc as reactants, producing electrical energy via the reaction [38–40]:

$$2Zn + O_2 \rightarrow 2ZnO \qquad E_0 = 1.65\ V \qquad (7)$$

RZABs generally consist of a zinc electrode and a catalyst-coated GDL serving as the air electrode, separated by an alkaline electrolyte (Figure 2) [41].

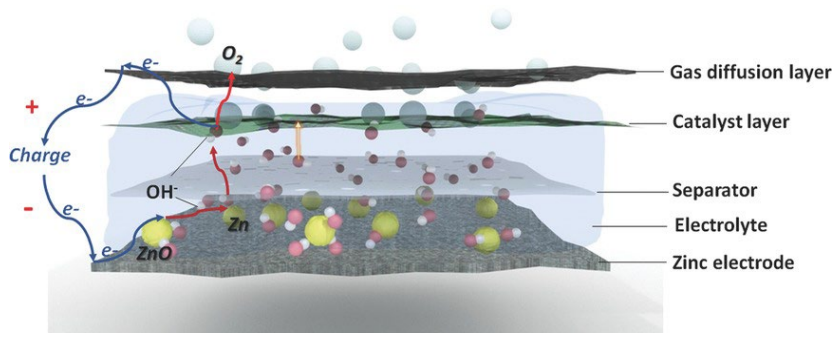

Figure 2. Schematic of RZAB, adapted from ref. [41].

The main attraction of RZABs is their high theoretical specific capacity of 820 mAh g^{-1}, as zinc is the only reactant stored in the battery, while oxygen is supplied from the air [42]. Zinc is a low-cost and widely available metal, making it a cost-effective alternative to lithium-based batteries [43]. Primary (non-rechargeable) zinc-air batteries (ZABs) have been used in applications such as hearing aids, railway signals, marker lights, and navigation instruments [43,44]. At the zinc anode, the following reactions occur [45,46]:

$$Zn + 4OH^- \rightarrow Zn(OH)_4^{2-} + 2e^- \qquad E_0 = -1.26\ V \tag{8}$$

$$Zn(OH)_4^{2-} \rightarrow ZnO\ (type\ I) + H_2O + 2OH^- \tag{9}$$

$$Zn + 2OH^- \rightarrow ZnO\ (type\ II) + H_2O + 2e^- \tag{10}$$

Zinc reacts with hydroxide anions at low current densities or low zincate concentrations, forming the water-soluble zincate anion (8). Type I zinc oxide starts to precipitate on the Zn electrode at higher zincate concentrations according to reaction (9); this oxide is porous and allows the electrolyte to be in contact with the zinc electrode [45,46]. When hydroxide anions are locally depleted near the zinc electrode, for example at high discharge rates, a direct reaction leading to the formation of type II zinc oxide occurs according to reaction (10). This quickly passivates the surface of the zinc electrode and stops the battery from working [45]. RZABs generally use 6 M KOH as the electrolyte, with additives like zinc oxide and zinc acetate to improve the corrosion resistance of the Zn electrode [47]. Therefore, the alkaline ORR reactions (2–5) described in Section 4.1 occur at the RZAB air electrode during discharge, while the oxygen evolution reaction (OER) occurs on the air electrode during charging [48]:

$$4OH^- \rightarrow O_2 + 2H_2O + 4e^- \qquad E_0 = 0.401\ V \tag{11}$$

The overall reaction for charging RZABs is the opposite of discharging:

$$2ZnO \rightarrow 2Zn + O_2 \tag{12}$$

Charging of RZABs is complicated due to oxygen gas forming during OER (11), which introduces multiple problems such as increased pressure in the cell, reduced electrochemically active surface area of the air electrode catalyst due to bubbles, and related bubble-induced overpotential [49–51]. Several ways have been proposed to address these issues, which involve facilitating the diffusion of produced oxygen by specifically engineering the air electrode [50,52].

For rechargeable zinc-air batteries, bifunctional electrocatalysts are required to lower the overpotential of the reactions occurring on the air electrode during both charging and discharging [53]. A wide variety of biomass-derived catalyst materials has been investigated for this purpose, as given in Table 2. An additional challenge associated with RZABs is that cell design has a large effect on the performance of the battery [54]. However, the vast majority of RZABs described in the literature are home-made cells without any standardized parameters, which makes direct comparison between studies difficult [12,55]. Furthermore, lab-scale RZABs tend to use excess amounts of both the zinc

electrode and the electrolyte, which may improve the observed performance, but do not accurately reflect practical operating conditions [42,55].

Table 2. RZAB performance of bifunctional biomass-derived catalyst materials.

Material	Biomass source	P_{max}, mW cm^{-2}	Stability testing results*	Ref.
4Fe4NiNCR	Rapeseed press cake	202	68 h @ 25 mA cm^{-2} (68 cycles, 12.5 mAh cm^{-2}) 148 h @ 5 mA cm^{-2} (876 cycles, 0.42 mAh cm^{-2})	[IV]
05Fe05NiPhenIC FeNiPhenIC	Rapeseed press cake	192 205	65 h @ 10 mA cm^{-2} (33 cycles, 10 mAh cm^{-2})	[V]
GPNCS	Glossy privet fruit	68	500 h @ 10 mA cm^{-2} (1340 cycles, 1.67 mAh cm^{-2})	[56]
Fe_2N@NCNTs	Eichhornia crassipes	135	200 h @ 5 mA cm^{-2} (600 cycles, 0.83 mAh cm^{-2})	[57]
$FeCoP_2$-NPWC	Wheat straw	123	110 h @ 5 mA cm^{-2} (225 cycles, 1.22 mAh cm^{-2})	[58]
CoN_x/Zn-NC	Locust bean gum	164	115 h @ 5 mA cm^{-2} (345 cycles, 0.83 mAh cm^{-2})	[59]
FeP-NWCC	Paulownia wood	144	450 h @ 10 mA cm^{-2} (1350 cycles, 1.67 mAh cm^{-2})	[60]
U–MnO_2-0.01/PSNC	Prawn shells	187	334 h @ 10 mA cm^{-2} (500 cycles, 3.33 mAh cm^{-2})	[61]
SAC-FeN-WPC	Wood	152	80 h @ 5 mA cm^{-2} (240 cycles, 0.83 mAh cm^{-2})	[62]
D-BNGFe-2-900‖NiFe-LDH@CF	Peanut shells	142	407 h @ 10 mA cm^{-2} (610 cycles, 3.33 mAh cm^{-2}) 250 h @ 20 mA cm^{-2} (375 cycles, 6.67 mAh cm^{-2})	[63]
$Co_{1-x}S$@SNFC	Lignin	207	40 h @ 10 mA cm^{-2} (no cycling data given)	[64]
NCO@HHPC-0.5	Gelatin	267	487 h @ 10 mA cm^{-2} (1460 cycles, 1.67 mAh cm^{-2})	[65]
Co@NCW–4	Paulownia wood	214	153 h @ 10 mA cm^{-2} (459 cycles, 1.67 mAh cm^{-2})	[66]
NS-5	Aubergine peels	90	70 h @ 5 mA cm^{-2} (3150 cycles, 0.056 mAh cm^{-2})	[67]
Fe-NSDC	Porphyra	225	67 h @ 4 mA cm^{-2} (402 cycles, 0.33 mAh cm^{-2})	[68]
Co/N-HPCs-800	Sodium alginate	160	30 h @ 5 mA cm^{-2} (164 cycles, 0.46 mAh cm^{-2})	[69]

*Areal cycling capacity calculated from data via the equation C_a = (cycling time*current density) / (2*cycle count) if not given in the article

4.3. Non-precious metal electrocatalysts

PGM-free electrocatalysts are currently being intensively investigated as cost-effective alternatives to replace expensive PGM-based catalysts for ORR and OER. For the ORR, these catalysts are typically carbon-based materials doped with heteroatoms, such as nitrogen, sulfur, and/or phosphorus, and often incorporate transition metals, such as iron, cobalt, manganese, copper, and/or nickel [6,70]. The most commonly used preparation method for the synthesis of these catalysts is high-temperature pyrolysis (>600 °C) of the corresponding precursors in an inert atmosphere (for example, in nitrogen or argon). Carbon is the most widely used catalyst support for ORR, as these electrocatalysts must be electrically conductive and chemically stable in highly alkaline or acidic conditions. Additionally, the high specific surface area of porous carbon supports allows for a high density of accessible active sites. In contrast, metal substrates such as nickel or stainless-steel mesh have been extensively used for OER, as they are generally more stable at the OER potentials compared to carbon-based materials [48].

The ORR-active sites for PGM-free catalysts in alkaline environments are considered to be atomically dispersed transition metals coordinated with up to four nitrogen atoms (M-N_x centers), various nitrogen-containing groups, and transition-metal-containing nanoparticles embedded in doped carbon (M@N-C sites) [6,8]. Nitrogen may be embedded in the carbon structure in pyridinic, pyrrolic, or graphitic configurations, in addition to the nitrogen in M-N_x centers (Figure 3). M-N_x centers, particularly Fe-N_x, have shown especially high ORR activity [6]. The existence of M-N_x centers and their importance for ORR can be demonstrated by cyanide (CN^-) poisoning experiments, in which CN^- ions bind strongly to these sites and inhibit the ORR activity [71]. Nitrogen and other heteroatom dopants, such as phosphorus and sulfur, can change the electron density of neighboring carbon atoms and other active sites, resulting in improved ORR activity [72]. For example, density functional theory (DFT) studies of Fe-N_x sites indicated that Fe coordinated to pyrrolic-N increased the ORR activity by an order of magnitude compared to Fe coordinated with pyridinic-N by activating adjacent carbon atoms for ORR [73]. A similar conclusion was reached in another DFT study, where carbon atoms near the Fe-N_x site improved the ORR activity if the iron in Fe-N_x site had adsorbed hydroxide anions, which may be the case in an alkaline environment [74]. Different phosphorus site positions near Fe-N_4 sites were noted to modulate the adsorption strength of ORR intermediates [75]. For metal-free nitrogen-doped carbon catalyst materials, it is still unclear which nitrogen species is the most active for ORR, as different studies attribute the activity to each of these sites [76,77]. In general, the nitrogen atom is assumed to induce a positive charge onto neighboring carbon atoms, which improves oxygen adsorption and subsequent reduction, resulting in better ORR performance [77]. Thus, the neighboring carbon atoms are often considered the active sites in metal-free nitrogen doped materials, not the nitrogen atoms [77]. For M@N-C sites, the ORR activity is often explained by synergistic effects

between the metal nanoparticle core and the surrounding N-doped graphitic carbon shell [78]. Catalysts containing Fe-N_4 sites and Fe nanoparticles have been shown to possess enhanced ORR activity originating from activation of the O_2 molecule due to improved adsorption energies and stretching of the O-O bond [79]. Additionally, it has been suggested that the electron-donating effect of the transition-metal-containing nanoparticle core improves the work function of the carbon shell, which again results in increased ORR activity [80,81].

While M-N_x centers have high electrocatalytic activity for ORR, it is difficult to obtain a high number of M-N_x centers in the catalyst material, because simply increasing the transition metal content in the precursor mixture results in the formation of metal nanoparticles. One way to sidestep this issue is by separating the carbon formation procedure from the metal doping step while using nitrogen-based coordination complexes of the corresponding metals for doping [82]. This two-step synthesis procedure may allow for the preparation of a more stable carbon base material, while the subsequent doping step can be carried out at a lower pyrolysis temperature to affix the M-N_x active sites to the structure and avoid the formation of metal nanoparticles.

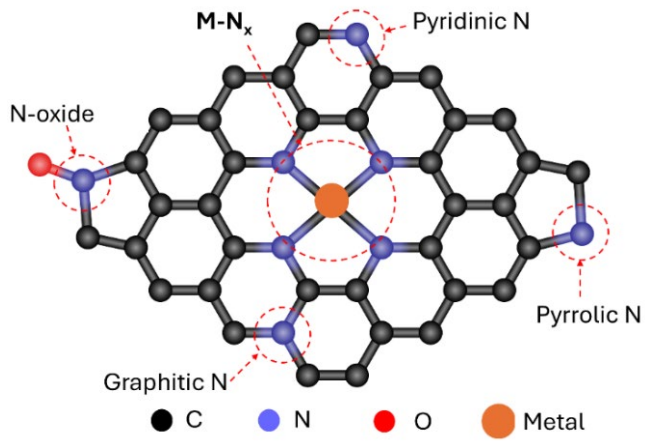

Figure 3. Nitrogen-containing active sites for ORR.

For OER, the identification of active sites is complicated due to surface re-structuring of the electrocatalysts during operation, but transition-metal oxides, (oxy)hydroxides, and various transition-metal-containing nanoparticles have all been shown to have high electrocatalytic OER activity [48]. Bimetallic iron- and nickel-containing catalysts stand out as state-of-the-art materials, the activity of which is often attributed to favorable charge redistribution effects [83]. This synergistic effect improves the OER performance to such an extent that even part-per-million level iron impurities in the supporting KOH electrolyte have been found to significantly enhance the activity of supposedly monometallic nickel-based catalyst materials [84]. However, metal-free materials have also shown

some electrocatalytic activity for OER. For example, a metal-free nitrogen and phosphorus co-doped material displayed high OER activity, which was attributed to the carbon sites located adjacent to specific P-N bonds in the carbon structure [85].

Biomass is a useful precursor due to the inherent presence of heteroatoms, which can act as active sites for ORR or modulate the electrocatalytic activity of nearby active centers [15]. This can simplify the production of the catalysts, as external nitrogen or phosphorus sources may not be needed. However, this is highly dependent on the specific biomass used, and transition metal sources are still necessary to reach high ORR activity. An additional advantage of biomass-based precursors is that their naturally occurring hierarchical porous structure may be partially retained even after high-temperature pyrolysis [86]. While, in principle, any biomass source could be used for the preparation of electrocatalysts, research has primarily focused on using waste biomass. A wide range of biomass sources have been used for the preparation of electrocatalysts for AEMFCs and RZABs, as summarized in Tables 1 and 2.

An appropriate porous structure of electrocatalysts is essential for achieving high electrocatalytic activity. Hierarchical structures containing abundant micropores connected by mesopores are considered beneficial for ORR electrocatalysis, with mesopores facilitating mass transport and micropores hosting the active sites [87,88]. Carbon is an ideal support material in this context because, in addition to being electrically conductive, it can be tailored to exhibit a wide range of pore sizes and structures [86,87,89]. One of the most commonly used methods is chemical activation using acids or bases, or physical activation with reactive gases, like ammonia or steam [14,86]. However, this approach typically results in materials with mainly microporous structure, which is not ideal. Another common method is the silica nanocasting technique, in which silica particles with a certain structure are used as templates to produce highly porous carbon with controlled pore size distributions [89,90]. This technique has been commercialized, for example, as the Varipore™ method [91]. However, while constructing the desired pore structure in this way is relatively straightforward, removing the silica requires the use of concentrated hydrofluoric acid, which is highly toxic and hazardous. Another approach is to use hard templates that can be removed more easily, like magnesium oxide, zinc oxide, calcium carbonate, sodium chloride [I], and others [31,89,92]. These can either be added directly to the synthesis mixture or formed *in situ* from template precursors such as magnesium acetate [III, IV] or magnesium nitrate [V, VI]. Removal of these templates can be achieved either by simple dissolution in water [I] or by treatment with dilute acids or bases. Another method that has gained significant attention is the use of metal-organic frameworks [93,94]. Materials produced from zeolitic imidazolate frameworks like ZIF-8, a subclass of metal-organic frameworks, exhibit ordered, highly porous structures along with controlled distribution of active sites for ORR [95,96].

4.4. Electrochemical characterization methods

For the electrochemical characterization of electrocatalysts, the most commonly used techniques are the rotating disk electrode (RDE) and the related rotating ring-disk electrode (RRDE) methods [97,98]. For a typical RDE experiment, a suspension of the catalyst material and a binder is prepared and sonicated to ensure uniform dispersion. A known amount of the catalyst is then deposited onto a glassy carbon (GC) electrode and dried, after which the electrode is attached to a rotator to form the RDE system. The RDE is used as the working electrode in a three-electrode electrochemical cell, which also includes a reference electrode and a counter electrode. The cell is filled with a relevant electrolyte, usually 0.1 M KOH for alkaline environment, which is saturated with oxygen or an inert gas. Linear sweep voltammetry or cyclic voltammetry is then used in order to characterize the electrochemical performance of the catalysts. This is usually carried out at low potential scan rates of around 10 mV s^{-1} to minimize the contribution of capacitive current. In the RDE measurements, the electrode is rotated to enhance mass transport of oxygen, leading to the formation of a diffusion-limited current plateau at higher overpotentials. Additionally, the background currents measured in the same solution saturated with an inert gas is subtracted from the experimental ORR currents. The experimentally measured polarization curves may be further corrected for the ohmic (iR) drop related to the combined resistance of the solution and the experimental setup, which becomes more relevant at higher current densities. The key parameters for ORR include the onset potential (E_{onset}, defined as the potential at which the ORR current density reaches –0.1 mA cm^{-2}) and the half-wave potential ($E_{1/2}$, defined as the potential at which the ORR current density reaches half of the diffusion-limited current density). For OER, the parameter $E_{j=10}$ is used, representing the potential at which the OER current density reaches 10 mA cm^{-2}. For bifunctional ORR/OER electrocatalysts, the parameter ΔE is defined as the difference between $E_{j=10}$ and $E_{1/2}$. Higher E_{onset} and $E_{1/2}$ values indicate better electrocatalytic activity for ORR, while lower $E_{j=10}$ values reflect superior OER activity.

RDE polarization data measured at different rotation rates are typically analyzed using the Koutecky-Levich (K-L) equation [99]:

$$\frac{1}{j} = \frac{1}{j_k} + \frac{1}{j_d} = \frac{1}{j_k} - \frac{1}{0.62nFD_{O_2}^{2/3}C_{O_2}\nu^{-1/6}\omega^{1/2}} \tag{13}$$

where j is the measured current density, j_d is the diffusion limited current density, j_k is the kinetic current density, n is the number of electrons transferred, F is the Faraday constant, D_{O2} is the diffusion coefficient of oxygen in the solution, C_{O2} is the concentration of dissolved oxygen in the solution, ν is the kinematic viscosity of the electrolyte, and ω is the electrode rotation rate.

The K-L analysis provides valuable information about the catalysts, such as the kinetic current density and the number of electrons transferred during ORR (n). The kinetic current obtained at a specific potential can be normalized to the catalyst mass to obtain the mass activity (MA) value. Higher MA values indicate

improved intrinsic electrocatalytic activity. The value of *n* is between two and four for ORR, corresponding to different reaction pathways according to equations (2–5). The RRDE method is used to determine the value of *n* directly by employing an additional platinum ring electrode around the disk electrode. The platinum ring is polarized at a fixed potential and is active for oxidation of the HO_2^- intermediate, generating a measurable current that is used to calculate the *n* values for the corresponding catalyst (Eq.14) and the percentage of HO_2^- produced during the ORR process (Eq.15):

$$n = \frac{4I_d}{I_d + \frac{I_r}{N}} \tag{14}$$

$$\%HO_2^- = \frac{\frac{2I_r}{N}}{I_d + \frac{I_r}{N}} \times 100\% \tag{15}$$

where *n* is the number of electrons transferred, I_d is the disk current, I_r is the ring current and *N* is the collection efficiency of the ring.

While RDE analysis provides essential information about the properties of the catalyst, it has several limitations. The K-L equation assumes a flat and smooth electrode surface, which is not the case for highly porous carbon-based catalysts [100]. As a result, the values of *n* derived in this way may be inaccurate. Additionally, the current densities used in AEMFCs are orders of magnitude higher, often exceeding 1 A cm^{-2}, compared to less than 10 mA cm^{-2} in RDE measurements [98]. This is due to the low oxygen diffusion coefficient in liquid electrolytes such as 0.1 M KOH, in contrast to the much faster diffusion in the gas phase. The gas-diffusion electrode (GDE) method enables operation at higher current densities, as the working electrode consists of a catalyst-coated GDL [98,101–103]. One side of the GDE is in contact with the electrolyte, while the opposite side is exposed to oxygen, allowing for faster mass transport and conditions that more closely resemble those in AEMFCs. Additionally, this method allows for the investigation of catalyst layer properties, such as catalyst loading, coating methods and ionomer content [98,101].

The final characterization method is the evaluation of the catalyst materials in AEMFCs or RZABs. However, these measurements are complex and require consideration of additional parameters relevant to the studied system. For RZABs, it has been shown that peak power density (P_{max}) values depend on the ratio of zinc electrode area to air electrode area, the electrolyte concentration, and the distance between the electrodes [54,104]. AEMFC measurements are considerably more intricate and, in addition to the intrinsic properties of the catalyst material, depend on other factors such as cell temperature, gas flow rates, humidification and backpressure, the type and thickness of anion-exchange membrane, catalyst layer fabrication, ionomer content and type, and the solvents used in catalyst ink preparation [7,20,23,27,105,106]. Due to these influencing factors, isolating the intrinsic catalyst performance is challenging. However, the results can be interpreted as a lower bound on catalyst performance under practical operating conditions, which is useful for real-world applications.

5. EXPERIMENTAL

5.1. Synthesis of biomass-derived electrocatalysts

5.1.1. Synthesis of electrocatalysts from glucose

Iron-containing nitrogen-doped carbon materials were prepared from D-glucose (Sigma-Aldrich) as a carbon source, potassium hexacyanoferrate ($K_3[Fe(CN)_6]$, Sigma-Aldrich) as an iron source, dicyandiamide (DCDA, Sigma-Aldrich) or urea (Sigma-Aldrich) as a nitrogen source, and sodium chloride (NaCl, Merck) as a hard template (see Table 3) [I]. These compounds were dissolved in water, and the resulting mixture was dried overnight at 35 °C, followed by grinding using a mortar and pestle. The obtained powder was pyrolyzed in a quartz tube furnace in N_2 atmosphere with a heating rate of 5 °C min^{-1} up to 800 or 900 °C, where it was held for 1 or 2 h. After the tube furnace had naturally cooled down, the resulting catalyst powder was ground using a planetary ball mill with a ZrO_2 grinding bowl and 5 mm ZrO_2 balls and subsequently washed with copious amounts of Milli-Q water to remove the NaCl template. The final product was obtained after drying overnight in an oven at 60 °C. In total, eight materials were synthesized, along with an additional metal-free material made without adding the iron salt (see Table 3).

Table 3. The amounts of precursors and pyrolysis conditions used for catalyst preparation [I].

Catalyst	Glucose (mg)	NaCl (mg)	$K_3[Fe(CN)_6]$ (mg)	DCDA or urea (mg)	Pyrolysis procedure
FeNC1	200	800	11.8	267	800 °C, 2 h
FeNC2	200	200	11.8	267	800 °C, 2 h
FeNC3	200	1600	11.8	267	800 °C, 2 h
FeNC4	200	800	47.2	267	800 °C, 2 h
FeNC5	200	800	5.9	267	800 °C, 2 h
FeNC6	200	800	11.8	267	900 °C, 1 h
FeNC7	200	800	11.8	800	800 °C, 2 h
FeNC8	200	800	11.8	267 (urea)	800 °C, 2 h
NC	200	800	-	267	800 °C, 2 h

5.1.2. Synthesis of electrocatalysts from rapeseed press cake

The iron- and/or cobalt-containing catalyst materials were prepared from hot-pressed rapeseed press cake (Scanola Baltic AS) as a carbon source, iron(III) nitrate nonahydrate ($Fe(NO_3)_3 \cdot 9H_2O$, Sigma-Aldrich) and cobalt(II) nitrate hexahydrate ($Co(NO_3)_2 \cdot 6H_2O$, Sigma-Aldrich) as transition metal sources, and

DCDA (Sigma-Aldrich) as the nitrogen source (Table 4) [II]. The precursors were mixed together in 50 mL of isopropanol, sonicated for 15 min, and dried overnight at 50 °C. The dry precursor mixture was then manually ground in a mortar and pyrolyzed in a quartz tube furnace in a N_2 atmosphere at a heating rate of 10 °C min^{-1} up to 800 °C, where it was held for 2 h. After cooling, the resulting catalyst powder was ground in a mortar once more. Certain catalysts were also acid-leached in a 1:1 mixture of 0.5 M HNO_3 and 0.5 M H_2SO_4 at 50 °C for 8 h. After acid leaching, the materials were washed with Milli-Q water, dried, and pyrolyzed again using the same pyrolysis procedure. In total, six metal-containing catalyst materials were prepared in this way. For comparison, a nitrogen-doped metal-free material and pyrolyzed pristine rapeseed press cake powder were also prepared.

Table 4. The amounts of precursors and synthesis conditions used for catalyst preparation [II].

Catalyst	Rapeseed press cake (mg)	DCDA (mg)	Fe (mg)	Co (mg)	Acid treatment
FeNCR	100	1000	2.5	-	no
FeNCR-a	100	1000	2.5	-	yes
CoNCR	100	1000	-	2.5	no
CoNCR-a	100	1000	-	2.5	yes
FeCoNCR	100	1000	1.25	1.25	no
FeCoNCR-a	100	1000	1.25	1.25	yes
CR	1000	-	-	-	no
NCR	200	1000	-	-	no

In order to improve the porous structure of the catalysts, a magnesium-based hard template was used [III,IV]. Iron-containing electrocatalysts for ORR [III] and bi-functional Fe- and/or Ni-containing catalysts [IV] were synthesized in this way (Table 5).

Iron- and/or nickel-containing catalyst materials were prepared from hot-pressed rapeseed press cake (Scanola Baltic AS) as a carbon source, iron(III) nitrate nonahydrate ($Fe(NO_3)_3 \cdot 9H_2O$, Sigma-Aldrich) and nickel(II) nitrate hexa-hydrate ($Ni(NO_3)_2 \cdot 6H_2O$, Sigma-Aldrich) as transition metal sources, DCDA (Sigma-Aldrich) as a nitrogen source, and magnesium acetate tetrahydrate ($Mg(CH_3COO)_2 \cdot 4H_2O$, Sigma-Aldrich) as a template precursor (Table 5) [III, IV]. The precursors were mixed together in 50 mL of isopropanol for 15 min on a magnetic stirrer. After letting the solvent evaporate overnight at 60 °C, the pre-cursor mixture was pyrolyzed in a quartz tube furnace in N_2 atmosphere at a heating rate of 10 °C min^{-1} up to 800 °C, where it was held for 2 h. After pyrolysis, the materials were acid-leached in 50 mL of 1 M HCl by stirring at room tempe-rature for 2 h. The materials were then washed with Milli-Q water, dried, and pyrolyzed again using the same pyrolysis procedure.

Table 5. The amounts of precursors and pyrolysis conditions used for catalyst preparation [III, IV].

Catalyst	Rapeseed press cake (mg)	DCDA (mg)	Fe (mg)	Ni (mg)	$Mg(CH_3COO)_2 \cdot 4H_2O$ (mg)
FeNCR-MgAc-1-1 [III]	200	2000	5	-	302
FeNCR-MgAc-3-1 [III]	200	2000	5	-	100
FeNCR-MgAc-5-1 [III]	200	2000	5	-	60.3
2FeNCR-MgAc-3-1 [III]	200	2000	10	-	100
0.5FeNCR-MgAc-3-1 [III]	200	2000	2.5	-	100
CR-MgAc-2-1 [III]	200	-	-	-	151
FeNCR [IV]	200	2000	5	-	151
NiNCR [IV]	200	2000	-	5	151
FeNiNCR [IV]	200	2000	2.5	2.5	151
2FeNiNCR [IV]	200	2000	5	2.5	151
2Fe2NiNCR [IV]	200	2000	5	5	151
4Fe4NiNCR [IV]	200	2000	10	10	151

5.1.3. Ionothermal synthesis of electrocatalysts

Ionothermally synthesized carbon was used for the preparation of Fe- and Ni-containing N-doped catalysts for RZAB (V) and Fe- and/or Mn-containing N-doped catalysts for AEMFC (VI) (Table 6). First, a mesoporous carbon material was prepared via ionothermal synthesis using hot-pressed rapeseed press cake (Scanola Baltic AS) and magnesium nitrate hexahydrate ($Mg(NO_3)_2 \cdot 6H_2O$, Alfa Aesar). The materials were weighed and manually ground together using a pestle and mortar. The precursor mixture was pyrolyzed under N_2 flow at 800 °C for 1 h at a heating rate of 10 °C min^{-1} in a quartz tube furnace. The resulting carbon material was then acid-treated in 50 mL of 1 M HCl solution by stirring for 2 h at room temperature followed by washing with copious amounts of Milli-Q water. The ionothermal carbon was then dried overnight at 60 °C. Two different ionothermal carbon materials, denoted IC (1:2 ratio of rapeseed cake to magnesium nitrate hexahydrate) [V, VI] and IC2 (1:2.5 ratio of rapeseed cake to magnesium nitrate hexahydrate) [VI] were prepared.

In the second stage, the prepared ionothermal carbon was doped with nitrogen and iron, nickel and/or manganese using 1,10-phenanthroline as a nitrogen source [82]. The ionothermal carbon, 1,10-phenanthroline (1,10-phen, Thermo Scientific), iron(III) nitrate nonahydrate ($Fe(NO_3)_3 \cdot 9H_2O$, Sigma-Aldrich), nickel(II) nitrate hexahydrate ($Ni(NO_3)_2 \cdot 6H_2O$, Carl Roth) and/or manganese(II) acetate tetrahydrate ($Mn(CH_3COO)_2 \cdot 4H_2O$, Carl Roth) were mixed together in 7 mL of isopropanol and sonicated for 30 min (Table 6). In article [VI], solutions of

corresponding iron and manganese salts in ethanol containing 1 mg mL^{-1} of metal were prepared and used for the preparation instead of weighing the salt directly. The amount of 1,10-phenanthroline used corresponds to a 4:1 molar ratio to the metals. The resulting mixture was poured into a Petri dish, dried at 60 °C, and pyrolyzed in N_2 flow at 800 °C for 1 h (heating rate of 50 °C min^{-1}).

Additionally, some catalysts were ball-milled in a ZrO_2 grinding bowl using 6 ZrO_2 balls with a diameter of 10 mm at 400 rpm for 10 min [VI] or 2×10 min (with a 5 min pause in between) [V].

Table 6. The amounts of precursors and pyrolysis conditions used for catalyst preparation [V, VI].

Catalyst	Ionothermal carbon (mg)	1,10-phen (mg)	Fe (mg)	Ni (mg)	Mn (mg)	Ball-milling
095Fe005NiPhenIC [V]	25 (IC)	19.5	1.42	0.08	-	no
08Fe02NiPhenIC [V]	25 (IC)	19.5	1.2	0.3	-	no
066Fe034NiPhenIC [V]	25 (IC)	19.5	0.99	0.51	-	no
05Fe05NiPhenIC [V] 05Fe05NiPhenIC-BM [V]	25 (IC)	19.5	0.75	0.75	-	no yes
034Fe066NiPhenIC [V]	25 (IC)	19.5	0.51	0.99	-	no
FeNiPhenIC [V] FeNiPhenIC-BM [V]	25 (IC)	39	1.5	1.5	-	no yes
FeIC [VI]	50 (IC)	13	1	-	-	yes
MnIC [VI]	50 (IC)	13	-	-	1	yes
FeMnIC [VI]	50 (IC)	13	0.5	-	0.5	yes
FeIC2 [VI]	50 (IC2)	13	1	-	-	yes
MnIC2 [VI]	50 (IC2)	13	-	-	1	yes
FeMnIC2 [VI]	50 (IC2)	13	0.5	-	0.5	yes

5.2. Physicochemical characterization

Scanning electron microscopy (SEM) samples were prepared by drop-casting a suspension of the catalyst material in 2-propanol onto polished GC disks. The SEM images were taken using a Nova NanoSEM 450 (FEI) [I] or Helios NanoLab 600 (FEI) [II–VI] microscope. For elemental characterization, an energy dispersive X-ray spectroscopy (EDX) detector INCA Energy 350 (Oxford Instruments) was used.

For high-resolution scanning transmission electron microscopy (HR-STEM) measurements, the materials were suspended in isopropanol and deposited onto holey carbon supports on Cu grids (Agar Scientific). The STEM measurements were performed at 200 kV using a FEI Titan Themis 200 microscope equipped with a SuperX EDX system (FEI/Bruker) in scanning mode to acquire high-angle annular dark field (HAADF) and bright field (BF) images. STEM-EDX elemental

mapping was performed using Esprit software, with corresponding HAADF images acquired from the same locations to accurately define the regions of analysis.

For obtaining the N_2 physisorption isotherms, the catalyst materials were degassed in vacuum for 12 h at 200 °C before measurements. The N_2 isotherms were recorded on a NovaTouch LX2 analyzer (Quantachrome) at the boiling point of nitrogen (77 K). Brunauer–Emmett–Teller (BET) surface area (S_{BET}) of the catalysts was calculated at a relative pressure (P/P_0) between 0.02 and 0.2. The total pore volume (V_{tot}) was measured at $P/P_0 = 0.97$. The specific surface area (S_{dft}), the micropore volume (V_μ) and the pore size distribution (PSD) of the catalyst materials were calculated using the quenched solid density functional theory (QSDFT) equilibrium model for slit [I–IV] or slit-cylindrical [V, VI] type pores. TouchWin 1.11 software (Quantachrome Instruments) was used to perform all the calculations.

For micro-Raman spectroscopy, the samples were suspended in 2-propanol and drop-casted onto silicon substrates. Raman spectra were recorded in the back-scattering geometry on an inVia Renishaw spectrometer in conjunction with a confocal microscope (Leica Microsystems CMS GmbH), 50X objective and an argon ion laser operated at 514.5 nm. Low incident laser power density at the sample prevented excessive sample heating and decomposition while providing averaged information over a ~200 μm^2 surface area in a single exposure. Raman spectra processing involved baseline correction and multiple-peak fitting procedure using PeakAnalyser software in OriginPro 9.

The X-ray photoelectron spectroscopy (XPS) analysis was conducted using an electron energy analyzer SCIENTA SES100 and a non-monochromatic twin anode X-ray tube (Thermo XR3E2) with the incident X-ray energy of 1253.6 eV (Mg K_α). The survey scans were measured in the energy range from 900 to 0 eV, pass energy of 200 eV, step size of 0.5 eV, step duration of 0.2 s and number of scans of 5. Detailed spectra were collected with the step size of 0.1 eV and step duration of 0.2 s; the number of scans was at least 25. The data processing using CasaXPS software (version 2.3.17) involved removal of the K_α and K_β satellites. For peak fitting, Gauss–Lorentz hybrid function (GL 70, Gauss 30 %, Lorentz 70 %) and a blend of linear and Shirley-type backgrounds were used.

In article [III], microwave plasma atomic emission spectroscopy (MP-AES) was used to determine metal contents in the samples using Agilent 4210 MP-AES. 10 mg of the catalyst material was dissolved in a mixture of 4 mL of HNO_3 and 2 m of H_2O_2 using the Anton Paar Multiwave PRO microwave digestion system with NXF100 vessels (PTFE/TFM liner). The dissolved samples were digested at pressures between 45–50 bar at 230 °C. Before measuring, the samples were diluted with a 2% HNO_3 solution to obtain metal concentrations of around 5 mg/l.

X-ray diffraction (XRD) measurements were performed on Bruker D8 Advance diffractometer with Ni-filtered Cu Kα radiation. The scanning step used to obtain the diffraction patterns was 0.0133° 2θ in the range from 3° to 92° with a counting time of 384 s per step. Topas 6 (Bruker) software was used to analyze the data.

5.3. Electrochemical characterization

5.3.1. RDE and RRDE experiments

Electrochemical measurements were conducted in an aqueous 0.1 M KOH solution saturated with oxygen (99.999%, Linde) or argon (99.999%, Linde) using an Autolab PGSTAT30 potentiostat/galvanostat (Metrohm-Autolab, The Netherlands). In a standard three-electrode setup, a saturated calomel electrode (SCE) was used as a reference electrode, a carbon rod as a counter electrode, and a catalyst-coated GC disk as a working electrode (geometric area of 0.196 cm^2). Before drop-coating, the GC electrodes were polished with 1 and 0.3 μm alumina slurry (Buehler) and cleaned by sonication in Milli-Q water. 4 mg of the catalyst material was suspended in the solution containing 980 μL of 2-propanol, and 20 μL of Nafion® ionomer solution (5 wt% in lower aliphatic alcohols, Ion Power) [IV-VI], 960 μL of 2-propanol and 40 μL of Nafion® solution [I, III] or 480 μL of 2-propanol, 480 μL of Milli-Q water, and 40 μL of Nafion® solution [II]. The suspensions were sonicated for 30 min to ensure the dispersion of the catalysts in the solution. Three drops of 3.33 μL of the prepared suspension were used to coat the GC electrodes, resulting in a catalyst loading of 200 μg cm^{-2}, which were then dried in air. The GC electrodes were coated with reference catalysts 20% Pt/C (E-TEK) [I-VI] and 50:25:25 PtRu/C (Alfa-Aesar) [IV, V] using the same procedure and catalyst loading of 200 μg cm^{-2}.

In RDE experiments, an EDI101 rotator with a CTV101 speed controller (Radiometer) was used. The electrode rotation rate (ω) was varied from 360 to 3100 rpm and the corresponding RDE data was analyzed by the K-L equation (13) in order to determine the number of electrons transferred per O_2 molecule (n). For RRDE experiments in articles [I, III], an AFMSRX rotator (Pine Research, USA), together with a MSRX speed controller, was used. The Pt ring electrode was polarized at 1.55 V *vs* the reversible hydrogen electrode (RHE) to detect HO_2^- anions produced during the RRDE experiments. The Pt ring electrode was electrochemically cleaned by potential cycling between 0.55 and 1.65 V vs RHE at 100 mV s^{-1} for 3 cycles before measurements were performed. The collection efficiency (N) of the Pt ring electrode was 0.22. RRDE data were analyzed to determine the value of n by Equation (14) and the HO_2^- yield by Equation (15).

The accelerated stability tests were carried out in the potential range of 1.0–0.4 V vs RHE for 5000 [I] or 10000 [II–VI] potential cycles at a scan rate of 100 mV s^{-1}, with RDE polarization curves recorded at 1900 rpm before and after cycling. The chronoamperometric (CA) stability tests were carried out at 0.5 V vs RHE for 10 h at 960 rpm [I-V].

In articles [V, VI], the double-layer capacitance (C_{dl}) measurements were carried out by recording cyclic voltammograms between 0.8–1.0 V in argon-saturated 0.1 M KOH solution using different scan rates (10, 20, 30, 40, 60, 80, and 100 mV s^{-1}). The differences between anodic and cathodic current densities at specific scan rates were linearly fitted, and C_{dl} was calculated as half the slope.

Potentials are given with respect to the RHE. Potentials were converted to the RHE via the equation $E_{RHE} = E_{SCE} + 1.008$ V. Background currents recorded in argon-saturated 0.1 M KOH solution were subtracted from the experimental ORR currents for the analysis and presentation of the ORR polarization curves. In articles [IV-VI], the ORR and OER polarization curves were also corrected for the ohmic (iR) drop for data analysis and presentation.

5.3.2. GDE experiments

In article [VI], GDE experiments were conducted using a simplified, 3D printed version of a design described by Inaba and co-workers [102]. The reference electrode was Hg/HgO (20 wt% KOH), and the counter electrode was a platinum plate. For preparing the catalyst suspensions, 10 mg of the respective catalysts were mixed with 2.45 mL of 2-propanol and 50 µL of Nafion® ionomer solution (5 wt% in lower aliphatic alcohols, Ion Power). The suspensions were sonicated for 30 min. GDEs used as working electrodes were prepared by cutting out circular GDLs (Sigracet 39 BB, Fuel Cell Store) with a diameter of 1.8 cm. The GDLs were then spray-coated using the catalyst suspensions to achieve a loading of 0.9 ± 0.1 mg cm^{-2}. The ORR polarization curve measurements were performed galvanostatically in an aqueous 1 M KOH solution, at a current rate of 1 mA cm^{-2} s^{-1}, in air and at room temperature. The area of the GDE in contact with the solution was 0.196 cm^2 (0.5 cm diameter circle) and this value was used for calculating the current density. Potentials were converted to the RHE via the equation $E_{RHE} = E_{Hg/HgO} + 0.924$ V. For analysis and presentation, the GDE polarization curves were corrected for the ohmic (iR) drop.

5.3.3. RZAB experiments

For RZAB experiments, different in-house RZAB devices were used. A polished Zn foil (99.9%, Auto-plaza) with a thickness of 0.2 mm was used as the Zn electrode. The air electrode consisted of a commercial GDL (Sigracet 39 BB, Fuel Cell Store), which was spray-coated with various catalyst loadings. The same catalyst suspensions were used for GDL coating as for the RDE experiments. In article [V], Freudenberg H23C8 GDL (Fuel Cell Store) was used for investigating the ionomer type and amount to optimize the catalyst loading, while Sigracet 39 BB was used for the other measurements. The catalyst loading on the air electrode was determined by weighing the GDL before and after spray coating. An aqueous solution of 6 M potassium hydroxide (KOH, Sigma-Aldrich) containing 0.2 M zinc acetate (prepared using zinc acetate dihydrate $Zn(CH_3COO)_2{\cdot}2H_2O$, Fisher Scientific) was used as the electrolyte.

In article [IV], two different in-house RZABs, designated as Battery 1 and Battery 2, were used to investigate the effects of different battery properties. For Battery 1, the air electrode area exposed to the electrolyte was 0.79 cm^2 (1 cm diameter circle) and the Zn electrode area exposed to the electrolyte was 2.55 cm^2 (1.8 cm diameter circle). The total Zn mass available to Battery 1 was 0.366 g,

which was determined by cutting out and weighing a circular piece of Zn foil with a diameter of 1.8 cm. The amount of Zn corresponds to a maximum battery capacity of 300 mAh. The volume of electrolyte in the ZAB was 2 mL. Battery 2 had an air electrode area of 1 cm^2 (1 cm × 1 cm square) and a Zn electrode area of 6.25 cm^2 (2.5 cm × 2.5 cm square) exposed to the electrolyte. The electrolyte volume was 7 mL. The total Zn mass available to Battery 2 was 0.893 g, which corresponds to a theoretical maximum battery capacity of 732 mAh. The distance between the electrodes was 1 cm for both batteries. In article [V], a battery with the same parameters as Battery 2 was used, except for an electrolyte volume of 6.5 mL.

The discharge polarization curve measurements of the Zn-air batteries were done at a scan rate of 10 mA min^{-1} (0.167 mA s^{-1}). The capacity of the battery was determined by discharging it at a current density of 20 mA cm^{-2}. The specific capacity was determined by dividing the measured capacity of the battery by the total Zn mass available to the battery. The stability and rechargeability of the battery were analyzed by discharge-charge cycling using 1 h discharging cycles at 25 mA cm^{-2} for 30 min, followed by charging at 25 mA cm^{-2} for 30 min [IV], or 2 h cycles of discharging at 10 mA cm^{-2} for 1 h, followed by charging at 10 mA cm^{-2} for 1 h. Charging efficiency was determined by dividing the discharge voltage by the charging voltage. The open circuit voltage (OCV) of the battery was determined 5 min after connecting the battery to the potentiostat.

All RZAB measurements were done at room temperature and in ambient air. In article [IV], additional polarization curves were measured in a pure O_2 atmosphere. The voltage limits used were 0.2 and 3.5 V [IV] or 0.4 and 3 V [V], at which point the experiments were stopped. The measured current density was normalized to the area of the air electrode. The OCV of the RZAB was determined 5 min after connecting the battery to the potentiostat.

5.3.4. AEMFC experiments

Single-cell AEMFC testing was conducted using a Greenlight Fuel Cell Test Station (G40 Fuel Cell System, Hydrogenics, Canada) and a 5 cm^2 test cell (Fuel Cell Technologies, USA) with graphite bipolar plates and serpentine flow fields.

In article [II], the membrane-electrode assembly was prepared using an AF2-HLE8-10-X (AEMION+ 10 μm) AEM and a catalyst-coated GDL (Sigracet 39 BC). The ionomer solution (3 wt%) was made by dissolving AP2-INN8-00-X (AEMION+ Powder) in methanol. The catalyst ink for the anode GDL was prepared using 6.7 mg of 50:25:25 PtRu/C (Alfa Aesar), 689 μL of methanol, 196 μL of Milli-Q water, and 49 μL of ionomer solution (3 wt%). The cathode GDL catalyst ink was prepared by dispersing 12.5 mg of FeCoNCR-a in 1340 μL of methanol, 391 μL of Milli-Q water, and 130 μL of ionomer solution (3 wt%). The catalyst inks were sonicated and drop-cast onto the GDL. The catalyst loadings of 0.8 mg_{PtRu} cm^{-2} and 2 mg cm^{-2} were calculated for the anode and cathode, respectively. The electrodes and the AEM were soaked in 3 M KOH solution prior to MEA preparation. One day of soaking was used for the electrodes and

four days for the AEM to ensure conversion to the OH^- form. The 3 M KOH solution for the latter was changed daily. The electrodes, AEM, and silicone gaskets were pressed together with a torque of 9 N m. The cell was operated using humidified hydrogen and oxygen gases at flow rates of 1 normal liters per minute (NLPM) at 60 °C, 50% relative humidity (RH), and a backpressure of 200 kPa.

In article [III], the cathode suspension was prepared using 25.8 mg of the FeNCR-MgAc-3-1 catalyst, which was dispersed in a mixture of Milli-Q water and 2-propanol (volume ratio 1:15), along with a PiperION ionomer solution (5 wt%, Versogen) by sonication in an ice-cooled bath for 2 h. The ionomer-to-carbon (I/C) ratio was 0.35. For preparation of the anode suspension, 20 mg of 40:20 PtRu/C (HiSPEC, Thermo Scientific) was dispersed in the same solvent mixture using the same procedure and PiperION ionomer at an I/C ratio of 0.75. To prepare the MEAs, the catalyst inks were spray-coated on GDLs (Freudenberg H23C8) with an airbrush, to obtain the cathode and anode catalyst loadings of 0.92 mg cm^{-2} and 0.5 mg_{PtRu} cm^{-2}, respectively. Before MEA preparation, the prepared GDEs, along with a PiperION membrane (20 μm, self-supporting, Versogen), were soaked in a 1 M KOH solution overnight. The GDEs and membrane, together with Teflon gaskets, were assembled in the test cell with a torque of 7 N m. The gaskets were selected to obtain a GDL compression of 30%. The AEMFC polarization curves were measured at 80 °C and 150 kPa back-pressures on both the anode and cathode sides. The flow rate of H_2 and O_2 gases was 0.1 NLPM; the anode and cathode dewpoints were set at 70 and 74 °C, respectively.

In article [VI], the cathode catalyst suspensions were prepared by dispersing 20 mg of catalyst in a mixture of 4.39 mL 2-propanol, 440 μL Milli-Q water, and 170 μL PiperION ionomer solution (5 wt%, Versogen). The anode catalyst suspension was prepared using 21.2 mg of 40:20 PtRu/C (HiSPEC, Thermo Scientific) catalyst, 3.23 mL 2-propanol, 295 μL Milli-Q water, and 175 μL of the same 5 wt% PiperION ionomer solution. Both suspensions were sonicated in an ice-cooled bath for 1 h to obtain a homogeneous dispersion. The GDEs were prepared by spray coating the catalyst suspensions on GDLs (Sigracet 39 BB) to obtain anode loadings of 0.8 mg cm^{-2} (0.48 mg_{PtRu} cm^{-2}) and cathode loadings of 0.9 ± 0.1 mg cm^{-2}. The loading for the 20 wt% Pt/C reference catalyst was 0.7 mg cm^{-2} (0.14 mg_{Pt} cm^{-2}). Before MEA preparation, the PiperION membrane (20 μm, Versogen) was soaked in a 1 M KOH solution overnight. The prepared GDEs were soaked in 1 M KOH solution for 1 h directly before MEA assembly. The GDEs and membrane, together with Teflon gaskets, were assembled in the test cell using a torque of 7 N m. The gaskets were selected to obtain a GDL compression of 30%. The AEMFC polarization curves were measured at 80 °C and 200 kPa backpressures on both the anode and cathode sides. The flow rate of the fully (100%) humidified H_2 and O_2 gases was 0.1 NLPM (0.3 NLPM for 20 wt% Pt/C).

6. RESULTS AND DISCUSSION

6.1. Electrocatalysts derived from glucose

In the first part of the work, glucose was used as a carbon source in the preparation of electrocatalysts along with DCDA as a nitrogen source, potassium hexacyanoferrate(III) ($K_3[Fe(CN)_6]$) as an iron source, and sodium chloride (NaCl) as a hard template, as described in Section 5.1.1 [I]. The catalysts were obtained by simple pyrolysis, after which the NaCl template was washed away with Milli-Q water. Glucose is the most abundant simple sugar, which is generally produced from biomass via enzymatic hydrolysis [107]. Thus, glucose functions as a renewable carbon precursor with a well-defined chemical structure.

SEM images of the FeNC1 catalyst show that the catalyst material has a porous, wrinkled carbon structure with irregular features (Figure 4a-b). STEM images further show that the FeNC1 material contains iron-rich nanoparticles with diameters between 5–40 nm (Figure 4c-h). Additionally, these nanoparticles are surrounded by graphitic carbon shells (Figure 4d). Iron and transition metals in general are known to catalyze the graphitization of carbon, which results in the formation of graphitic carbon layers surrounding the nanoparticles [78]. STEM-EDX mapping shows an even distribution of nitrogen throughout the carbon structure, while iron is concentrated as nanoparticles (Figure 4f-h). However, iron is also distributed along the carbon structure, likely as atomically dispersed Fe centers. Between 300 and 600 °C, DCDA forms graphitic carbon nitride (g-C_3N_4), which decomposes completely during pyrolysis at 800 °C and acts as a reactive template by forming sheet-like structures, additionally doping the carbon structure with nitrogen by evolving gases [108,109]. The pores of different sizes seen in Figure 4a-b are likely formed as a result of the combination of both the NaCl template and the decomposition of g-C_3N_4.

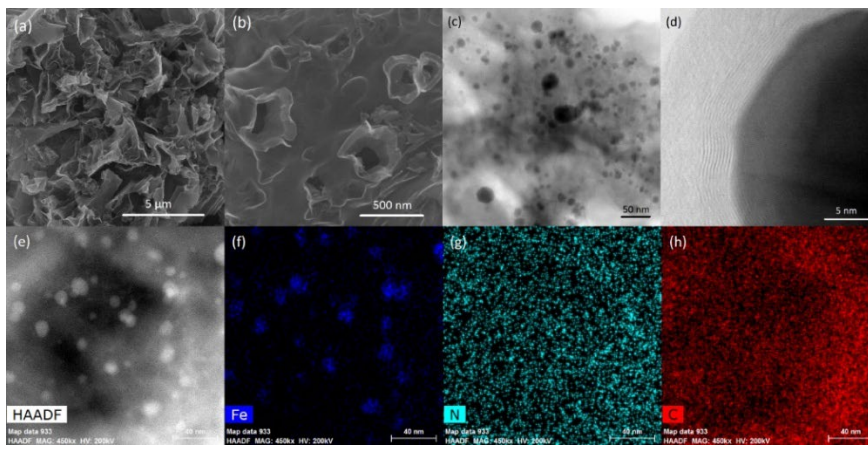

Figure 4. (a, b) SEM micrographs of FeNC1 material; (c, d) bright-field STEM images, (e) HAADF STEM image, and (f-h) corresponding EDX elemental maps of iron, nitrogen, and carbon of FeNC1 catalyst.

According to N_2 physisorption analysis, the majority of pores in the FeNC1 catalyst have a diameter of around 0.8 nm, with another small maximum at about 3.5 nm (Figure 5a). The specific surface area (SSA) of this material is 453 $m^2\ g^{-1}$ and the total pore volume (V_p) is 0.24 $cm^3\ g^{-1}$, of which 0.18 $cm^3\ g^{-1}$ (75%) is the micropore volume. A type Ib isotherm with a H4-type hysteresis loop according to the IUPAC classification was observed, which is characteristic of micro-mesoporous materials (Figure 5a, inset) [110]. XRD analysis of the FeNC1 catalyst shows that the material contains crystalline iron and iron carbide (Figure 5b). Additionally, zirconium oxide reflections originating from the ball-milling procedure are evident. Zirconium oxide has been reported to be rather inactive for ORR [111]. The Raman spectrum shows two first-order bands for the FeNC1 material – the D1 band at 1350 cm^{-1} and the G band at about 1580 cm^{-1} (Figure 5c). The D1 band corresponds to disordered carbon, while the G band corresponds to graphitic carbon. The I_{D1}/I_G ratio (integrated areas under the corresponding bands) can be used to describe the degree of graphitization of carbon-based materials. For FeNC1, this ratio is 2.6, indicating highly defective and disordered graphitic structures [112].

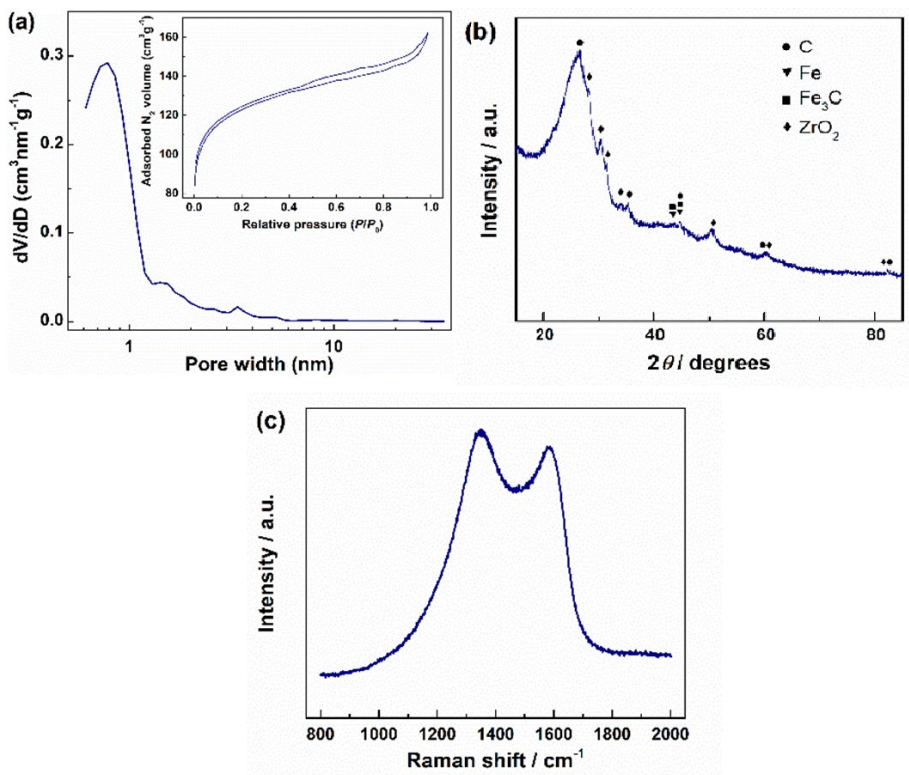

Figure 5. (a) PSD and N_2 adsorption-desorption isotherm (inset), (b) XRD pattern, and (c) Raman spectrum of FeNC1 catalyst material.

According to XPS analysis, the FeNC1 material contains carbon (74.0 at%), nitrogen (20.0 at%), oxygen (5.2 at%), sodium (0.7 at%), and iron (0.2 at%) (Figure 6a-d). The high surface nitrogen content shows effective nitrogen doping, while the surface iron content is low. Approximately 10% of the iron is in metallic form, with the other 90% corresponding to oxidized iron and nitrogen-coordinated iron (Figure 6a, inset). The N1s spectrum was deconvoluted into five peaks corresponding to pyridinic nitrogen (397.9 eV), iron-coordinated nitrogen (Fe-N_x, 399.6 eV), pyrrolic nitrogen (400.9 eV), graphitic nitrogen (402.6 eV), and oxidized nitrogen (N-O, 404.5 eV) (Figure 6b). The FeNC1 catalyst material has a high relative surface content of nitrogen as Fe-N_x centers (23%), which are known to be the main active centers for ORR [6,113]. Additionally, around 50% of the nitrogen is in the form of pyridinic-N, which is often associated with high ORR activity [114].

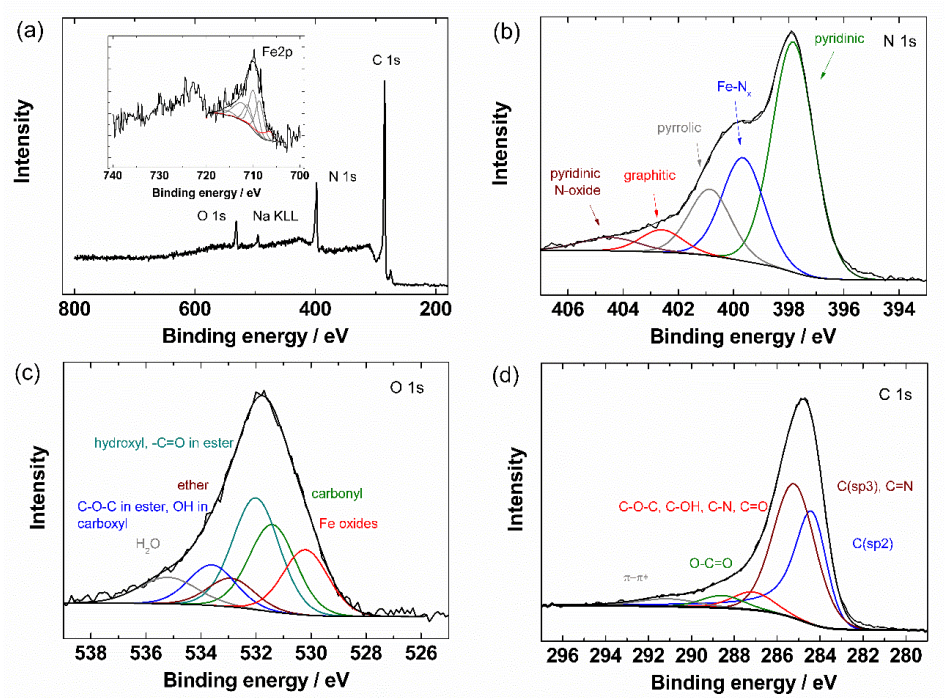

Figure 6. XPS spectra of the FeNC1 catalyst. (a) survey spectrum and detailed Fe 2p spectrum (inset); (b) N 1s detailed spectrum; (c) O 1s detailed spectrum; (d) C 1s detailed spectrum.

The synthesized materials were electrochemically characterized using the RDE method in aqueous 0.1 M KOH solution, and the RDE results are given in Table 7 and Figure 7. For the FeNC1, FeNC2, and FeNC3 materials, the amount of NaCl template during the synthesis was varied (Figure 7a). Decreasing the NaCl content four times for the FeNC2 material considerably decreased the ORR

activity, as MA decreased sixteen times and the $E_{1/2}$ decreased by about 200 mV compared to the FeNC1 catalyst. Doubling the NaCl content in the case of FeNC3, however, had a minor effect on the ORR activity. Both increasing and decreasing the NaCl content slightly increased peroxide production, as indicated by a decrease in the number of electrons transferred (n) during the reaction. For FeNC1, the main product was water, with about 10–25 % peroxide production indicated by an n value between 3.5–3.8. The iron content in the materials was varied for the FeNC4 and FeNC5 catalysts, and for comparison, the NC material was synthesized without the iron salt (Figure 7b). It is evident that iron is essential for ORR activity, as the iron-free NC material showed low ORR activity. This was indicated by a more negative E_{onset} of 230 mV and more negative $E_{1/2}$ of 250 mV compared to the FeNC1 material. Additionally, the main product of the ORR switched to peroxide, as the n values dropped to around 2.4–2.5. Both increasing and decreasing the iron content for FeNC4 and FeNC5, respectively, appeared to decrease the ORR activity, as indicated by the lower MA values and more negative $E_{1/2}$ values. Increasing the metal content in the precursor mixture generally results in more metal nanoparticles, which may be encapsulated by a graphitic carbon shell (Fe@N-C sites) [115,116]. At low metal content, Fe-N_x sites are usually most prominent. Both of these types of sites are considered active for ORR in alkaline environments, although Fe-N_x centers are considered to have higher activity [117,118]. Additionally, iron can catalyze the graphitization of carbon, which generally increases the electrical conductivity and stability of the catalyst material. However, increased graphitization of the carbon material is inversely correlated with the number of defects in the carbon structure, which can serve as active sites for ORR [70].

Table 7. ORR parameters for the catalysts in 0.1 M KOH solution, ω = 1900 rpm.

Catalyst	$E_{1/2}$, V	E_{onset}, V	MA at 0.8 V, A g^{-1}	n
FeNC1	0.75	0.92	14.2	3.5–3.8
FeNC2	0.56	0.85	0.9	3.1–3.6
FeNC3	0.77	0.94	16.6	3.3–3.6
FeNC4	0.68	0.90	6.5	3.5–3.6
FeNC5	0.67	0.90	6.0	3.4–3.6
FeNC6	0.60	0.89	2.8	2.9–3.0
FeNC7	0.74	0.92	11.4	3.8–3.9
FeNC8	0.62	0.86	2.0	3.0–3.3
NC	0.52	0.67	n.d.	2.4–2.5
Pt/C	0.86	1.00	112.5	3.9–4.0

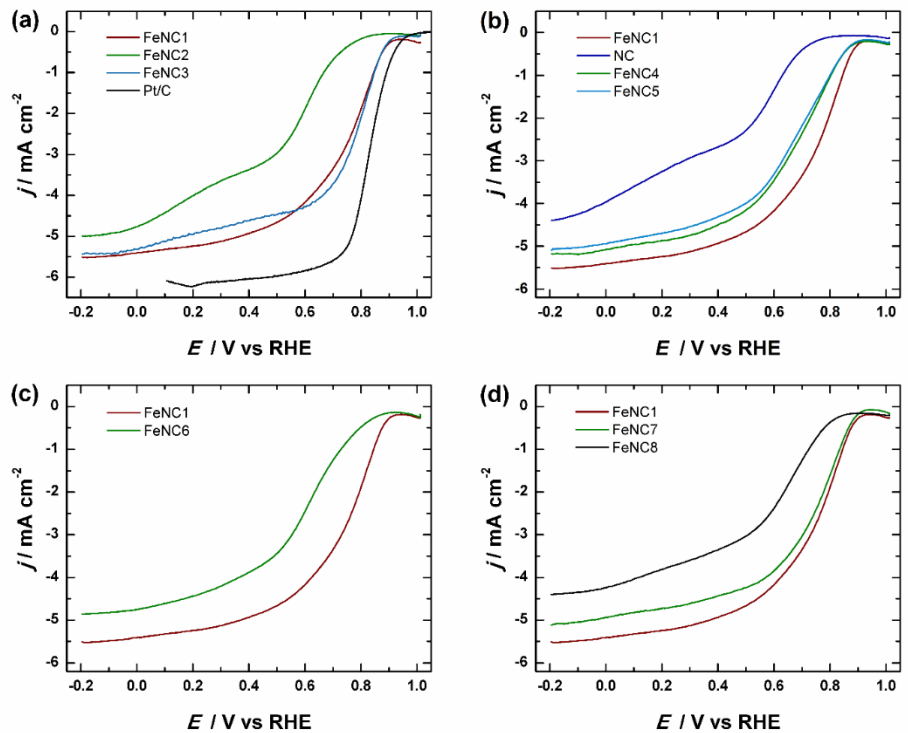

Figure 7. RDE voltammetry curves for O_2 reduction on the electrocatalysts in O_2-saturated 0.1 M KOH. ω = 1900 rpm; v = 10 mV s^{-1}.

For the FeNC6 material, the pyrolysis temperature was raised from 800 to 900 °C (Figure 7c). The melting point of NaCl is slightly above 800 °C [119], which indicates that the catalyst structure could change due to molten NaCl. Additionally, pyrolysis at higher temperatures tends to increase the graphitization of the catalyst materials and decrease the heteroatom content [120]. Raising the pyrolysis temperature had a negative effect, as the ORR activity decreased compared to FeNC1. Zhou and co-workers reported similar negative results, which they explained by the loss of the NaCl template structure, which resulted in the formation of thicker carbon nanosheets [121]. Conversely, Pan and co-workers reported better ORR activity, which was explained by enhanced graphitization of the carbon due to coverage of the catalyst by molten NaCl [119]. For the FeNC7 material, the amount of DCDA used for preparing the material was increased 3 times, which showed minor effects on the ORR activity (Figure 7d). Replacing DCDA with urea for the FeNC8 material, however, resulted in lower ORR activity. Urea forms g-C_3N_4 at around the same temperature as DCDA [122], forming pores upon its decomposition and doping the material with nitrogen in an analogous way to DCDA. However, as the activity for the FeNC8 material was lower, it is evident that this process was not optimal using urea.

To investigate the active sites for ORR, cyanide poisoning experiments were conducted. Cyanide (CN^-) anions bind irreversibly to M-N_x centers, blocking the ORR activity of these sites [71]. Comparing ORR polarization curves before and after CN^- poisoning can confirm the existence of the M-N_x centers in the material. The ORR activity for the FeNC1 material clearly decreased in the presence of 10 mM CN^-, with E_{onset} shifting negatively by 51 mV and $E_{1/2}$ by 115 mV (Figure 8a). While this confirms that the FeNC1 catalyst contains Fe-N_x centers substantially contributing to the ORR activity, some electrocatalytic activity still remains. This could be either due to Fe@N-C sites or metal-free nitrogen moieties [123,124]. Fe@N-C sites have displayed high ORR activity in alkaline media, which has been attributed to synergistic effects between the iron nanoparticle and the surrounding carbon shell [115,123,124]. Effectively, the iron core decreases the local work function on the surface of the shell by electron transfer, thereby increasing the ORR activity [115,124].

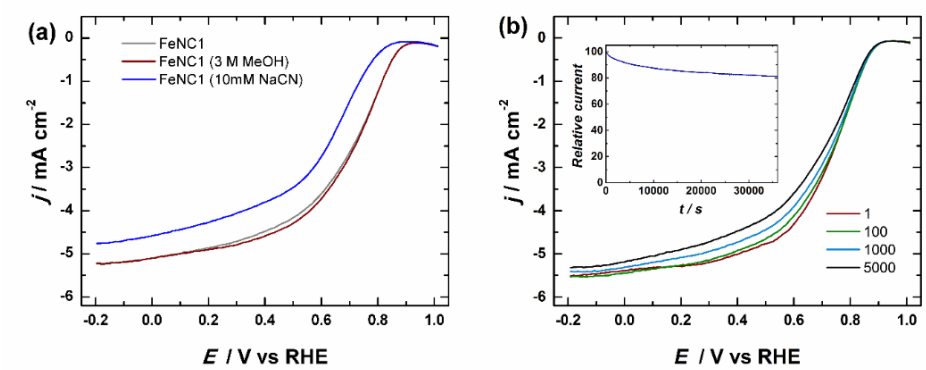

Figure 8. (a) RDE voltammetry curves for O_2 reduction using FeNC1 catalyst in 0.1 M KOH solution in the presence of 10 mM NaCN or 3 M methanol; (b) RDE voltammetry curves for O_2 reduction on FeNC1 catalyst before and after repetitive potential cycles between 1 and 0.6 V, ω = 1900 rpm; v = 10 mV s^{-1}. Inset: decrease of the ORR current in CA stability test at 0.5 V, ω = 960 rpm.

The catalysts' tolerance toward methanol was also tested. PGM-free ORR catalysts generally have a higher tolerance to methanol compared to PGM-based catalysts [125]. The ORR polarization curve for the FeNC1 catalyst is almost unchanged in the presence of 3 M methanol in 0.1 M KOH solution (Figure 8a), which shows that it could be used as a catalyst in direct methanol fuel cells.

For usage in fuel cells, the catalyst materials must also retain their ORR activity for a long duration. The FeNC1 material showed high stability in a short-term stability test for 5000 cycles in 0.1 M KOH solution, with $E_{1/2}$ decreasing by only 17 mV (Figure 8b). During a 10 h chronoamperometric test, the ORR current decreased by about 20% (Figure 8b, inset).

6.2. Electrocatalysts derived from rapeseed press cake

From the first part of the work, it was evident that the glucose-derived materials did not perform as well as anticipated, and their ORR activity remained below that of the commercial 20% Pt/C catalyst. In the second part of the work, we proceeded with hot-pressed rapeseed press cake as the organic precursor for producing electrocatalysts active for ORR and/or OER. Rapeseed press cake is a byproduct of rapeseed oil production, which is used as animal feed [126]. This material is an interesting precursor because, unlike glucose, rapeseed press cake inherently contains nitrogen and phosphorus from the fibers and proteins present in its structure, which can act as dopants in the resulting carbon material. Additionally, cobalt was used as a transition metal in addition to iron in order to investigate the effects of bimetal doping.

6.2.1. Electrocatalysts synthesized using DCDA and metal salts

The electrocatalysts were synthesized using rapeseed press cake as an organic precursor along with DCDA, iron and/or cobalt salts [II]. The synthesis process of these materials was similar to that of the materials prepared using glucose, except that the NaCl template was not used and certain materials were acid-treated and pyrolyzed again after that (Section 5.1.2, Table 4). The acid-treated material FeCoNCR-a has a similar morphology to FeNC1 according to SEM images, consisting of irregular carbon structures (Figure 9a). Additionally, larger metal-containing nanoparticles are visible in STEM images (Figure 9b,d). These nanoparticles are evenly distributed across the carbon support, with their diameters ranging from 10 nm up to 50 nm. The nanoparticles are surrounded by graphitic carbon shells, which appear to protect the nanoparticles from dissolution during the acid treatment (Figure 9c). SEM-EDX analysis shows that the acid-treated material FeNCR-a has the lowest nitrogen content (8.3±1.7 wt%) and the highest metal content (14.7±1.7 wt%), while CoNCR-a, in contrast, has the highest nitrogen content (17.9±0.5 wt%) and the lowest metal content (11.5±1.1 wt%). Additionally, the catalysts contain 11–15 wt% oxygen and 2–4 wt% phosphorus, along with calcium, magnesium, potassium, sulfur, and silicon in minor quantities. Phosphorus originates from the rapeseed precursor. STEM-EDX mapping for the FeCoNCR-a catalyst reveals evenly distributed nitrogen throughout the carbon structure, while iron, cobalt, and phosphorus are concentrated in the nanoparticles (Figure 9e-g). Additionally, the signals of iron, cobalt, and phosphorus can also be seen outside of the nanoparticles, indicating that the material also contains either very small nanoparticles or atomically dispersed sites. XRD analysis further shows that the nanoparticles consist of metal phosphides, as the main crystalline phases are Co_2P, Fe_2P, and $Fe_{1.4}Co_{0.6}P$ for the respective metal-containing materials (Figure 10a). The intensity of the reflections is lower for the acid-treated materials, which suggests that some of the metal phosphide nanoparticles were dissolved during the acid treatment process.

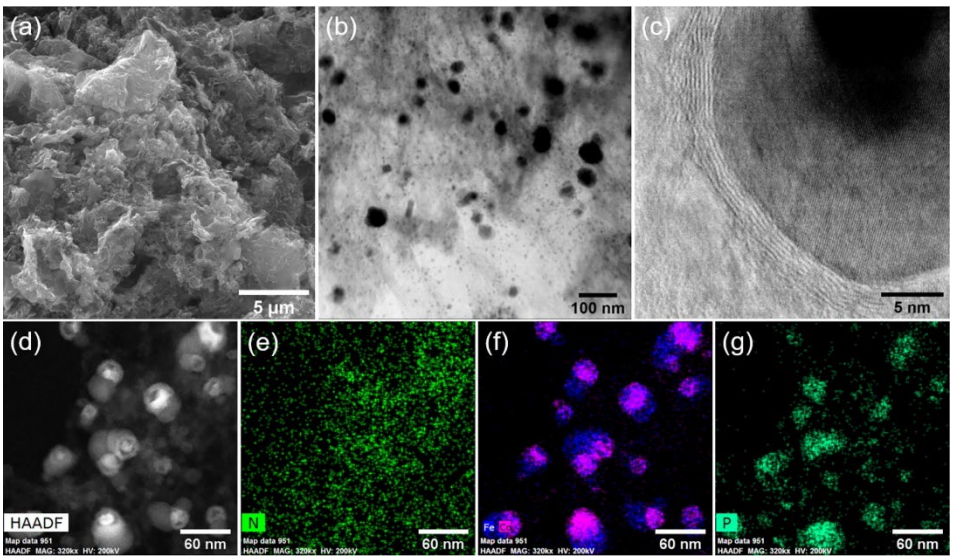

Figure 9. (a) SEM micrograph of FeCoNCR-a material; (b, c) bright-field STEM images, (d) HAADF STEM image, and (e-g) STEM-EDX elemental mappings of nitrogen, cobalt, iron, and phosphorus for FeCoNCR-a catalyst.

The PSD and SSA of the catalyst materials were studied by N_2 physisorption analysis (Figure 10b). Type III isotherms with an H3-type hysteresis loop were observed, according to the IUPAC classification (Figure 10b, inset) [110]. Before acid treatment, the SSA of the catalysts was between 130–180 $m^2\ g^{-1}$. The SSA of the materials was considerably increased after the acid washing, reaching 240, 295, and 415 $m^2\ g^{-1}$ for CoNCR-a, FeNCR-a, and FeCoNCR-a, respectively. Similarly, the V_{tot} and V_{μ} of the catalysts also increased after acid treatment, with the highest values observed for FeCoNCR-a (V_{tot} = 0.61 $cm^3\ g^{-1}$ and V_{μ} = 0.09 $cm^3\ g^{-1}$), likely due to the dissolution of metal nanoparticles not covered by a graphitic carbon shell. The PSD shows two maxima for all catalysts, one at around 2 nm and the second at around 3.5 nm, along with abundant mesopores of all sizes (Figure 10b).

The Raman spectra of the catalysts show that all of the materials are highly disordered carbon materials (Figure 10c). With the D1 band at 1350 cm^{-1} corresponding to disordered carbon and the G band at 1580 cm^{-1} corresponding to graphitic carbon, the I_{D1}/I_G ratio is higher than two for all the catalysts. For the acid-treated materials, the width of the peaks is slightly lower, indicating an increased proportion of ordered (sp^2) carbon phases and increased graphitization. Similar results were reported previously, and it is likely that some surface defects were removed during the second pyrolysis, which may result in increased graphitization [127].

From XPS analysis, it was evident that the CoNCR-a, FeNCR-a, and FeCoNCR-a materials have a high surface content of nitrogen (10–12 at%) and oxygen (5.6–7.4 at%). The surface iron content (0.8 at% for FeNCR-a and

0.5 at% for FeCoNCR-a) was lower compared to the surface cobalt content (1.9 at% in CoNCR-a and 1.2 at% in FeCoNCR-a). The detailed N1s XPS spectra were deconvoluted into several subpeaks corresponding to different nitrogen functionalities: pyridinic nitrogen (398.4 eV), metal-coordinated nitrogen (M-N_x, 399.3 eV), hydrogenated nitrogen (including pyrrolic nitrogen and hydrogenated pyridine, 400.5 eV), graphitic nitrogen (402.0 eV), bulk N-H (403.9 eV), and N-O (405 eV) (Figure 10d). For CoNCR-a, FeNCR-a, and FeCoNCR-a, the most abundant species, comprising almost 50% of nitrogen, is pyridinic N, which has often been related to increased ORR activity [114]. Additionally, a part of the nitrogen is in the form of M-N_x centers, which are known to have high ORR activity, although the relative content of these species was low in the catalysts [123].

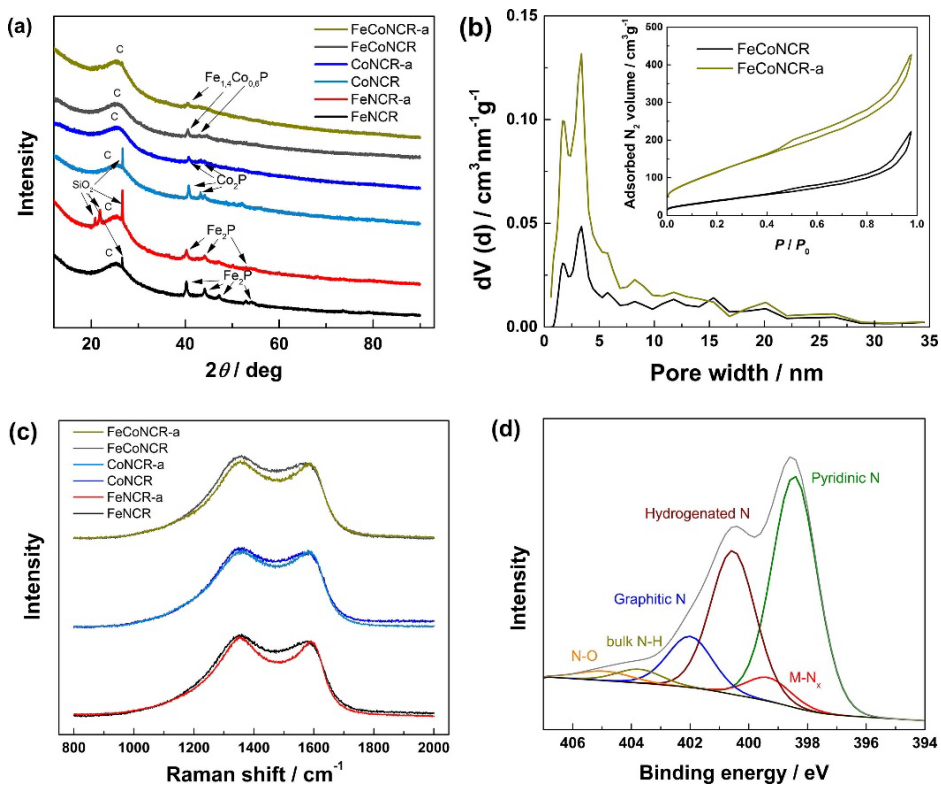

Figure 10. (a) XRD patterns of the catalyst materials; (b) PSD graph for FeCoNCR and FeCoNCR-a catalysts with corresponding N_2 physisorption isotherms (inset); (c) Raman spectra of the catalysts; (d) Deconvoluted XPS spectra in the N1s region for FeCoNCR-a catalyst material.

Oxygen electroreduction on the catalyst materials was studied by the RDE method in a 0.1 M KOH electrolyte solution, and the results are given in Table 8 and Figure 11. Low ORR activity was observed for both the pyrolyzed rapeseed press cake material CR and the metal-free catalyst NCR, as indicated by rather

negative $E_{1/2}$ and E_{onset} values. The addition of transition metals significantly increased the ORR activity, which was also slightly increased after acid treatment, likely due to the increased specific surface area (Figures 11 and 12). The FeNCR-a and FeCoNCR-a materials have a relatively high ORR onset potential (0.94 and 0.95 V, respectively). However, the commercial 20 wt% Pt/C catalyst has 20 mV more positive $E_{1/2}$ and E_{onset} values, indicating slightly higher ORR activity. The main product of the ORR for FeNCR-a and FeCoNCR-a is water, as indicated by n values between 3.7–3.9. The value of n is around 3.5 for the CoNCR-a catalyst, indicating that up to 25% of the hydroperoxide anion is produced. This has been observed in previous works [127,128] and has been explained by the slow disproportionation of peroxide on Co nanoparticles [129].

Table 8. ORR parameters of the catalysts in 0.1 M KOH solution, ω = 1900 rpm.

Catalyst	E_{onset}, V	$E_{1/2}$, V	n
CR	0.77	0.62	2.4–2.6
NCR	0.83	0.66	3.1–3.2
FeNCR	0.93	0.77	3.6–3.7
FeNCR-a	0.94	0.80	3.8–3.9
CoNCR	0.90	0.80	3.6–3.7
CoNCR-a	0.92	0.81	3.4–3.5
FeCoNCR	0.92	0.81	3.7–3.8
FeCoNCR-a	0.95	0.81	3.7–3.9
20 wt% Pt/C	0.97	0.83	3.9–4

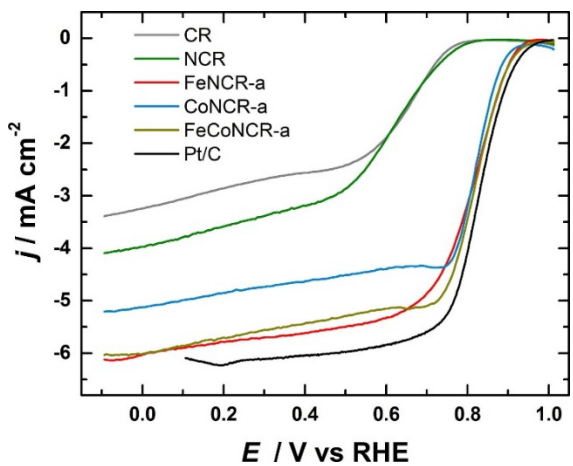

Figure 11. RDE voltammetry curves for O_2 reduction on various catalysts in O_2-saturated 0.1 M KOH at 1900 rpm, v = 10 mV s^{-1}.

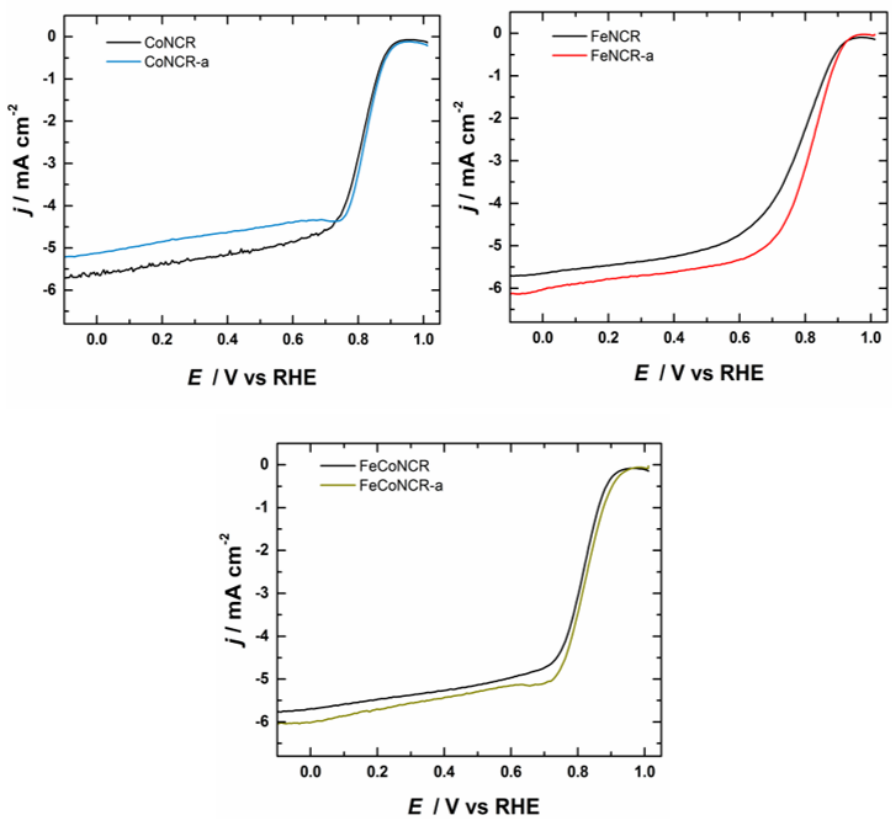

Figure 12. Comparison of the RDE polarisation curves of O_2 reduction before and after acid-treatment in 0.1 M KOH solution. ω = 1900 rpm, v = 10 mV/s.

The role of different transition metal-containing centers and nitrogen-containing species for ORR is unclear. It is evident from Figure 11 that the presence of transition metal salts in the synthesis process is necessary to obtain high ORR activity. M-N_x centers are most often considered active sites for ORR [114,118, 123], while M@N-C centers are also known to have high activity in alkaline media [70,115,118,130]. As shown by STEM and XRD analysis, the catalysts contained metal phosphide nanoparticles, while XPS analysis suggested the existence of M-N_x centers. We performed additional RDE experiments in the presence of CN^- anions, which are known to irreversibly bind to M-N_x sites and inhibit ORR activity [71,118]. The results of this experiment show that the $E_{1/2}$ of the FeCoNCR-a catalyst decreased by 50 mV and E_{onset} decreased by 80 mV, confirming the presence of M-N_x centers and showing that they have a large contribution to the ORR activity of the catalyst (Figure 13a). The remaining ORR activity was still higher than for the metal-free catalyst NCR, which indicates that other metal-containing sites are also highly active for ORR. For example, the increased ORR activity for Fe@N-C sites has been explained by the decreased

local work function of the nitrogen-doped carbon due to electron transfer from the metal core [115]. High ORR activity for electrocatalysts containing nanoparticles of cobalt phosphides [131,132], iron phosphides [133,134] and bimetallic cobalt and iron phosphides [135] in heteroatom-doped carbon has been previously reported. The increased ORR activity was attributed to the positive effects of the metal phosphide nanoparticles on the electrocatalytic activity of the outer carbon layers. The increased ORR activity of metal-containing catalysts could also be partly due to the increased graphitization of the catalyst materials, as transition metals can catalyze the graphitization of carbon [136].

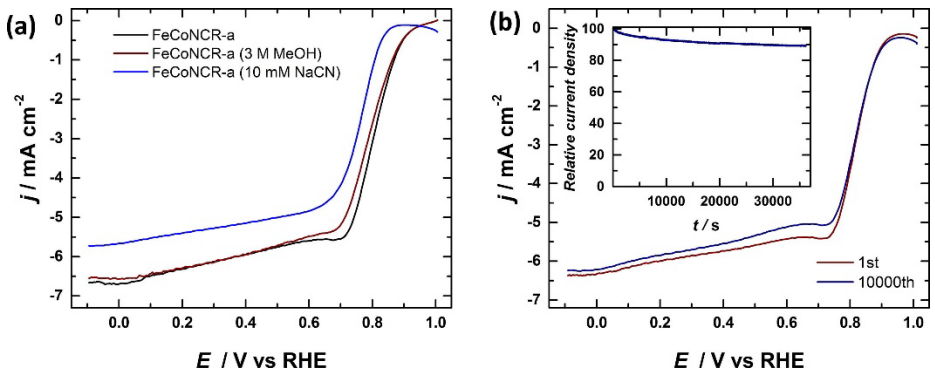

Figure 13. (a) RDE voltammetry curves for O_2 reduction using FeCoNCR-a catalyst in 0.1 M KOH and in the presence of 10 mM NaCN or 3 M methanol; (b) RDE voltammetry curves for O_2 reduction on FeCoNCR-a catalyst before and after 10000 potential cycles between 1 and 0.4 V. ω = 1900 rpm; v = 10 mV s^{-1}. Inset: chronoamperometric response at 0.5 V, ω = 960 rpm.

To evaluate the possibility of applying the catalysts in direct methanol fuel cells, the ORR activity of the FeCoNCR-a catalyst was also tested in 0.1 M KOH solution containing 3 M methanol. The $E_{1/2}$ value decreased by only 15 mV, showing high tolerance to methanol (Figure 13a). Additionally, the durability of catalysts is important for their practical usage in fuel cells. The short-term stability test showed that the FeCoNCR-a material has high stability, as the $E_{1/2}$ value remained almost unchanged (Figure 13b). The current decayed by only 10% during a 10 h chronoamperometric test (Figure 13b, inset).

Despite good ORR performance in RDE analysis, the FeCoNCR-a catalyst showed a moderate P_{max} of 131 mW cm^{-2} at 0.5 V in H_2/O_2 AEMFC tests (Figure 14). It is difficult to directly compare fuel cell results with literature data due to different experimental conditions, like the specific membrane used and the AEMFC setup itself [34,127,137]. Further optimizing the conditions used in this work could lead to better performance. However, this result does show that electrocatalysts derived from rapeseed press cake can be successfully used as cathode catalysts for AEMFCs.

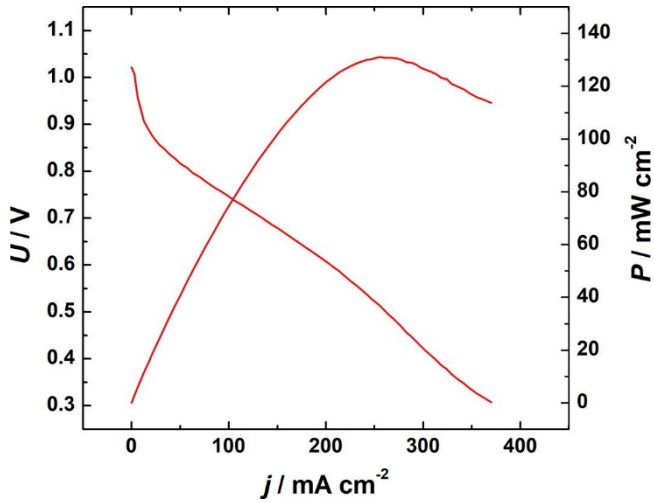

Figure 14. Polarization and power density curves for H_2/O_2 (50% RH) single-cell AEMFC with the MEA prepared using AEMION+ (10 µm) AEM, FeCoNCR-a (2 mg cm^{-2}) cathode catalyst, and Pt–Ru/C (0.8 $mg_{Pt\text{-}Ru}$ cm^{-2}) anode catalyst. T = 60 °C.

6.2.2. Templated electrocatalysts for AEMFC

From the previous work [II], it was evident that while the materials showed high electrocatalytic activity, the performance of the FeCoNCR-a catalyst in an AEMFC was not good. Thus, we proceeded with the addition of magnesium acetate as a template precursor to the synthesis process in an attempt to optimize the porous structure of the catalyst material [III]. The synthesis process was effectively identical to the previous process, except for the addition of magnesium acetate during the first pyrolysis (Section 5.1.2, Table 5). Magnesium acetate decomposes to magnesium oxide during the high-temperature pyrolysis and forms a mesoporous structure in the carbon material after its removal with dilute hydrochloric acid.

According to SEM images (Figure 15), the FeNCR-MgAc-3-1 material has a similar irregular sheet-like carbon structure to the material FeCoNCR-a prepared without the template [II] (Figure 9). However, compared to the FeCoNCR-a catalyst, the nanoparticles in FeNCR-MgAc-3-1 are much smaller (less than 10 nm) and appear to be more dispersed throughout the carbon structure (Figures 15b,d). Additionally, the nanoparticles are covered with graphitic carbon shells (Figure 15c), similar to the materials studied in previous works [I, II]. The STEM-EDX elemental mapping shows that the nanoparticles contain iron and phosphorus, along with evenly dispersed iron, phosphorus, and nitrogen in the carbon structure (Figure 15e-g). From SEM-EDX analysis, the FeNCR-MgAc-3-1 material has lower nitrogen and iron contents compared to the untemplated FeNCR-a catalyst [II] (5.7±2.3 vs 8.3±1.7 wt% and 8.7±2.0 vs 14.7±1.7 wt%, respectively). It is likely that the templating procedure created a more porous material and exposed more nanoparticles to the acid treatment, thus decreasing

the iron content in the FeNCR-MgAc-3-1 material. Additionally, FeNCR-MgAc-3-1 contains an increased amount of magnesium compared to the FeNCR-a material. These results agree with MP-AES results, which show that FeNCR-MgAc-3-1 has a bulk Fe content of around 5 wt% and a Mg content of around 2 wt%. Most likely, the magnesium retained in the materials is present as atomically dispersed Mg-N_x moieties, which do not dissolve during the acid leaching [138]. This agrees with the results of XRD analysis, which shows no MgO peaks after acid treatment (Figure 16). XRD analysis also indicates that the nanoparticles seen in STEM images consist of iron phosphide. Interestingly, before acid treatment, the XRD spectrum of the material also shows peaks corresponding to magnesium cyanamide ($MgCN_2$) in addition to magnesium oxide. Magnesium cyanamide forms during high-temperature pyrolysis of the magnesium acetate template precursor in the presence of a nitrogen-rich source like DCDA [92,139]. The reflections of magnesium cyanamide and magnesium oxide are not seen in the final material FeNCR-MgAc-3-1, showing the success of the acid treatment.

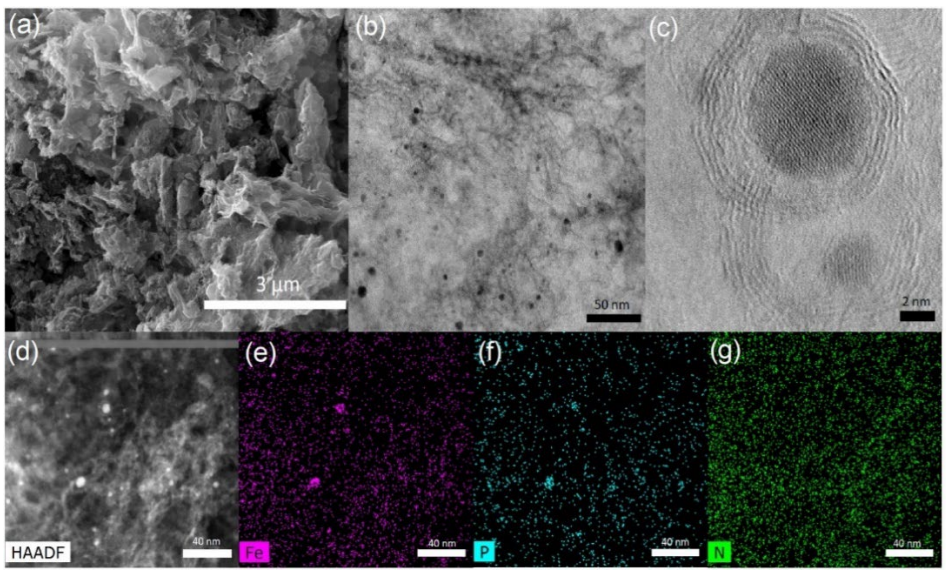

Figure 15. (a) SEM micrograph, (b, c) bright-field STEM images, (d) HAADF STEM image, and (e, f, g) STEM-EDX elemental mappings of iron, phosphorus, and nitrogen for FeNCR-MgAc-3-1 material.

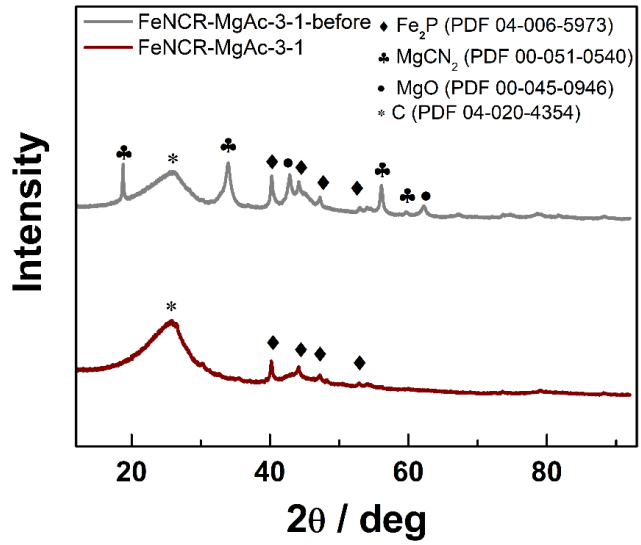

Figure 16. XRD patterns of FeNCR-MgAc-3-1 before and after acid treatment.

Table 9. Specific surface area (S_{BET} and S_{dft}), total pore volume (V_{tot}) and micropore volume (V_{micro}) of catalyst materials via N_2 physisorption analysis.

Catalyst	S_{BET}, $m^2\ g^{-1}$	S_{dft}, $m^2\ g^{-1}$	V_{tot}, $cm^3\ g^{-1}$	V_{micro}, $cm^3\ g^{-1}$
FeNCR-a [II]	295	273	0.39	0.08
FeNCR-MgAc-3-1 [III]	357	308	0.57	0.07
FeNCR-MgAc-1-1 [III]	378	324	0.58	0.08

The N_2 physisorption analysis shows that the templated material FeNCR-MgAc-3-1 had roughly 20% higher SSA and almost 50% higher total pore volume than the untemplated FeNCR-a material (Table 9). The FeNCR-MgAc-1-1 material was prepared using an increased amount of the template precursor, but this did not increase the SSA by a large amount compared to FeNCR-MgAc-3-1. According to the PSD analysis, all materials have the majority of pores with diameters around 3–4 nm, but templated materials have a higher amount of larger mesopores compared to the untemplated FeNCR-a material (Figure 17a). According to the IUPAC classification, all materials have type III isotherms with an H3-type hysteresis loop (Figure 17a, inset) [110]. Both magnesium acetate and DCDA contribute to the formation of the porous structure of the catalyst materials. Magnesium acetate decomposes to magnesium oxide at around 200–250 °C, and the removal of magnesium oxide during the acid treatment leaves behind a porous structure [140]. DCDA forms g-C_3N_4 between 300 and 600 °C,

which decomposes to reactive nitrogen gases during further temperature increase, also forming a porous structure [108,109].

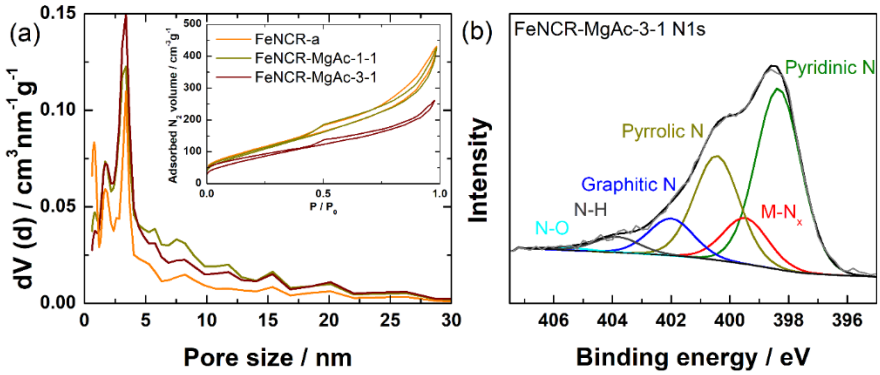

Figure 17. (a) PSD curves and N_2 physisorption isotherms (inset) of catalyst materials. (b) Deconvoluted XPS spectrum for FeNCR-MgAc-3-1 in the N1s region.

From XPS analysis, the FeNCR-MgAc-3-1 material contains mostly carbon, nitrogen, oxygen, phosphorus, and iron, with a low quantity of magnesium. The oxygen content of 13.2 at% for FeNCR-MgAc-3-1 has almost doubled compared to the untemplated FeNCR-a material (7.2 at%). The deconvoluted XPS spectrum in the N1s region for the FeNCR-MgAc-3-1 material is shown in Figure 17b. A significant increase in the relative amount of nitrogen in the form of M-N_x centers is observed, reaching 11.9% for FeNCR-MgAc-3-1 compared to 1.3% for FeNCR-a. It is likely that these are mostly Fe-N_x centers, which are considered highly active ORR sites [15,114]. However, it is possible that Mg-N_x centers also contribute to this XPS peak. Pyridinic nitrogen is the most abundant N species for both FeNCR-a and FeNCR-MgAc-3-1, and it has often been associated with increased ORR activity [15,114]. Surface phosphorus content was low at 0.4 at%. The P2p XPS peak was deconvoluted into subpeaks corresponding to C-O-P (134.1 eV), C-P-O (133.0 eV), and C_3-P=O (132.2 eV) functional groups [141]. Catalyst materials doped with phosphorus or both nitrogen and phosphorus have shown improved ORR activity due to favorable charge redistribution and a high degree of edge defects [14,15,142].

The synthesized electrocatalysts were electrochemically characterized in 0.1 M KOH solution using the RDE method (Figure 18a–b, Table 10). The material CR-MgAc-2-1, prepared using only rapeseed press cake and magnesium acetate, showed rather low ORR activity. For iron-containing materials, the addition of magnesium acetate in the synthesis enhanced the ORR activity, as the $E_{1/2}$ for the templated materials increased by 20–40 mV compared to the untemplated FeNCR-a material. Halving the metal content for the 05FeNCR-MgAc-3-1 material or doubling it for the 2FeNCR-MgAc-3-1 material slightly decreased the ORR activity (Figure 18b). FeNCR-MgAc-3-1 showed the best $E_{1/2}$ value at 0.84 V, which was comparable to that of the commercial 20 wt% Pt/C catalyst. The

value of *n* was near 4 for the materials according to K-L analysis, suggesting a $4e^-$ or $2\times2e^-$ ORR pathway (Table 10). The RRDE technique can directly evaluate the amount of HO_2^- produced via the 2-electron ORR pathway. According to RRDE analysis, the *n* value is around 3.7–3.9, corresponding to about 8–12% HO_2^- yield for all the catalysts. K-L analysis showed *n* values above 4 for FeNCR-MgAc-5-1, while, according to the RRDE analysis, the value of *n* was around 3.7–3.8. The K-L analysis assumes that the surface of the electrode is flat and uniform, which is not generally valid for porous catalyst materials, like the ones used in this work [99]. However, for the other materials, the results of the RRDE analysis and K-L analysis were in good agreement.

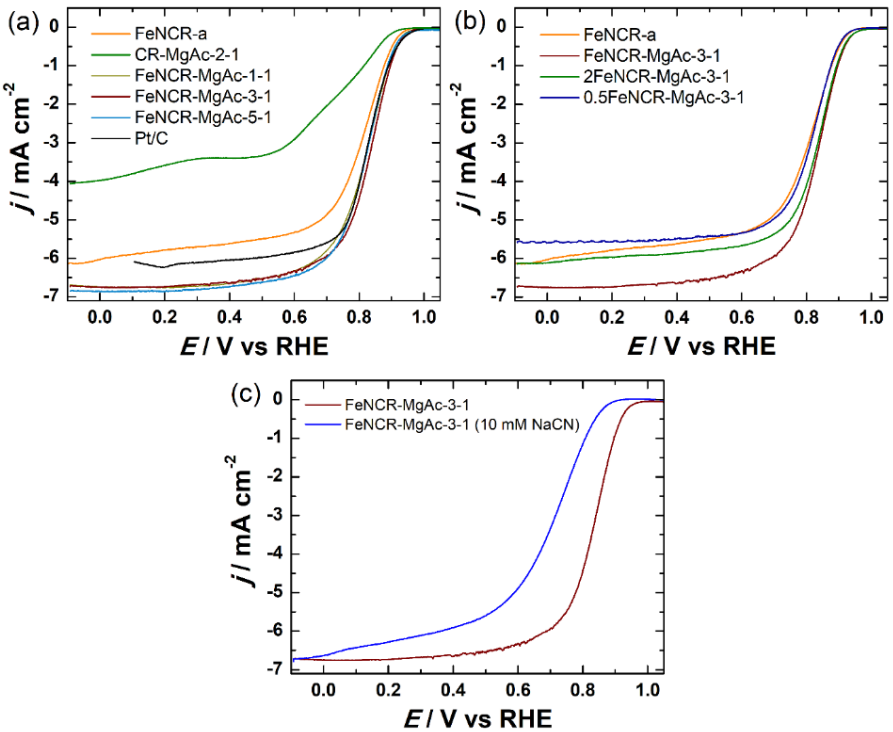

Figure 18. (a, b) ORR polarization curves of different catalyst materials in O_2-saturated 0.1 M KOH solution and (c) in the presence of 10 mM NaCN. ω = 1900 rpm, ν = 10 mV s^{-1}.

Table 10. ORR parameters of different catalysts in 0.1 M KOH, ω = 1900 rpm.

Catalyst	E_{onset}, V	$E_{1/2}$, V	MA at 0.8 V, A g^{-1}	n
FeNCR-a [II]	0.94	0.80	-	3.8 – 3.9
CR-MgAc-2-1 [III]	0.92	0.70	8	2.5 – 2.7
FeNCR-MgAc-1-1 [III]	0.95	0.82	43	4 – 4.1
FeNCR-MgAc-3-1 [III]	0.97	0.84	56	3.8 – 4
FeNCR-MgAc-5-1 [III]	0.94	0.82	44	4.2 – 4.3
2FeNCR-MgAc-3-1 [III]	0.95	0.83	56	3.8 – 3.9
0.5FeNCR-MgAc-3-1 [III]	0.94	0.82	37	3.6 – 3.7
20 wt% Pt/C [III]	0.97	0.83	51 (255 A g_{Pt}^{-1})	3.9 – 4

To investigate the active sites for ORR, the RDE experiments were performed in the presence of 10 mM NaCN. As noted in earlier sections, cyanide anions inhibit the ORR activity of M-N_x centers by strongly binding to these sites [71]. The $E_{1/2}$ value decreased by 135 mV and E_{onset} by 44 mV for the FeNCR-MgAc-3-1 material in the presence of 10 mM NaCN, indicating a significant contribution of Fe-N_x sites to the ORR activity. The remaining ORR activity can be attributed to M@N-C sites and nitrogen-containing moieties. Similar to previous catalysts [II], STEM and XRD analysis confirmed the presence of iron phosphide nanoparticles. It has been suggested that carbon-encapsulated iron phosphides enhance the electrocatalytic activity of the surrounding nitrogen-doped carbon [133,134]. Additionally, phosphorus doping has been suggested to improve the ORR activity of the catalysts via charge redistribution [14,15,142]. For the catalyst materials in this work, the surface content of phosphorus according to XPS analysis is low, which indicates that phosphorus likely has a limited impact on the ORR activity.

The durability of catalysts is important for practical usage in AEMFCs [143]. In the short-term stability test, the FeNCR-MgAc-3-1 material showed stable performance with E_{onset} staying the same and $E_{1/2}$ decreasing by 10 mV (Figure 19a). The ORR current decreased by 13% during a 10 h chronoamperometric test (Figure 19a, inset).

The performance of fuel cells is more significantly affected by the structure and composition of the catalyst layers compared to RDE analysis, which is why it is necessary to assess the catalysts in fuel cells [137]. In an AEMFC, a P_{max} of 355 mW cm^{-2} was achieved with the FeNCR-MgAc-3-1 cathode catalyst (Figure 19b). This indicates that using the Mg-based template in the synthesis was beneficial, as the results are significantly improved compared to the previous results of P_{max} = 131 mW cm^{-2} achieved with the untemplated FeCoNCR-a material [II].

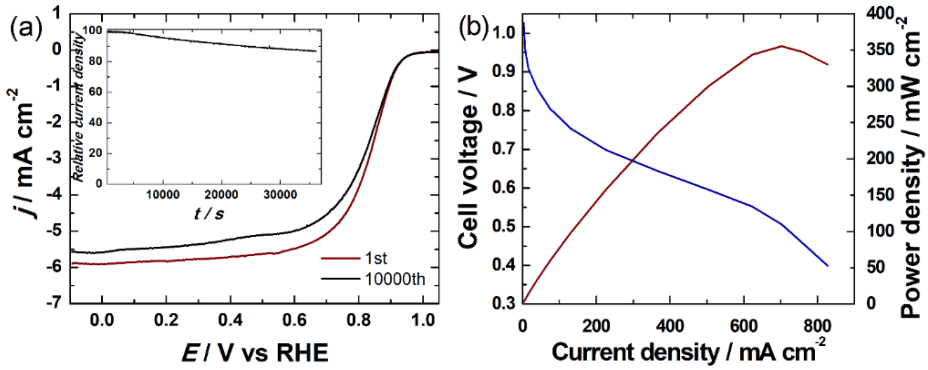

Figure 19. (a) ORR polarization curves for FeNCR-MgAc-3-1 catalyst before potential cycling and after 10000 cycles between 1.0 and 0.4 V. ω = 1900 rpm, ν = 10 mV s^{-1}. Inset: decrease of the ORR current in CA stability test at 0.5 V, ω = 960 rpm. (b) Single cell AEMFC polarization and power density curves with FeNCR-MgAc-3-1 cathode catalyst. T = 80 °C, O_2/H_2 flowrates of 0.1 NLPM and cathode catalyst loading of 0.92 mg cm^{-2}.

6.2.3. Templated electrocatalysts for RZAB

As the magnesium acetate templating procedure produced highly active electrocatalysts for ORR, we decided to use this synthesis method for the production of bifunctional materials. The synthesis procedure remained the same as that for article [III], except that nickel salts were used instead of cobalt salts in order to increase the OER activity of the catalyst materials and thereby achieve high bifunctional activity (Section 5.1.2, Table 5) [IV].

Similar to previous catalysts, the prepared materials exhibit a general structure of sheet-like carbon layers (Figures 20 and 21). Additionally, carbon nanotubes (CNTs) are seen on the carbon sheets. The number of CNTs increases with the amount of metal used in the preparation of the materials, with the 4Fe4NiNCR material containing the highest number of CNTs. Transition metals are known to catalyze the formation of CNTs [144,145]. STEM images also show that graphitic carbon layers have been formed around the metal nanoparticles (Figure 21d,e). STEM-EDX analysis for the 4Fe4NiNCR material shows abundant iron- and nickel-containing carbon-covered nanoparticles, along with evenly distributed iron, nickel, nitrogen, and phosphorus (Figure 21d-j). Iron and nickel appear to be distributed on carbon as single atoms or very small clusters, as indicated by numerous bright dots observed on the carbon sheets in high-resolution HAADF-STEM imaging (Figure 21f). According to the SEM-EDX analysis, the total metal content for the FeNiNCR, 2FeNiNCR, 2Fe2NiNCR, and 4Fe4NiNCR materials is 8.3, 16.2, 14.5, and 19.4 wt%, respectively. It is likely that any metal particles not covered by graphitic carbon layers were removed during the acid treatment, which limits the maximum possible metal content in the catalysts.

XRD analysis indicates that the catalyst materials contain metal phosphides in the form of Fe_2P, Ni_2P, or $Ni_{12}P_5$. Additionally, bimetallic phosphides ($Fe_{1.72}Ni_{1.28}P$

and FeNiP) and Fe_3Ni_2 alloy can be detected in the 2Fe2NiNCR catalyst. For the 4Fe4NiNCR material, the main crystalline phase is an iron-nickel alloy ($Fe_{0.65}Ni_{0.35}$), in accordance with spatially correlated STEM-EDX signals for the metal-containing nanoparticles observed on the elemental mappings (Figure 21h-i).

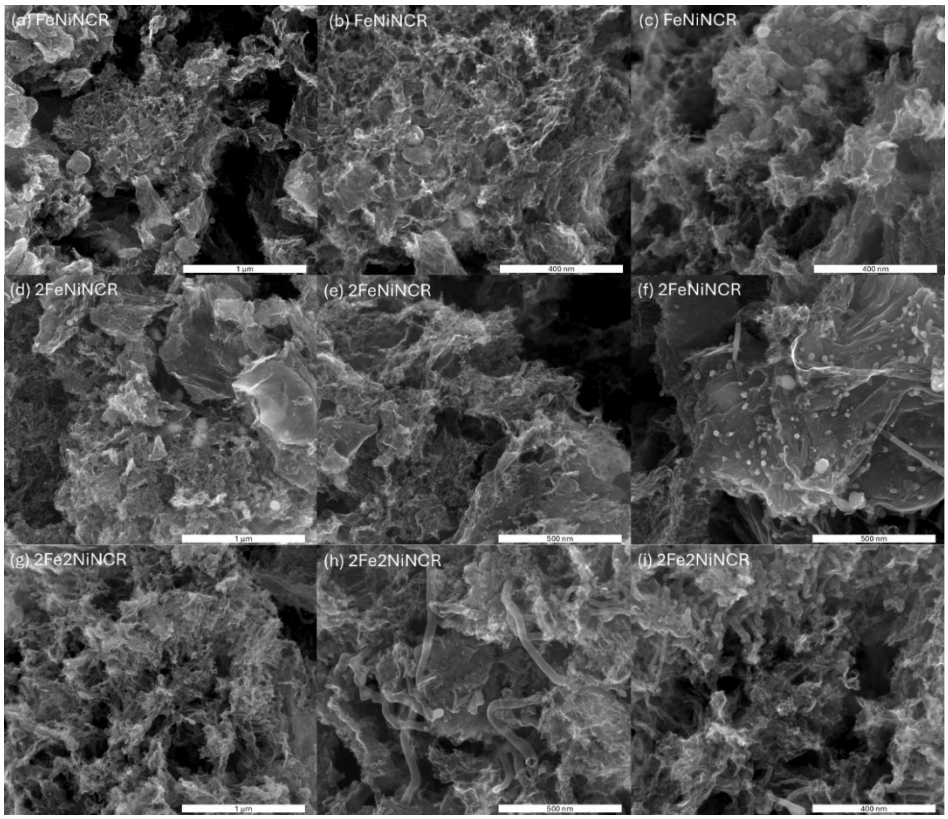

Figure 20. SEM images for (a-c) FeNiNCR, (d-f) 2FeNiNCR, and (g-i) 2Fe2NiNCR materials.

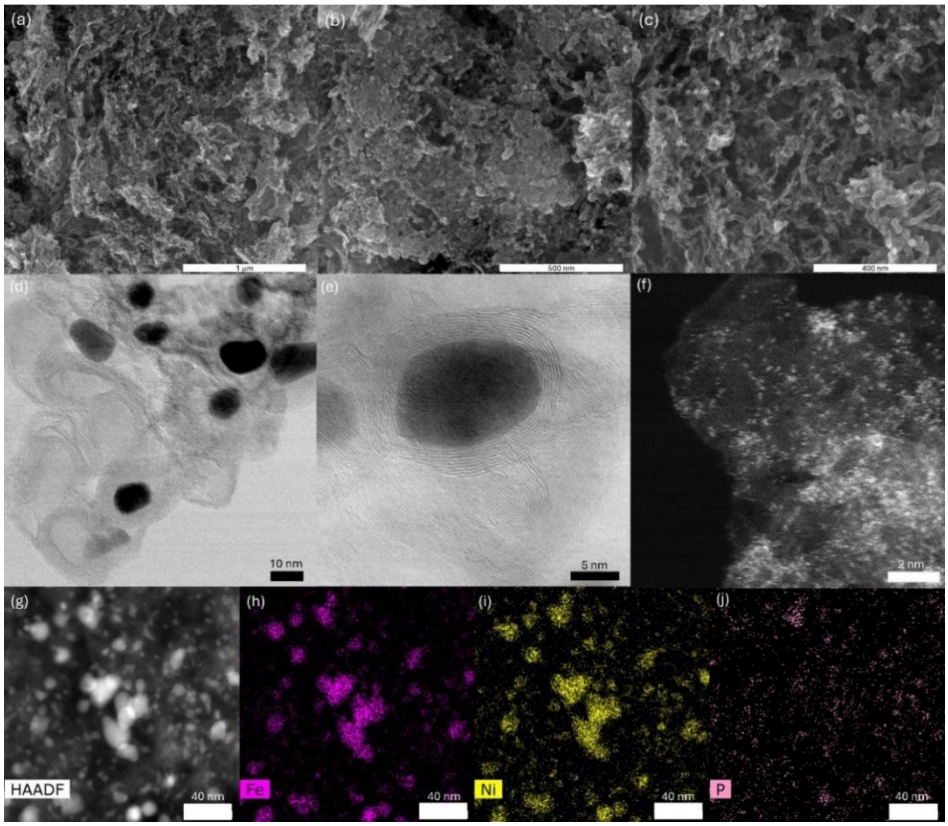

Figure 21. (a-c) SEM micrographs, (d, e) bright-field STEM images, (f, g) HAADF STEM images, and (h-j) STEM-EDX elemental mappings of iron, nickel, and phosphorus for 4Fe4NiNCR material.

Additionally, SEM-EDX analysis indicated that the heteroatom (N, O, P) content in the catalyst materials decreased with increasing metal content, with the 4Fe4NiNCR material having less than half the heteroatom content of FeNiNCR. This may be explained by the increased graphitization of the carbon structure, which is also seen in the Raman spectra (Figure 22a) [146]. After normalizing the spectra to the intensity of the G band, the spectra were further fitted using the five Voigt-shaped band model to the G (1590 cm^{-1}), D1 (1355 cm^{-1}), D2 (1615 cm^{-1}) D3 (1490 cm^{-1}), and D4 bands (1195 cm^{-1}) [112]. For highly disordered carbon materials, the Raman band commonly labelled as G is a superposition of the G and D2 bands [147]. Therefore, instead of the I_D/I_G ratio, the $I_{D1}/(I_G + I_{D2})$ ratio was used. The $I_{D1}/(I_G + I_{D2})$ ratios are 2.5, 2.6, 2.2, and 2.1 for FeNiNCR, 2FeNiNCR, 2Fe2NiNCR, and 4Fe4NiNCR materials, respectively. The decrease in these ratios with increasing metal content indicates that the structural disorder of carbon decreases and graphitization increases [112,146]. XPS results were consistent with SEM-EDX analyses, indicating that the surface heteroatom content of the catalyst materials decreased with increasing metal content. The

deconvoluted N1s XPS spectrum for the 4Fe4NiNCR material is shown in Figure 22d. All of the materials have around 11–16% of surface nitrogen in the form of M-N_x centers, which are considered to be the main ORR-active sites [21]. Pyridinic N, which has also been associated with high ORR activity [114], is the largest fraction of nitrogen at around 49–55%.

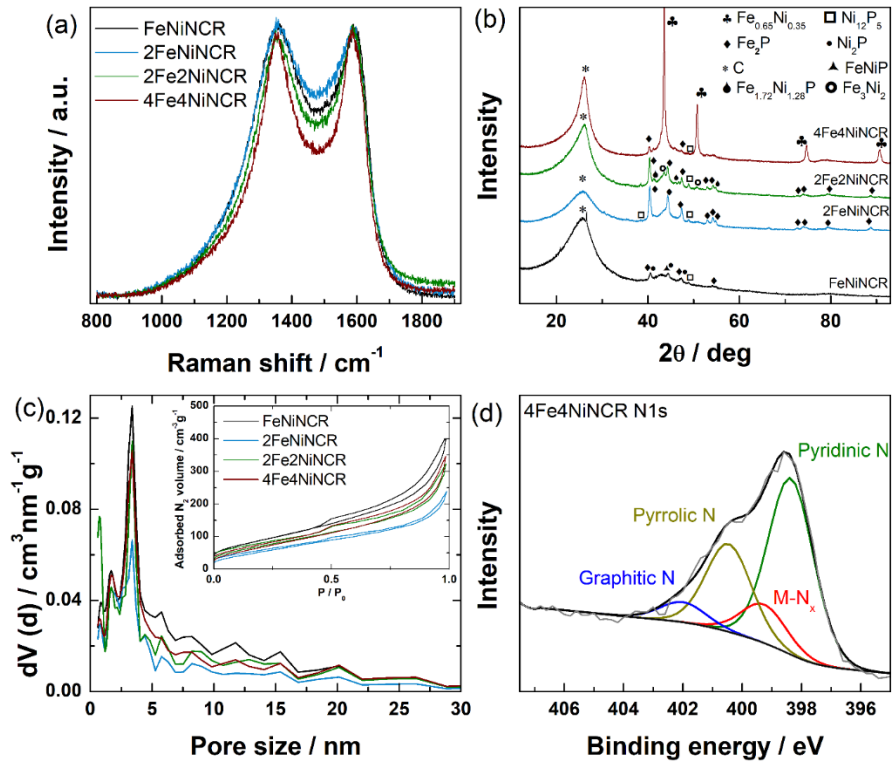

Figure 22. (a) Raman spectra, (b) XRD patterns and (c) PSD graphs for various catalyst materials. Inset: N_2 physisorption isotherms. (d) XPS N1s spectra for 4Fe4NiNCR material.

All the materials have a similar PSD, with the most pores around 3–4 nm, along with varying amounts of mesopores at higher pore sizes, according to the N_2 physisorption analysis (Figure 22c). The SSA of the materials is also similar, with values of 318, 194, 254, and 243 $m^2\ g^{-1}$ for FeNiNCR, 2FeNiNCR, 2Fe2NiNCR, and 4Fe4NiNCR materials, respectively. Similar to previous work [III], both magnesium acetate and DCDA contribute to the structure of the 4Fe4NiNCR material. During pyrolysis, magnesium acetate decomposes, forming magnesium oxide and, in the presence of a nitrogen source, magnesium cyanamide particles, which are removed during the acid-treatment and leave behind a porous structure [III]. DCDA forms graphitic carbon nitride (g-C_3N_4) layers during pyrolysis,

which decompose at higher temperatures (>600 °C) and introduce nitrogen into the material [108,109,148].

Table 11. ORR and OER parameters of different catalyst materials in 0.1 M KOH, ω = 1900 rpm.

Catalyst	E_{onset}, V	$E_{1/2}$, V	$E_{j=10}$,V	ΔE, V	n
FeNCR [IV]	0.94	0.84	1.80	0.96	3.8 – 3.9
NiNCR	0.86	0.74	-	-	2.8 – 2.9
FeNiNCR	0.92	0.81	1.67	0.86	3.4 – 3.5
2FeNiNCR	0.95	0.82	1.65	0.83	3.5 – 3.6
2Fe2NiNCR	0.95	0.83	1.64	0.81	3.4 – 3.5
4Fe4NiNCR	0.93	0.81	1.60	0.79	3.4 – 3.5
20 wt% Pt/C	0.97	0.84	-	-	3.9 – 4
50:25:25 PtRu/C	0.99	0.85	1.60	0.75	3.4 – 3.6

The ORR and OER processes were investigated by RDE in 0.1 M KOH solution. All of the bimetallic catalysts showed high ORR activity, but the OER activity varied more (Figure 23a,b and Table 11). The $E_{j=10}$ value (potential at which the OER current density reaches 10 mA cm^{-2}) decreased with increasing metal content, from 1.67 V for FeNiNCR to 1.60 V for 4Fe4NiNCR. The 4Fe4NiNCR material showed the lowest $E_{j=10}$ and the best bifunctional performance with a ΔE = 0.79 V (ΔE is the difference between $E_{1/2}$ and $E_{j=10}$). In comparison, the monometallic catalysts FeNCR [IV] and NiNCR exhibited low bifunctional activity. Iron- and nickel-containing bimetallic catalysts are generally more active for OER than monometallic ones due to various synergistic effects [149]. All the bimetallic catalyst materials showed n values of around 3.4–3.5 for ORR according to the K-L analysis [22], which corresponds to approximately 25% HO_2^- yield. However, in RZABs the catalyst loading on the GDL is much higher – about 1.5 mg cm^{-2} compared to 0.2 mg cm^{-2} used for the RDE tests in this work. The amount of free HO_2^- produced may be lower than during the RDE experiment, because HO_2^- can be further reduced to OH^- ions during diffusion through the catalyst layer [21].

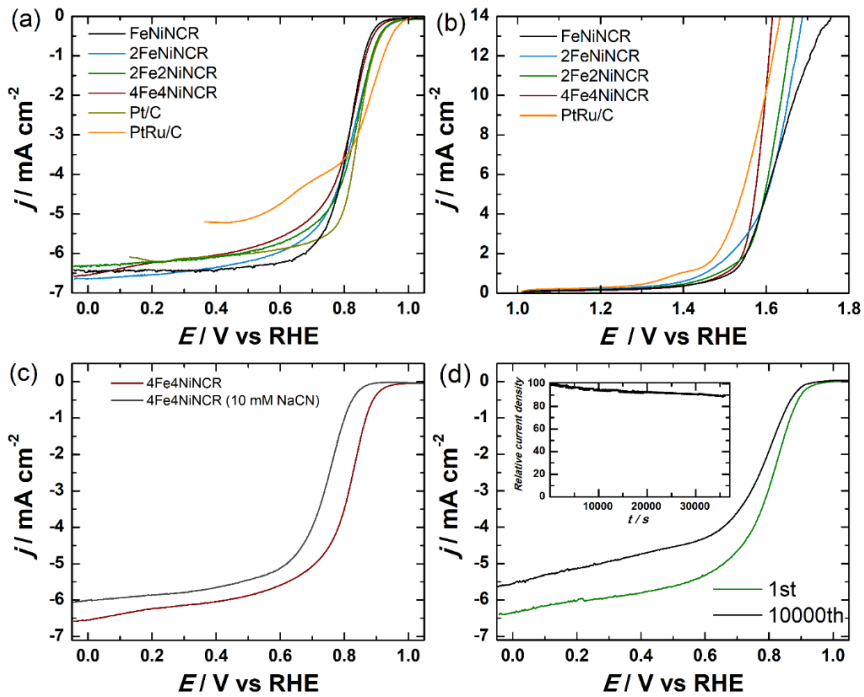

Figure 23. (a) ORR and (b) OER polarization curves for various catalyst materials in O_2-saturated 0.1 M KOH. (c) ORR polarization curve in the absence and presence of 10 mM NaCN in 0.1 M KOH. (d) ORR polarization curves for 4Fe4NiNCR before and after 10000 cycles between 1 and 0.4 V. Inset: relative current in CA stability test at 0.5 V. ω = 1900 rpm, ν = 10 mV s^{-1}.

Additional RDE tests were performed in the presence of 10 mM NaCN in 0.1 M KOH solution in order to characterize the electrochemically active sites for the 4Fe4NiNCR catalyst. As noted earlier, CN^- ions bind strongly to M-N_x centers, inhibiting the ORR process and confirming the presence of these centers [71]. The $E_{1/2}$ shifted negatively by 73 mV and the E_{onset} by 60 mV, confirming the presence of M-N_x centers and their key role in the ORR electrocatalytic activity of the 4Fe4NiNCR catalyst (Figure 23c). As the catalyst still retained ORR activity, this suggests the presence of additional electrocatalytically active sites, such as nitrogen-containing moieties and M@N-C nanoparticles [21].

The active sites for OER can be located on the surface of metal nanoparticles, which are restructured during the OER electrocatalysis [48]. The OER is thought to proceed via a four-step OH^- adsorption mechanism, which includes metal-oxo (MO) and metal hydroperoxide (MOOH) intermediates, and for which bimetallic nickel- and iron-based materials have shown high activity [48,149,150]. Additionally, OER may occur on heteroatom-doped carbon surface, as it has been shown via DFT calculations that for certain nitrogen- and phosphorus-doped materials the active sites were the carbon sites next to P-N bonds in the carbon

structure [85]. From STEM images, it is clear that in the 4Fe4NiNCR material the nanoparticles are covered with graphitic carbon layers, and it is likely that they do not participate in the OER directly. Thus, it is possible that the nanoparticles enhance the activity of the surface carbon and/or heteroatom sites via charge redistribution [151]. It is also possible that the graphitic carbon partially corrodes during the OER process, which would expose the underlying bimetallic nanoparticles. On these nanoparticles, oxide/oxyhydroxide active sites would then form, which have shown high activity for OER [48,151].

The stability of the catalyst materials is important for practical usage in RZABs. In particular, batteries are expected to discharge at a stable voltage for a long duration, making chronoamperometric tests especially relevant. The 4Fe4NiNCR material showed high stability during a 10 h chronoamperometric test, with the current decreasing by only 10% (Figure 23d, inset). During the short-term stability test, however, the $E_{1/2}$ decreased by 30 mV, which indicates moderate stability (Figure 23d). XPS analysis of the 4Fe4NiNCR material after the stability test showed that the surface oxygen content had doubled from 6.7 at% to 12.6 at%. Additionally, the deconvoluted O1s XPS spectra indicated that the main oxygen-containing species are carbonyl (C=O) groups, while before stability tests the oxygen was present as various carbon-oxygen functional groups. These results suggest that the surface carbon structure had partially corroded, possibly due to the effects of HO_2^-, which could contribute to a decrease in electrocatalytic ORR activity of the 4Fe4NiNCR catalyst [48].

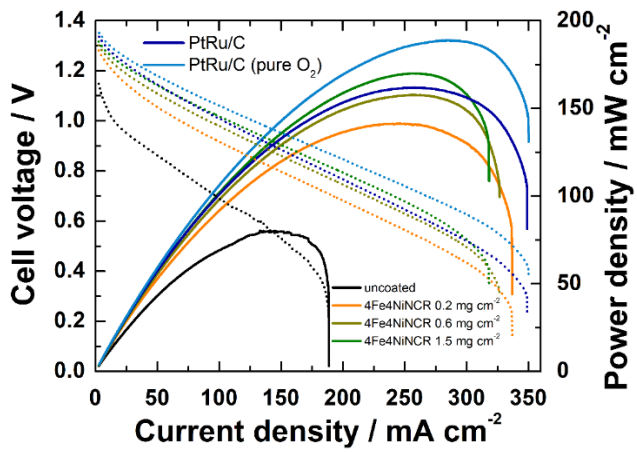

Figure 24. RZAB discharge polarization and power density curves using 4Fe4NiNCR air electrode of various loadings. Battery 1.

The 4Fe4NiNCR material showed the lowest ΔE value and therefore was used as an air electrode catalyst for RZABs. Additionally, the effect of battery parameters on the RZAB performance was investigated by using two different battery configurations denoted as Battery 1 and Battery 2 (Section 5.3.3). Battery 2 had a larger zinc electrode to air electrode area ratio (6.25:1 *vs* 3.22:1) and a larger

electrolyte volume to zinc mass ratio (7.84 mL g_{Zn}^{-1} *vs* 5.46 mL g_{Zn}^{-1}) compared to Battery 1. The P_{max} of RZAB has been shown to depend on the ratio of zinc electrode area to air electrode area, with the optimal ratio around 6:1–8:1 [104]. When the RZAB was operated using only a GDL without any catalyst layer, a P_{max} of 82 mW cm^{-2} was observed for both battery configurations (Figures 24 and 25, Table 12). The GDL consists of a macroporous hydrophobic layer covered with a microporous carbon layer. Porous carbon is known to have inherent ORR activity but is unstable during OER [41,152,153]. Interestingly, this P_{max} value of the uncoated GDL is already comparable to the values reported for RZABs using different catalyst materials [152,153]. Using the 4Fe4NiNCR catalyst at a low loading of 0.2 mg cm^{-2} as an air electrode catalyst in Battery 1, the P_{max} increased to 141 mW cm^{-2}, indicating enhanced performance (Figure 24). Increasing the air electrode catalyst loading to 0.6 mg cm^{-2} and 1.5 mg cm^{-2} further raised the P_{max} value to 157 and 170 mW cm^{-2}. Additionally, it was observed that increasing the catalyst loading slightly reduced the maximum current density, likely due to thicker catalyst layers impeding oxygen mass transfer (Figure 24).

Table 12. RZAB discharge polarization and power density measurement data. Battery 2.

Catalyst	Loading, mg cm^{-2}	P_{max}, mW cm^{-2}
Uncoated	-	82
Uncoated (pure O_2)	-	157
4Fe4NiNCR	1.5	202
4Fe4NiNCR (pure O_2)	1.5	256
50:25:25 PtRu/C	1	205
50:25:25 PtRu/C (pure O_2)	1	316

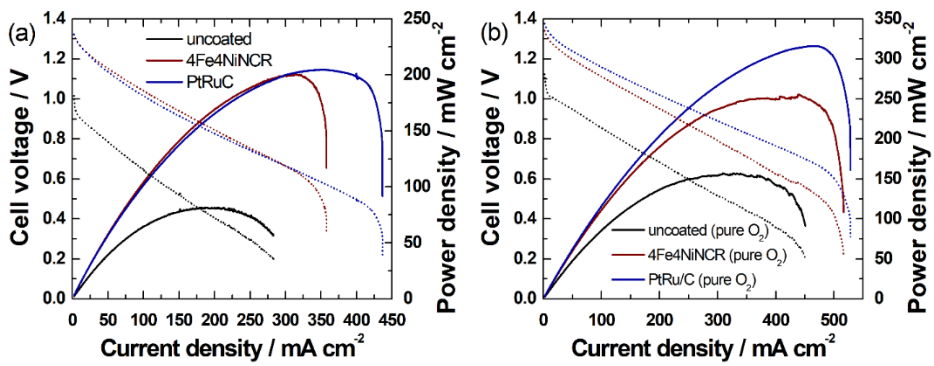

Figure 25. RZAB discharge polarization and power density curves using uncoated GDL or 4Fe4NiNCR and 50:25:25 PtRu/C catalysts (a) in air and (b) in pure O_2. Current rate 10 mA min^{-1}, Battery 2.

When the 4Fe4NiNCR material was used as an air electrode catalyst for Battery 2 with the optimized loading, a high P_{max} of 202 mW cm^{-2} was observed (Figure 25a, Table 12). This result was remarkably close to the performance of the commercial 50:25:25 PtRu/C, which had a P_{max} of 205 mW cm^{-2}. However, the maximum current density for the 4Fe4NiNCR material was lower, 350 mA cm^{-2} compared to 430 mA cm^{-2} for 50:25:25 PtRu/C. With Battery 1, 50:25:25 PtRu/C appears to perform worse with a P_{max} of 162 mW cm^{-2}, compared to a P_{max} of 170 mW cm^{-2} using 4Fe4NiNCR. However, the maximum current densities for Battery 1 are similar for both materials. This indicates that there is a limiting factor affecting the performance of Battery 1, which is not observed for Battery 2. This may be related to limited oxygen diffusion to the air electrode or to issues with the zinc electrode. To investigate this further, the RZAB polarization curves were measured in a pure O_2 atmosphere. Using Battery 1, the P_{max} for 50:25:25 PtRu/C increased from 162 mW cm^{-2} to 189 mW cm^{-2}, but the maximum current density stayed the same (Figure 24). As Battery 2 had a higher performance of 205 mW cm^{-2} using oxygen from air, this suggests that the higher zinc electrode to air electrode ratio was responsible for increased performance compared to Battery 1. This was further confirmed by the results using pure O_2 for Battery 2, where 4Fe4NiNCR had a 27% higher P_{max} of 256 mW cm^{-2}, while the P_{max} for 50:25:25 PtRu/C increased by 54% to 316 mW cm^{-2} (Figure 25b, Table 12). Thus, the RZAB performance of the catalysts was limited by oxygen diffusion for Battery 2. However, it was observed that the maximum current densities for both catalysts were similar at 510–515 mA cm^{-2}, again suggesting a limitation within the battery system. As the maximum current densities were similar, it is likely that the limitation was not due to oxygen transport in the catalyst layer, because the maximum current density would likely be different for 50:25:25 PtRu/C and 4Fe4NiNCR, as observed in measurements in air. It is possible that the oxygen transport through the GDL was the limiting factor, but this is unlikely due to the GDLs high air permeability of 1.5 Gurley sec, as given by the manufacturer. The air permeability value corresponds to 10.3 cm s^{-1}, which at the limiting current density of 510 mA cm^{-2} corresponds to a required oxygen transport of 0.06 cm s^{-1}. The significant difference between the required oxygen flux and the given air permeability indicates that the GDL is not the limiting factor, despite the fact that the permeability of the GDL is measured under a certain small pressure difference [154]. Therefore, the limitation is most likely associated with the zinc electrode, as zinc electrodes are known to passivate more rapidly at higher current densities [46]. This appears to limit the peak power density of RZAB, regardless of the activity of the air electrode catalyst.

The discharge performance of both Battery 1 and Battery 2 was investigated by fully discharging the RZABs at 20 mA cm^{-2} (Figure 26). Using Battery 2 and the 4Fe4NiNCR catalyst for the air electrode, a high average discharge voltage of 1.18 V and an excellent specific capacity of 616 mAh g_{Zn}^{-1} were observed, resulting in a high specific energy of 727 mWh g_{Zn}^{-1}. For 50:25:25 PtRu/C, these values were lower, with an average discharge voltage of 1.15 V, a specific capacity of 597 mAh g_{Zn}^{-1}, and a specific energy of 685 mWh g_{Zn}^{-1}, indicating that

4Fe4NiNCR exhibited superior discharge performance. Using Battery 1 and the 4Fe4NiNCR catalyst for the air electrode, the results were much lower, at a specific capacity of 448 mAh g_{Zn}^{-1} and a specific energy of 510 mWh g_{Zn}^{-1}. This suggests that similar to the P_{max} measurements, certain parameters of Battery 1 were limiting the discharge performance. For both Battery 1 and Battery 2, and for both catalysts, the calculated concentration of zincate anions at the end of the measurement was around 1.4–1.5 M. This indicates that the limiting parameter for Battery 1 was the electrolyte volume-to-zinc mass ratio, which was larger for Battery 2. Increasing the volume of electrolyte solution in the battery to avoid the passivation of the zinc electrode by zinc oxide precipitation could increase the utilization of zinc, but this would decrease the battery-level energy density by considerably increasing the weight of the battery. Another possibility is improving the solubility of zinc oxide or zincate by adjusting the composition of the electrolyte [155,156].

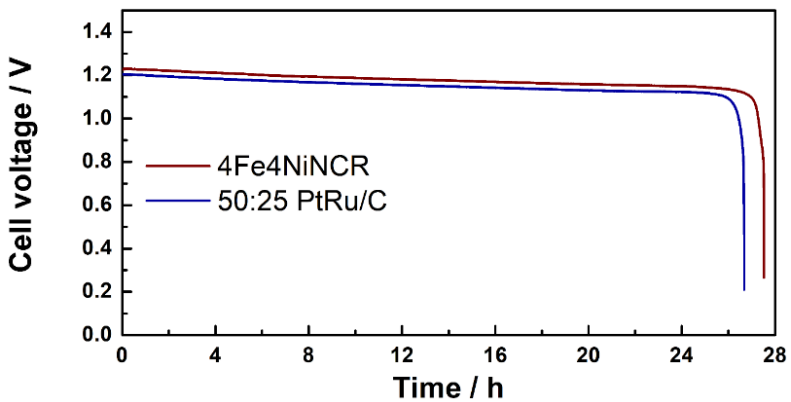

Figure 26. RZAB discharge curves of Battery 2 at 20 mA cm^{-2} using 4Fe4NiNCR and 50:25:25 PtRu/C catalysts.

In order to investigate the recharging performance of RZABs, two different cycling procedures were used. The first procedure used 10-min cycles of discharging and charging at 5 mA cm^{-2} (5 min discharge followed by 5 min charge) [157,158]. Battery 1 using the 4Fe4NiNCR catalyst showed good stability for 146 h (876 cycles) with a low voltage gap of 0.85–0.91 V (58% to 53% charging efficiency) using the first procedure (Figure 27). However, this procedure does not correspond well to practical battery usage, due to the low areal cycling capacity of 0.42 mAh cm^{-2} [42,159]. The second procedure was therefore chosen to achieve higher areal cycling capacities of >10 mAh cm^{-2}, which better simulate realistic usage [42,159]. Thus, 1-hour cycles were used, consisting of discharging at 25 mA cm^{-2} for 30 min, followed by charging at 25 mA cm^{-2} for 30 min, corresponding to an areal cycling capacity of 12.5 mAh cm^{-2}.

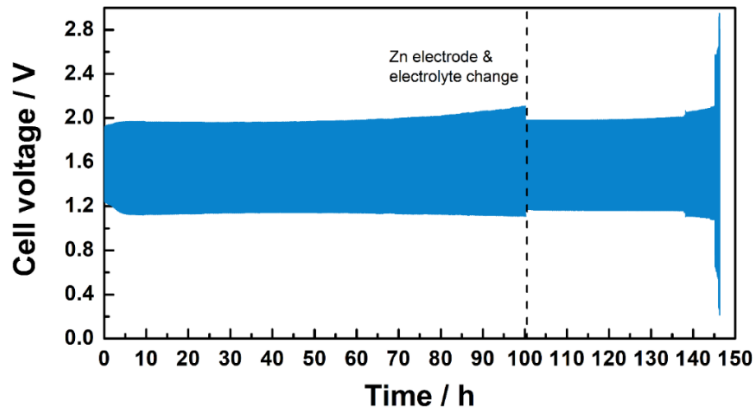

Figure 27. RZAB cycling performance at low areal capacity for the 4Fe4NiNCR material in Battery 1. 10-min cycles of discharging and charging for 5 min at 5 mA cm^{-2} for an areal cycling capacity of 0.42 mAh cm^{-2}. Catalyst loading 1.5 mg cm^{-2}.

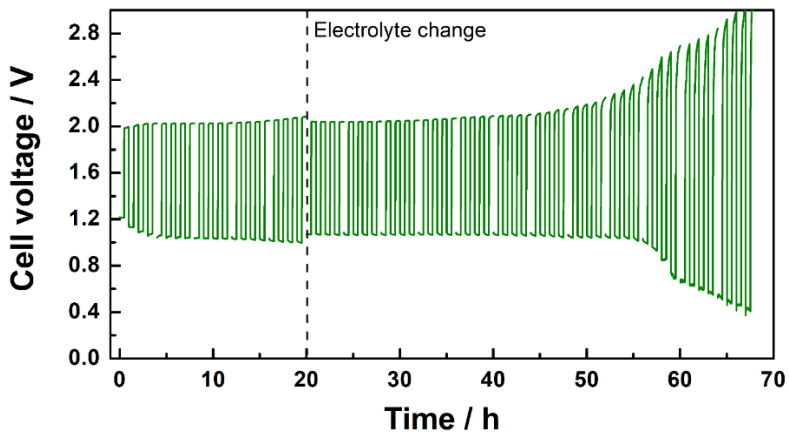

Figure 28. ZAB cycling performance at 12.5 mAh cm^{-2} areal cycling capacity for the 4Fe4NiNCR material. 1-hour cycles of discharging and charging for 30 min at 25 mA cm^{-2}. Catalyst loading 1.5 mg cm^{-2}. Battery 2. [IV]

Using Battery 2, the 4Fe4NiNCR catalyst showed excellent results for the second cycling procedure, staying stable for 68 h (68 cycles) (Figure 28). It became evident that the charging process changed the surface structure of the catalyst, as the initial voltage gap of 0.79 V (61% charging efficiency) increased to 0.97 V (52% charging efficiency) during the initial cycles. After refreshing the electrolyte at around 20 h due to electrolyte leakage, the voltage gap returned to 0.97 V (52% charging efficiency), which indicates that the catalyst was stable. Comparable results were obtained using Battery 1, although it lasted for only around 30 h (28 cycles) due to issues with electrolyte leakage. Increased O_2 bubble formation at higher current densities was the most probable cause of leakage issues

for both batteries. The overpotential and other issues caused by the formation of O_2 bubbles during charging are well-known challenges for RZABs [50,51,160]. Modifying the air electrode to improve oxygen transport could help mitigate these issues, for example by using hierarchical hydrophilic and hydrophobic layers on the air electrode [50,52]. Using the second cycling procedure with the 50:25:25 PtRu/C catalyst showed that the catalyst was highly unstable during charging, lasting for only 5 h (5 cycles) (Figure 29). By the end of the first charging cycle, the initial voltage gap of 0.92 V had increased to 1.12 V (56% - 51% charging efficiency), as the charging voltage rose from 2.11 to 2.30 V. Similar performance for PtRu/C catalysts has been reported in the literature, and the low stability of PGM-based catalysts during RZAB cycling is well-known [161–163]. The results obtained with the 4Fe4NiNCR catalyst indicate that it is suitable for practical applications in RZABs, as it combines P_{max} values above 200 mW cm^{-2} with high stability at practically relevant areal cycling capacities.

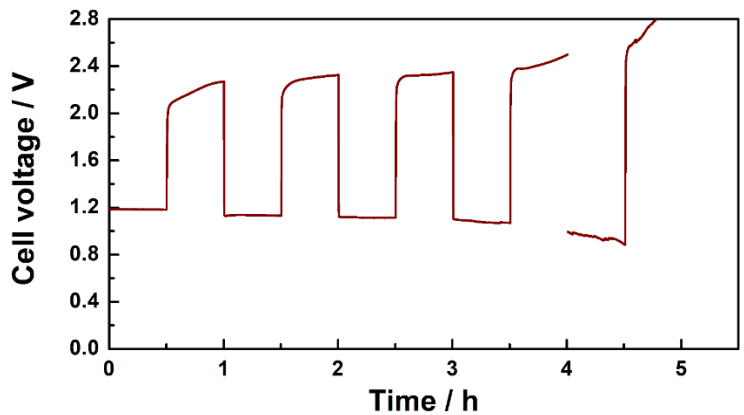

Figure 29. ZAB cycling performance at a high areal cycling capacity for the benchmark catalyst 50:25:25 PtRu/C in Battery 2. 1-hour cycles of discharging and charging for 30 min at 25 mA cm^{-2} for an areal cycling capacity of 12.5 mAh cm^{-2}. Catalyst loading 1 mg cm^{-2}.

6.2.4. Ionothermally synthesized electrocatalysts for RZAB

The previous results showed that pyrolysis using an Mg-based template was well suited for producing both active ORR catalysts and bifunctional catalysts for ORR and OER [III, IV]. However, both the porous carbon structure and active sites are formed simultaneously during pyrolysis, which may be limiting for high electrocatalytic activity. It is possible to separate the formation of the porous carbon structure from the formation of active sites for ORR/OER, which may be beneficial for optimizing the performance of materials in RZABs or AEMFCs [164,165]. Thus, we synthesized mesoporous electrocatalyst materials using an ionothermal method with rapeseed press cake as a carbon source (Section 5.1.3,

Table 6) [V]. Magnesium nitrate hexahydrate has a melting point of around 89 °C, which means that it forms a liquid reaction medium during the pyrolysis procedure [165]. At around 350–400 °C, magnesium nitrate starts to decompose into nitrogen dioxide (NO_2) gas and magnesium oxide nanoparticles, with NO_2 further reacting with the carbonizing material and introducing nitrogen and micropores into the material [164–166]. Similar to the previous synthesis process [III, IV], the magnesium oxide nanoparticles are washed out with an acid-treatment procedure, which leaves behind a mesoporous structure in the carbon material. The active sites are then formed during the second synthesis step, where the carbon base material is doped with transition metal complexes of 1,10-phenanthroline, following a previously reported method [82,83,128,164].

The 05Fe05NiPhenIC material prepared in this way shows an interconnected foam-like carbon structure (Figure 30a-g). Evenly dispersed carbon, nitrogen, and oxygen are seen from STEM-EDX elemental mapping, along with transition metal-containing nanoparticles (Figure 30g-m). The structure of this material is distinct from the previously described materials [I-IV]. Additionally, the nanoparticles do not seem to be surrounded by a graphitic carbon shell, likely due to the fact that the carbon material was synthesized separately. A relatively high nickel and iron content and a pyrolysis temperature of 800 °C were used in the catalyst synthesis in order to induce the formation of nanoparticles, which was clearly confirmed. Metal nanoparticles are known to be generally active for OER [48]. In contrast, only atomically dispersed metal sites were observed using the same doping method at 600 °C [82]. Additionally, in an alkaline environment, metal nanoparticles can favorably modulate the electronic properties of nearby active sites, thereby enhancing the ORR activity [48,134,167]. Atomically sized bright spots are visible in high-resolution HAADF-STEM image, indicating that iron and nickel are also atomically dispersed throughout the carbon structure. These are likely in the form of M-N_x centers, a high density of which is known to improve the ORR performance of electrocatalysts [6].

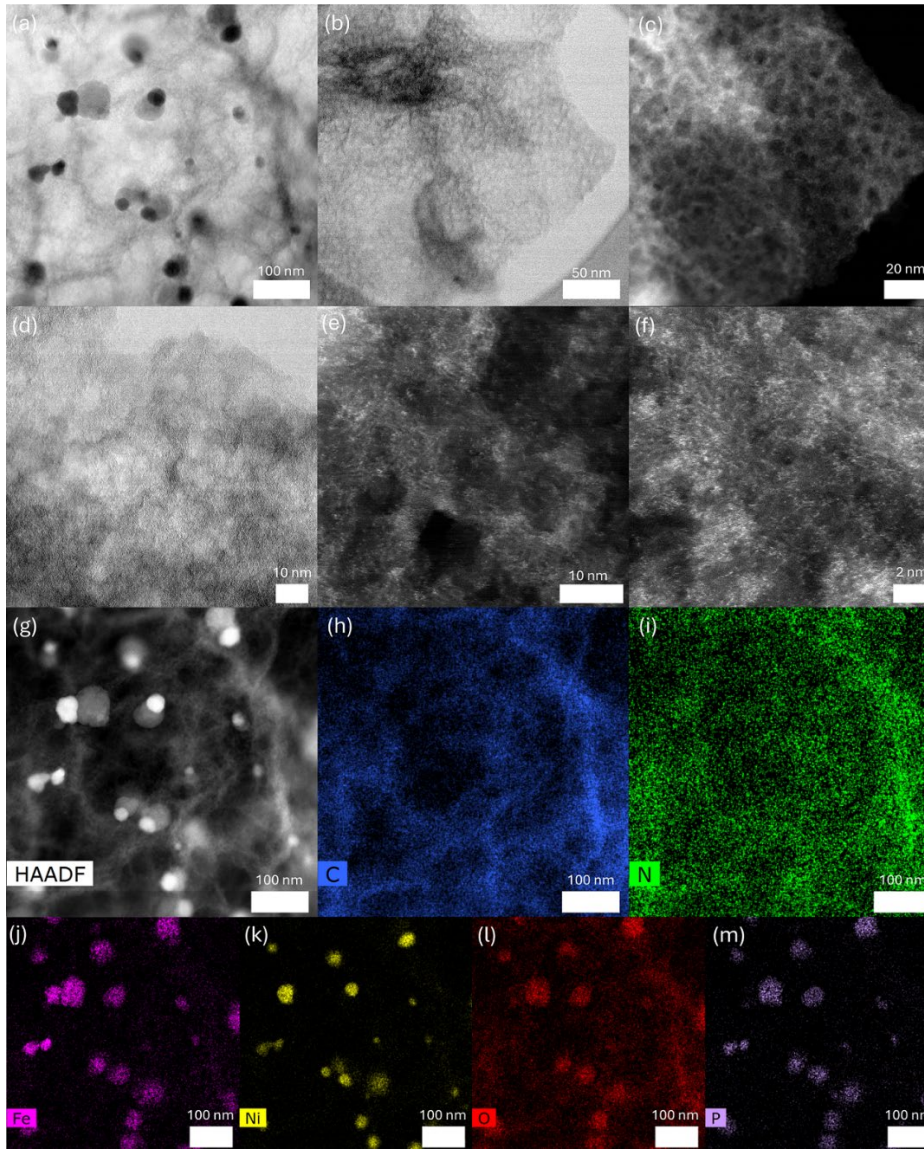

Figure 30. (a, b, and d) bright-field STEM images, (c, e-g) HAADF STEM images and (h-m) elemental mappings of carbon, nitrogen, iron, nickel, oxygen, and phosphorus for 05Fe05NiPhenIC material.

SEM-EDX analysis shows that the synthesized catalyst materials contain around 5–6 wt% nickel and iron along with 70–73 wt% carbon, 7–9 wt% nitrogen, and around 1 wt% phosphorus. In the material FeNiPhenIC with doubled metal content in the precursor mixture, the nickel and iron content is around 8 wt%. Additionally, the mass ratios of iron and nickel correspond well to the ratios of metals in the precursors. The materials also contain around 1–2 wt% of magnesium,

which is most likely in the form of Mg-N_x centers, which do not dissolve during acid treatment [138]. Magnesium oxide was successfully removed from the ionothermally synthesized carbon base material during the acid treatment, as shown by XRD analysis (Figure 31). However, according to the XRD analysis, all of the catalyst materials contain MgO, along with iron-nickel-magnesium oxide and iron(II,III) oxide for some materials (Figure 32c), which indicates that MgO reformed from Mg-N_x sites during the second pyrolysis step. Additionally, all of the catalyst materials contain iron-nickel alloys ($Fe_{0.5}Ni_{0.5}$, $Fe_{0.6}Ni_{0.4}$, and $Fe_{0.8}Ni_{0.2}$, with reflections at 43–44°, 51°, 73–75°, and 91–92° (2θ)), along with various metal phosphides (Fe_3P, $Fe_{1.5}Ni_{1.5}P$, and $Fe_{1.92}Ni_{1.08}P$) (Figure 32c). All of the transition-metal-containing nanoparticles are likely active for OER, as under anodic potentials they are restructured to the corresponding (oxy)hydroxides, which are known to exhibit high OER activity [48].

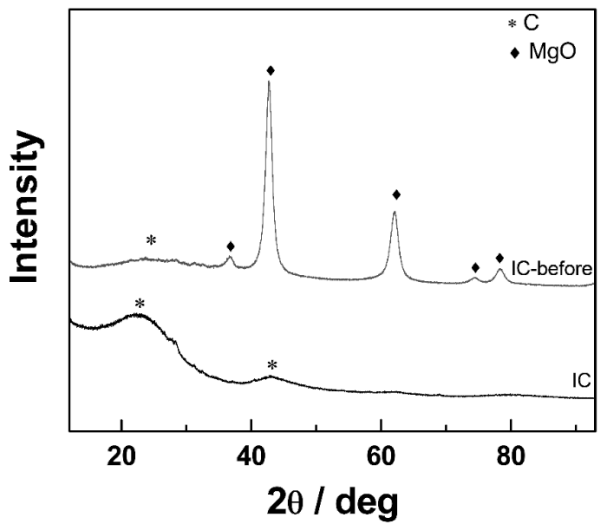

Figure 31. XRD patterns of the ionothermally synthesized carbon before and after acid treatment.

The surface elemental composition of the ionothermal carbon IC and the 095Fe005NiPhenIC, 05Fe05NiPhenIC, and FeNiPhenIC materials as determined by XPS, was consistent with SEM-EDX results. The surface of the catalyst materials contained mainly carbon, nitrogen, and oxygen, along with phosphorus, magnesium, iron, and nickel. A deconvoluted N1s XPS spectrum is shown in Figure 32d. Pyridinic and pyrrolic nitrogen both account for around 36–45% of the nitrogen content. The base carbon material IC has a high relative surface content of M-N_x centers (6.8%), which, as indicated by XRD data in Figure 31, are likely in the form of Mg-N_x centers. While M-N_x centers are known to be the main active sites for ORR, Mg-N_x centers are generally considered to have negligible activity for ORR [164,168]. The material with doubled metal content

(FeNiPhenIC) has the highest relative surface content of M-N_x centers (15.1%), while the corresponding values are 0.4% for 095Fe005NiPhenIC and 2.1% for 05Fe05NiPhenIC.

For Raman analysis, the spectra were normalized to the intensity of the G band, after which they were deconvoluted according to the five Voigt-shaped band model to D4 (1195 cm^{-1}), D1 (1355 cm^{-1}), D3 (1505 cm^{-1}), G (1590 cm^{-1}), and D2 (1615 cm^{-1}) bands [112]. The catalyst materials have a typical defective carbon structure, as indicated by broad D1 and G bands (Figure 32b) [112]. Similar to the Raman spectroscopy analysis employed in article [IV], for highly disordered materials it is more appropriate to compare $I_{D1}/(I_G + I_{D2})$ ratios instead of I_{D1}/I_G ratios due to the overlap of the G band with the D2 band [147]. The calculated $I_{D1}/(I_G + I_{D2})$ ratios are 2.1, 1.6, 1.9, and 1.8 for 095Fe005NiPhenIC, 05Fe05NiPhenIC, FeNiPhenIC, and IC materials, respectively. While graphitic carbon is generally more stable and a better conductor of electricity, defects in the carbon structure may function as active sites for ORR [70]. Transition metals are known to catalyze the graphitization of carbon, and increasing the metal content in the precursor mixture can enhance the degree of graphitization of the resulting carbon-based material [146,169], which was also seen with previous materials [IV]. The differences between the materials are small, likely due to the separate synthesis of the carbon base material. According to N_2 physisorption analysis, the carbon base material IC has a relatively high SSA of 606 $m^2\ g^{-1}$, which decreases with increasing metal content (Figure 32a, Table 13). The PSD for IC, 05Fe05NiPhenIC, and FeNiPhenIC is similar, although the peaks are lower for doped materials. This implies that the existing pores are partially occupied by metal species introduced during the second synthesis step. A prominent peak at around 5 nm in diameter is seen for all analyzed materials in the PSD graph, along with a smaller peak at 3–4.5 nm; all materials also contain mesopores in the 6–15 nm range (Figure 32a). The peak at around 3–4 nm may originate from the rapeseed press cake biomass, since when the same ionothermal synthesis method was used with cyclodextrin as the carbon source, only a single prominent peak at around 5 nm was seen [165]. Similar peaks in the PSD graphs were observed in our previous work, where template precursors were not used in the synthesis procedure [II].

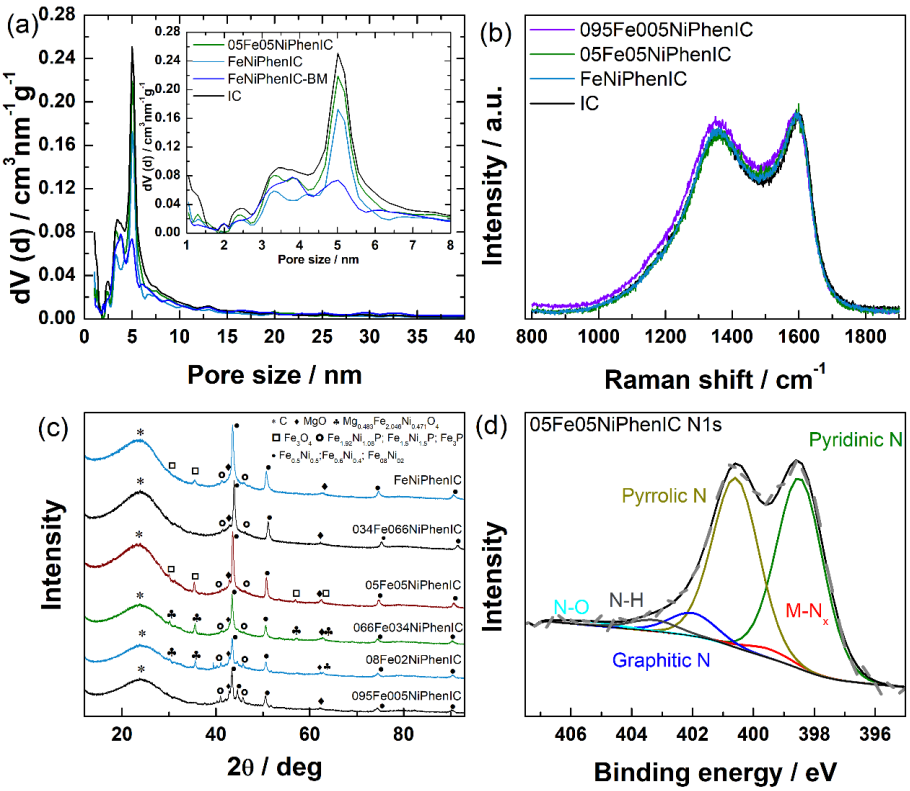

Figure 32. (a) PSD curves of IC, 05Fe05NiPhenIC, FeNiPhenIC and FeNiPhenIC-BM catalyst materials. Inset: magnified section of the pore-size distribution. (b) Raman spectra of IC, 095Fe005NiPhenIC, 05Fe05NiPhenIC, and FeNiPhenIC materials. (c) XRD patterns of various catalyst materials. (d) Deconvoluted XPS N1s spectra for 05Fe05NiPhenIC material.

Table 13. S_{BET}, S_{dft}, V_{tot} and V_{micro} of electrocatalyst materials determined via N_2 physisorption analysis.

Material	S_{BET} ($m^2\ g^{-1}$)	S_{dft} ($m^2\ g^{-1}$)	V_{tot} ($cm^3\ g^{-1}$)	V_{micro} ($cm^3\ g^{-1}$)
IC	605	556	0.66	0.17
05Fe05NiPhenIC	512	489	0.59	0.14
FeNiPhenIC	422	412	0.47	0.12
FeNiPhenIC-BM	411	417	0.51	0.13

The electrocatalytic activity of the synthesized materials toward the ORR and OER was studied by RDE in 0.1 M KOH solution (Figure 33, Table 14). The base carbon material IC was somewhat active for ORR with an $E_{1/2}$ value of 0.76 V,

although this was significantly lower compared to the transition metal-containing catalysts. While XPS analysis indicated a high relative content of Mg-N_x centers for IC, the ORR activity of Mg-N_x centers is generally low and depends strongly on the coordinating environment of the Mg site [168,170]. Additionally, after magnesium ions were exchanged for iron ions using an ion-exchange method, the ORR activity was considerably increased for certain electrocatalyst materials [164]. It is likely that the ORR activity of IC is due to nitrogen and/or phosphorus moieties, which are active for ORR in an alkaline environment. The ORR activity of the transition metal-containing catalyst materials is high, surpassing that of 20 wt% Pt/C for most materials. The MA values increase from 2.4 to 16.3 A g^{-1} with increasing relative iron content (see Table 14), which is most likely related to the increasing number of Fe-N_x centers, as Ni-N_x centers have low activity for ORR [113,171]. The double-layer capacitance (C_{dl}) of all the materials is around 4–5 mF cm^{-2}, which indicates only minor differences in the electrochemically accessible surface area of the catalysts. The OER performance of the catalysts is very similar, with the $E_{j=10}$ values of 1.63–1.64 V for all materials, except 095Fe005NiPhenIC, which shows a value of 1.67 V (Figure 33b, Table 14). While XRD data indicated that the materials contained different transition-metal-containing nanoparticles, it is likely that their surface was restructured to the corresponding (oxy)hydroxides at anodic potentials, which probably causes their similar OER activity [48]. The lower relative Ni content of 095Fe005NiPhenIC is likely responsible for the reduced OER performance. The n values range between 3.7–4.0 for all the transition-metal-containing catalyst materials, according to the K-L analysis (Table 14). This indicates that while the main ORR pathway is $4e^-$ reduction, around 10–15% HO_2^- is still produced via $2e^-$ pathway, which may be detrimental to RZAB cell components, such as the air electrode.

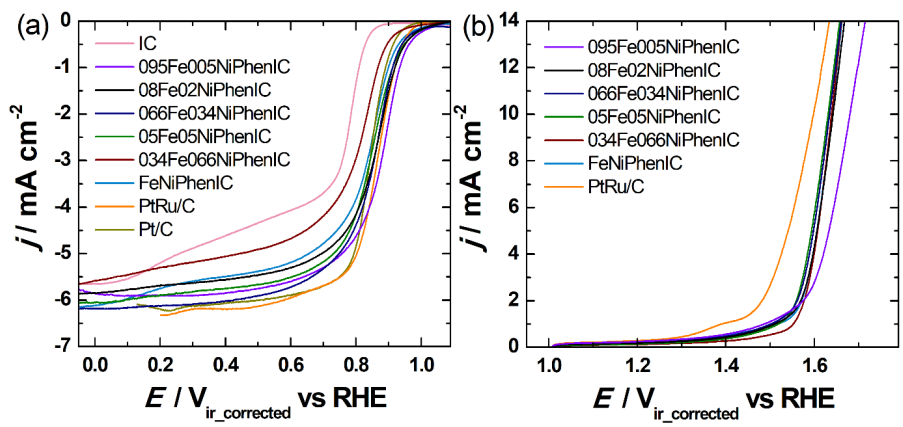

Figure 33. (a) ORR and (b) OER polarization curves for various catalyst materials in O_2-saturated 0.1 M KOH. ω = 1900 rpm, ν = 10 mV s^{-1}.

Table 14. ORR and OER parameters of different catalyst materials in 0.1 M KOH, ω =1900 rpm.

Catalyst	E_{onset}, V	$E_{1/2}$, V	$E_{j=10}$, V	ΔE, V	n	MA at 0.9 V, A g^{-1}
IC	0.86	0.76	-	-	3.2–3.3	n.d
095Fe005NiPhenIC	0.99	0.88	1.67	0.79	3.9–4.0	16.3
08Fe02NiPhenIC	0.98	0.86	1.64	0.78	3.8–3.9	9.8
066Fe034NiPhenIC	0.98	0.86	1.63	0.77	3.7–3.8	8.5
05Fe05NiPhenIC	0.98	0.84	1.63	0.79	3.8–3.9	7.7
034Fe66NiPhenIC	0.95	0.81	1.63	0.82	3.9–4.0	2.4
FeNiPhenIC	0.97	0.83	1.63	0.80	3.8–3.9	6.1
20 wt% Pt/C	0.97	0.84	-	-	3.9–4	4.3
50:25:25 PtRu/C	0.99	0.86	1.60	0.74	3.9–4	10.4

The stability of the catalyst materials is critical for practical application in RZABs. While the 05Fe05NiPhenIC material was stable during a 10 h chrono-amperometric test, with the current decaying by only 11%, the short-term stability test showed moderate stability, with $E_{1/2}$ decreasing by 80 mV (Figure 34a-b). The same tests were performed using a commercial 50:25:25 PtRu/C catalyst, where the current decay was 8%, while the $E_{1/2}$ decreased by 35 mV (Figure 34c–d). One possible cause for the loss in ORR activity for the 05Fe05NiPhenIC material during the short-term stability test is the dissolution of metals from both nanoparticles and M-N_x sites [172]. Additionally, carbon corrosion due to HO_2^- produced during ORR is also a possibility, as observed previously by XPS analysis conducted after stability testing [IV].

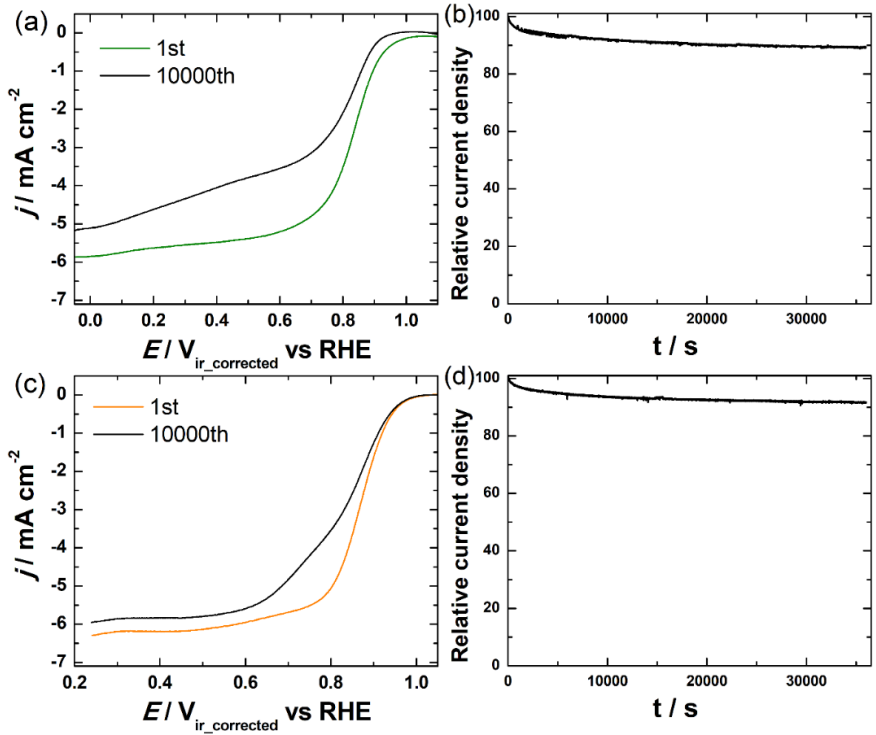

Figure 34. (a) ORR polarization curves for 05Fe05PhenIC before and after 10000 potential cycles between 1 and 0.4 V. ω = 1900 rpm, ν = 10 mV s^{-1}. (b) CA stability test of 05Fe05PhenIC at 0.5 V, ω = 960 rpm. (c) ORR polarization curves for 50:25:25 PtRu/C before and after 10000 potential cycles between 1 and 0.4 V. ω = 1900 rpm, ν = 10 mV s^{-1}. (d) CA stability test of 50:25:25 PtRu/C at 0.5 V, ω = 960 rpm.

The transition-metal-containing materials were investigated in RZABs, as they all had high bifunctional activity. The optimal loading for air electrodes appeared to be around 0.4–0.5 mg cm^{-2} (Figure 35a). Additionally, experiments with an anion-exchange ionomer (AEI) in the catalyst layer were conducted. As noted by Li and co-workers, almost all reports of RZABs use Nafion [173], which is a cation-exchange ionomer and thus presumably functions only as a binder in the catalyst layer. As they further note, it is reasonable to evaluate AEIs in the catalyst layers due to their anion-exchange properties [173]. It was revealed that there are only minor differences in the RZAB discharge polarization curves obtained using different ionomers, although the batteries using Nafion in the catalyst layers perform slightly better (Figure 35). This is likely because the ion-exchange properties of the binders in the catalyst layer are not as relevant in RZAB as compared to AEMFCs, due to the much higher ionic conductivity of the 6 M KOH electrolyte. A similar result was reported for anion-exchange membrane water electrolyzers, where Nafion showed slightly better performance [174].

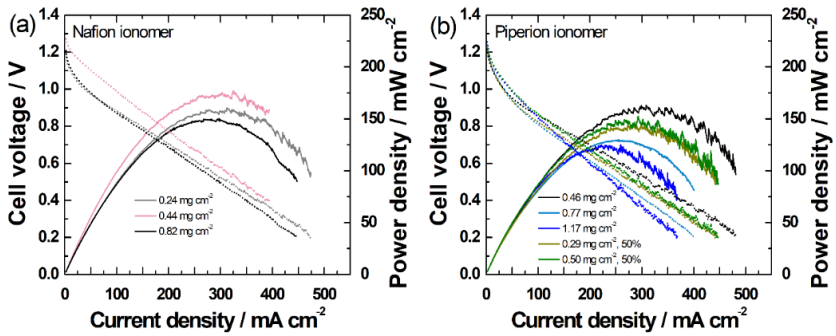

Figure 35. RZAB discharge polarization and power density curves of FeNiPhenIC using different catalyst loadings with (a) Nafion or (b) Piperion ionomer. 20 wt% ionomer is used, unless shown otherwise in the graph. Current rate 10 mA min^{-1}.

The discharge polarization curves of various catalyst materials with the optimized loading are shown in Figure 36a. The 034Fe066NiPhenIC material has the lowest P_{max} of 158 mW cm^{-2}, while the other catalysts have P_{max} values between 168–180 mW cm^{-2} and the commercial 50:25:25 PtRu/C catalyst reaches 199 mW cm^{-2} (Table 15). The synthesized catalysts had a highly porous, low-density structure characteristic of materials with a high SSA, which is why a ball-milling procedure was also applied to the FeNiPhenIC and 05Fe05NiPhenIC catalysts in order to reduce their bulk volume and thereby decrease the thickness of the catalyst layer on the GDL. It has been shown that the structure and thickness of the catalyst layer have a large effect on the performance of catalysts in fuel cells [175,176]. The RZAB results were improved using ball-milled catalysts, as the P_{max} of 05Fe05NiPhenIC-BM increased by 8% from 178 to 192 mW cm^{-2}, and the P_{max} of FeNiPhenIC-BM increased by 15% from 179 to 205 mW cm^{-2} (Figure 36b, Table 15). Additionally, the PSD for FeNiPhenIC-BM changed, with the peak at around 5 nm becoming less pronounced (Figure 32a). Both the change in catalyst structure on the GDL and the modified PSD could be responsible for the increased RZAB performance.

Table 15. RZAB discharge polarization and power density measurement data.

Catalyst	Catalyst loading, mg cm^{-2}	P_{max}, mW cm^{-2}
095Fe005NiPhenIC	0.42	174
08Fe02NiPhenIC	0.42	167
066Fe034NiPhenIC	0.45	181
05Fe05NiPhenIC	0.45	178
034Fe066NiPhenIC	0.47	158
FeNiPhenIC	0.44	179
50:25:25 PtRu/C	0.40	199

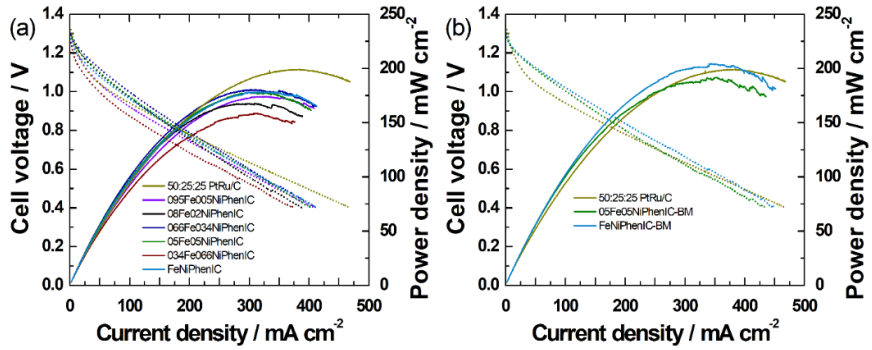

Figure 36. RZAB discharge polarization and power density curves of (a) pristine and (b) ball-milled catalyst materials, and of 50:25:25 PtRu/C. Current rate 10 mA min^{-1}, catalyst loading 0.45±0.03 mg cm^{-2}, with a loading of 0.4 mg cm^{-2} for 50:25:25 PtRu/C.

For the RZAB full discharge experiments at 20 mA cm^{-2}, a good average discharge voltage of 1.11 V and a battery capacity of 464 mAh were obtained using the 05Fe05NiPhenIC material, which corresponds to a specific capacity of 520 mAh g_{Zn}^{-1} and a specific energy of 579 mWh g_{Zn}^{-1}. To investigate the charging performance of RZABs, the catalyst materials were evaluated using 2 h cycles, by discharging for 1 h and charging for 1 h at 10 mA cm^{-2}, corresponding to an areal capacity of 10 mAh cm^{-2} (Figure 37a). The current density of 10 mA cm^{-2} was chosen to avoid issues with O_2 bubbles during charging, which were previously observed to be significant when a current density of 25 mA cm^{-2} was used [IV]. The first charging cycle likely changed the properties of all the catalysts, as the discharge voltage in the second cycle decreased by around 0.10–0.12 V for the catalyst materials. This implies that, similar to previous work [IV], an anodic process took place during charging, which reduced the ORR activity. The 034Fe066NiPhenIC material is an exception, as it exhibited a higher charging voltage that continued to increase during successive cycles. In comparison, a commercial 50:25:25 PtRu/C catalyst showed a high initial charging efficiency of 62%, which decreased to 50% by the fifth cycle. Similar RZAB cycling performance, showing low stability of PtRu/C, has been reported in the literature [177,178]. The same cycling conditions were used for a long-term stability test using the 05Fe05NiPhenIC material, which showed good stability for 65 h (33 cycles) (Figure 37b). The electrolyte was changed at 18 h due to leakage, restoring the discharge voltage to its initial value, while the charging voltage increased to 2.2 V. The discharge voltage stayed stable, while the charging voltage decreased to 2.05 V over the next 15 h. The cause of this behavior is unclear, although it is likely related to disassembly and cleaning of the RZAB during electrolyte refilling. Electrolyte leakage was still a problem, likely due to O_2 bubbles. A change in the structure of the GDL during cycling was also evident – the measured thickness of the GDL coated with the 05Fe05NiPhenIC catalyst was around 200–210 µm after the test, compared to around 350–360 µm before the

test. The thickness of the catalyst layer measured by a micrometer screw gauge before the stability test was around 50–60 µm and as the RZAB performance did not significantly decrease, the catalyst layer likely remained intact. This implies that the structure of the GDL changed and/or the microporous layer corroded during the stability test. Electrochemical corrosion of carbon-based catalyst materials and GDLs is known to be a severe problem in RZABs [179,180]. Using GDLs that are not based on carbon, such as melamine foam or polymer substrates, is a possible solution to this issue [181,182].

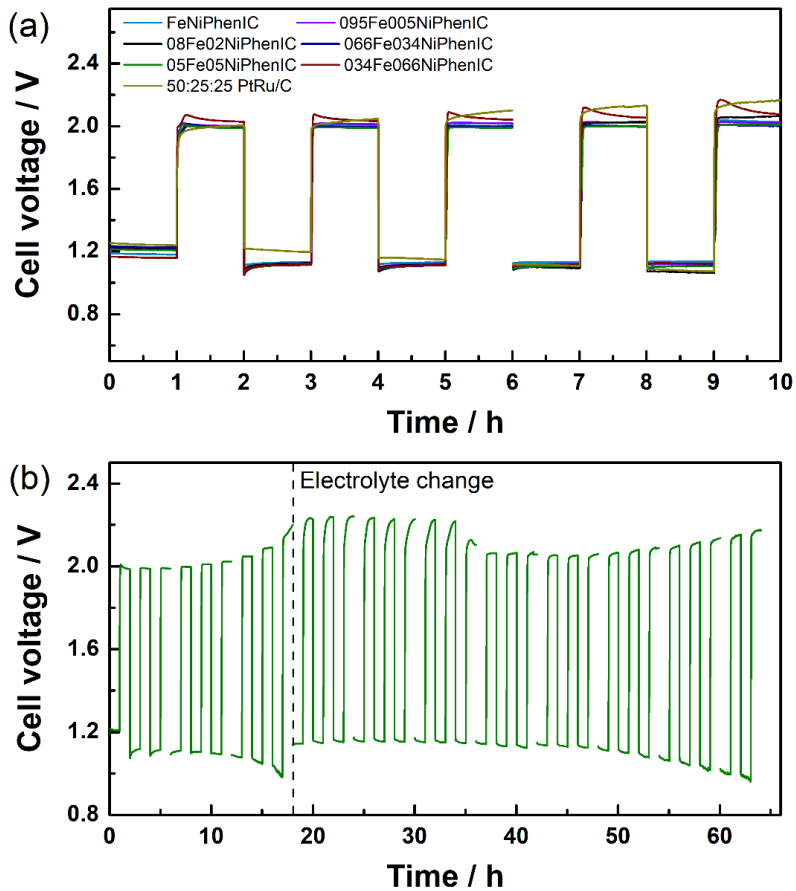

Figure 37. (a) Short-term RZAB cycling performance for various catalyst materials. (b) Long-term RZAB cycling for 05Fe05NiPhenIC material. 2-h cycles of discharging and charging for 1 h at 10 mA cm^{-2} for an areal capacity of 10 mAh cm^{-2}. Catalyst loading 0.45±0.03 mg cm^{-2}.

6.2.5. Ionothermally synthesized electrocatalysts for AEMFC

The ionothermal synthesis method of carbon from rapeseed press cake described in the previous section proved successful for producing highly active bifunctional materials for ORR and OER. Therefore, we decided to use this approach for the synthesis of ORR electrocatalysts for use in AEMFCs. Two carbon materials were ionothermally synthesized from rapeseed press cake (IC and IC2) and doped with nitrogen and transition metals, iron and/or manganese. M-N_x centers are the main active sites for ORR, but transition metals tend to form nanoparticles during pyrolysis at high metal loadings. Thus, a rather low metal loading was used in this part of the work to favor the formation of M-N_x sites. Additionally, all catalysts were ball-milled, as this was found to enhance RZAB performance and was therefore assumed to be beneficial for AEMFC applications as well.

The STEM images for the FeMnIC material show a similar foam-like, interconnected carbon structure as observed in ionothermally prepared materials in previous work (Figure 38a-g) [V]. The material contains well-dispersed carbon, nitrogen, oxygen, phosphorus, iron, and manganese (Figure 38h-m). According to the SEM-EDX analysis, all of the synthesized materials consist of around 70–72 wt% carbon, 10–12 wt% oxygen, 6–7 wt% nitrogen, 1–2 wt% phosphorus, 1–2 wt% magnesium, and 5–6 wt% transition metals. Small bright spots in Figure 38f indicate that iron and manganese are atomically dispersed, likely in the form of M-N_x sites, which are known to have high electrocatalytic activity for ORR. Additionally, some agglomerated bright spots are seen in some STEM images, which may correspond to small nanoparticles, less than 10 nm in diameter (Figure 38c and 38e). The materials exhibit high SSA values according to N_2 physisorption analysis, which are similar to those obtained in previous work (Tables 13 and 16). MnIC appears to have a smaller V_{tot} and a lower SSA compared to the FeIC and FeMnIC materials. Two peaks are seen in the PSD at around 5 nm and 3.5 nm (Figure 39a). The PSD of FeIC, MnIC and FeMnIC materials are rather similar, resembling that of the ball-milled material FeNiPhenIC from previous work [V]. For the MnIC material, the peak at around 5 nm is lower than for FeIC and FeMnIC; however, the overall distribution of pores remains similar, suggesting that these pores are more extensively blocked in MnIC than in the other materials.

XRD analysis shows that the materials FeIC, MnIC, and FeMnIC contain small amounts of magnesium oxide and zirconium oxide (Figure 39b). Zirconium oxide originates from the ball-milling procedure, but it has been shown to have low ORR activity [111]. However, it is possible that zirconium oxide particles partially block pores, which may reduce the ORR activity of the catalysts. Additionally, the FeIC material appears to contain iron phosphide and iron(II, III) oxide phases. The deconvoluted XPS N1s spectrum for the FeMnIC material is shown in Figure 39c. According to XPS analysis, the FeMnIC material contains around 81 at% carbon, 6 at% nitrogen, 10 at% oxygen, and 0.3 at% of both iron and manganese on the surface. Similarly, FeIC and MnIC catalysts have surface nitrogen contents of around 5–6 at% and metal contents of around 0.4–0.6 at%.

The FeMnIC material has around 5% of the surface nitrogen in the form of M-N_x centers, along with approximately equal fractions (32–33%) of pyridinic and pyrrolic nitrogen.

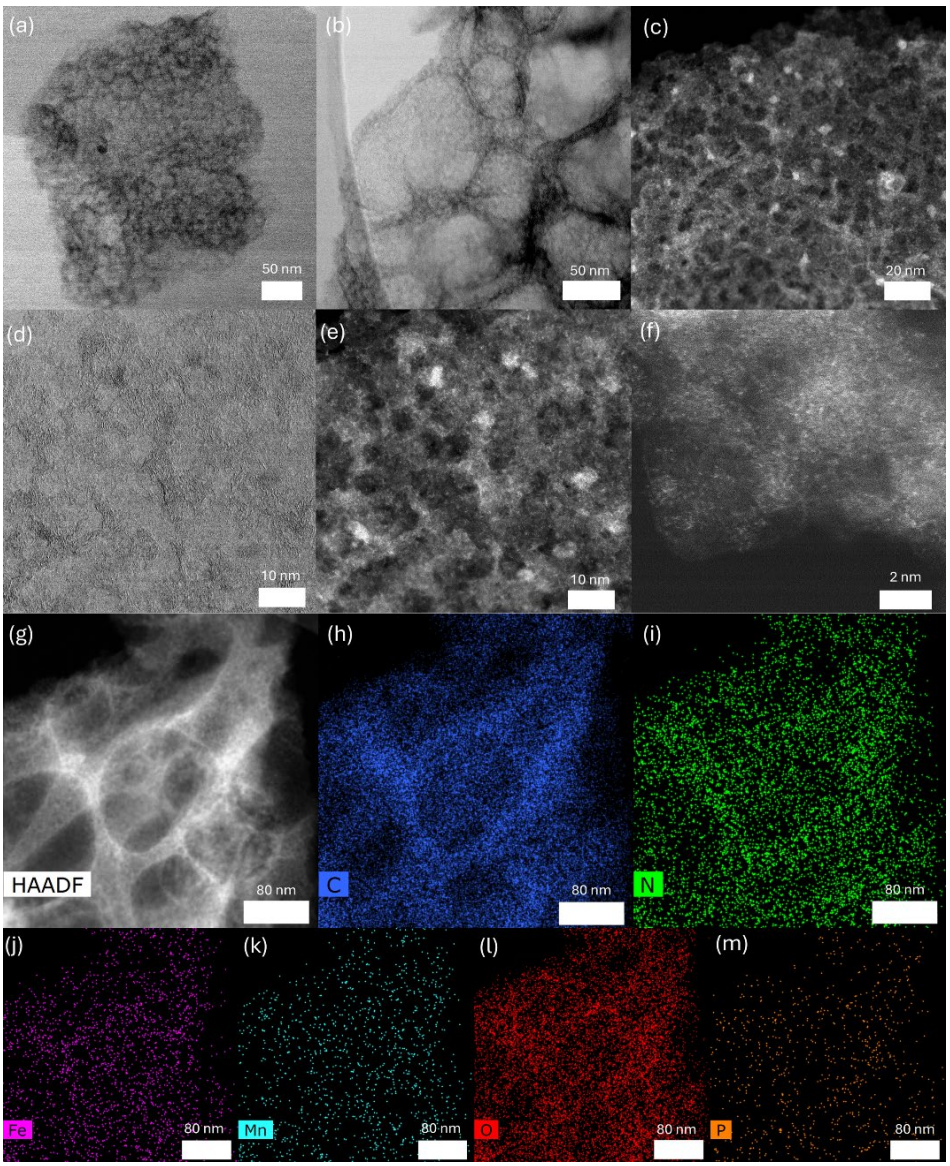

Figure 38. (a,b and d) bright-field STEM images, (c, e–g) HAADF STEM images and (h–m) elemental mappings of carbon, nitrogen, iron, manganese, oxygen, and phosphorus for FeMnIC material.

The Raman spectra of the materials are shown in Figure 39d, showing typical defective carbon bands. The spectra were normalized to the intensity of the G band and further deconvoluted according to the five Voigt-shaped band model into the D4 (1195 cm^{-1}), D1 (1355 cm^{-1}), D3 (1505 cm^{-1}), G (1590 cm^{-1}), and D2 (1615 cm^{-1}) bands [112]. It is evident that the Raman spectra of all the materials are extremely similar to each other, with the $I_{D1}/(I_G + I_{D2})$ ratios between 1.5 and 1.7 for all of the materials. This result is similar to that obtained for ionothermally synthesized materials in the previous work [V], although the differences appear to be even smaller in this case. This is likely because the same pre-synthesized carbon base material was used, which was stable during the second pyrolysis.

Table 16. S_{BET} and S_{dft}, V_{tot}, and V_{micro} of electrocatalyst materials determined via N_2 physisorption analysis.

Material	S_{BET} (m^2 g^{-1})	S_{dft} (m^2 g^{-1})	V_{tot} (cm^3 g^{-1})	V_{micro} (cm^3 g^{-1})
IC2	536	485	0.51	0.08
FeIC	562	571	0.64	0.09
MnIC	431	428	0.50	0.06
FeMnIC	540	483	0.65	0.05

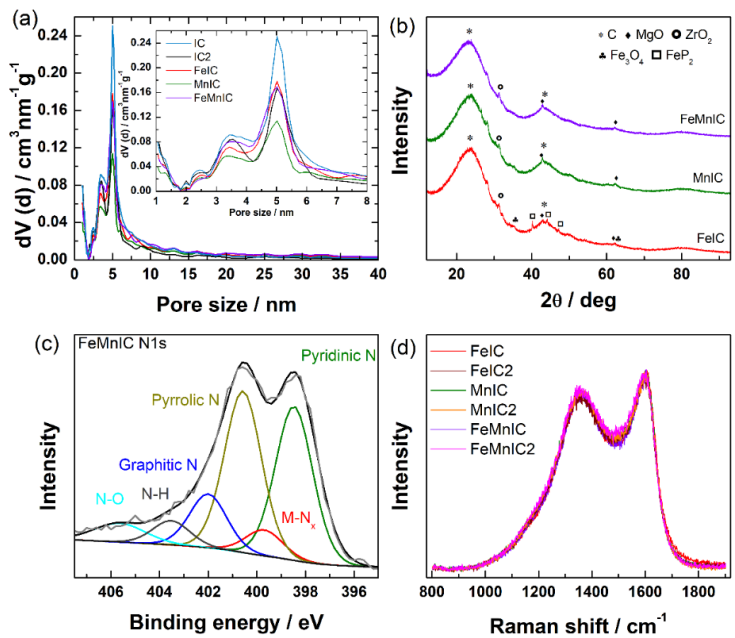

Figure 39. (a) PSD graphs of IC, IC2, FeIC, MnIC, and FeMnIC materials. Inset: magnified section of the PSD. (b) XRD patterns of FeIC, MnIC, and FeMnIC catalyst materials. (c) Deconvoluted N 1s XPS spectra for FeMnIC material. (d) Raman spectra of FeIC, MnIC, FeMnIC, FeIC2, MnIC2, and FeMnIC2 materials.

The RDE method was used to study oxygen electroreduction in an oxygen-saturated 0.1 M KOH solution (Figure 40, Table 17). All the catalysts showed high ORR performance in RDE studies with $E_{1/2}$ values close to that of 20 wt% Pt/C (Table 17). The materials containing only iron (FeIC, FeIC2) and both iron and manganese (FeMnIC, FeMnIC2) showed similarly high ORR activity, as indicated by similar $E_{1/2}$ values around 0.86–0.87 V. Additionally, the MA values at 0.9 V are relatively high (Table 17). The calculated values of C_{dl} of the materials are between 10–18 mF cm^{-2}, indicating relatively similar electrochemically accessible surface areas. The FeIC and FeIC2 materials appear to have a lower C_{dl} compared to the other materials, although the reason for this remains unclear. Before ball milling, the C_{dl} values were around 5–6 mF cm^{-2} for IC2 and 8–9 mF cm^{-2} for FeMnIC2, while after ball milling the values increased to 18 and 13 mF cm^{-2}, respectively. This increase suggests an enhancement in the electrochemically accessible surface area, most likely due to the breakdown of particle agglomerates and improved exposure of porous structures to the electrolyte.

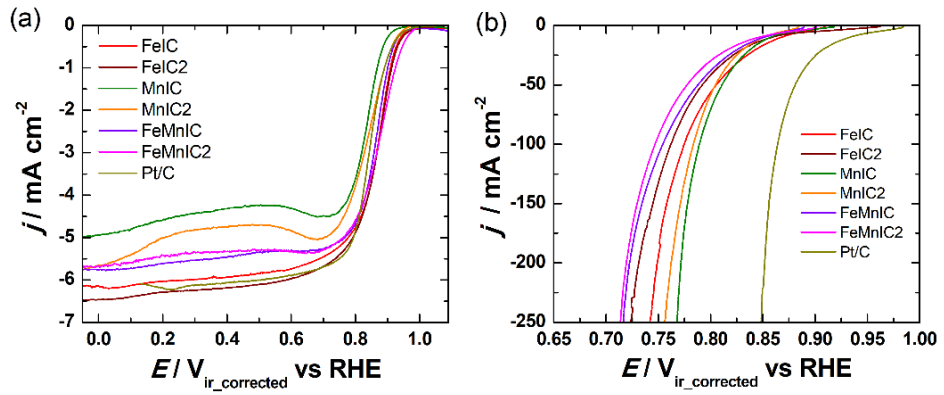

Figure 40. (a) ORR polarization curves for various catalysts measured by RDE in O_2-saturated 0.1 M KOH, ω = 1900 rpm, ν = 10 mV s^{-1} or (b) by GDE in 1 M KOH, at room temperature, in air, ν = 1 mA cm^{-2} s^{-1}.

The GDE method was used to analyze the ORR performance of the catalysts in conditions better resembling AEMFCs. This method can operate at higher current densities, thereby providing a more realistic assessment of catalyst performance [98,101,103]. A simplified GDE setup based on a design by Inaba and co-workers was used, as described in Section 5.3.2. The results show that all the catalyst materials exhibit high ORR performance in GDE analysis (Figure 40b). However, some differences are still observed, with ORR potentials ranging from 0.71–0.77 V at 250 mA cm^{-2}. The reference catalyst, 20 wt% Pt/C, shows higher activity, reaching a current density of 250 mA cm^{-2} at a potential of 0.85 V. The performance of MnIC and MnIC2 at current densities above 50 mA cm^{-2} is higher than that of the other ionothermally prepared materials, in contrast to the RDE data. The reason for this is unclear but may be related to the thicker catalyst layers

used for the GDE measurements, which could enable further reduction of HO_2^- intermediate at other active sites during diffusion through the catalyst layer [21].

Table 17. ORR parameters of different catalysts in 0.1 M KOH, ω = 1900 rpm.

Catalyst	E_{onset}, V	$E_{1/2}$, V	n	C_{dl}, mF cm^{-2}	MA at 0.9 V, A g^{-1}
FeIC	0.96	0.87	3.6 – 3.7	12.9	8.7
MnIC	0.93	0.83	3.7 – 3.8	18.0	1.5
FeMnIC	0.97	0.86	3.7 – 3.8	16.6	6.3
FeIC2	0.96	0.86	3.7 – 3.8	10.5	9.4
MnIC2	0.96	0.83	3.5 – 4	13.8	4.3
FeMnIC2	0.98	0.87	3.8 – 4	13.0	12.9
20 wt% Pt/C	0.97	0.84	3.9 – 4	-	4.3

The stability of electrocatalysts is of great importance for their practical usage. The $E_{1/2}$ value decayed by 20 mV for FeIC (Figure 41a) and by 47 mV for MnIC (Figure 41b) during a short-term stability test using RDE, showing moderate stability. However, there was no apparent change in the $E_{1/2}$ value for the FeMnIC material (Figure 41c). High electrochemical stability for bimetallic iron- and manganese-containing materials has been noted previously [183,184].

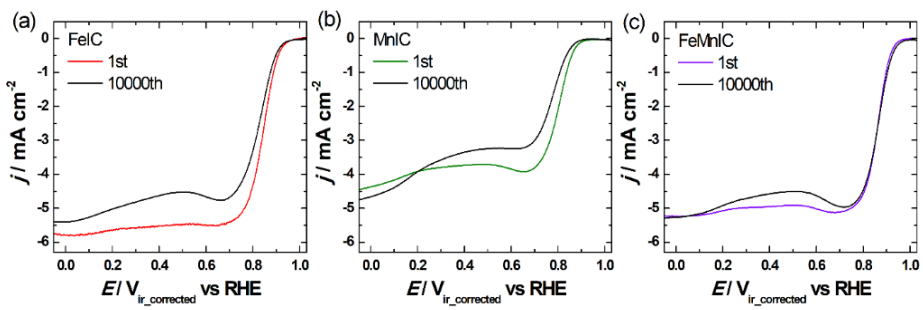

Figure 41. ORR polarization curves for (a) FeIC, (b) MnIC, and (c) FeMnIC catalysts measured by RDE before and after 10000 potential cycles between 1.0 and 0.4 V in 0.1 M KOH. ω = 1900 rpm, ν = 10 mV s^{-1}.

The catalysts were used as cathode catalysts in AEMFCs. The materials showed moderate P_{max} values of 289 mW cm^{-2} for FeIC, 267 mW cm^{-2} for FeMnIC and 222 mW cm^{-2} for MnIC (Figure 42). In comparison, a 20 wt% Pt/C catalyst showed a relatively high P_{max} of 645 mW cm^{-2} at a loading of 0.7 mg cm^{-2} (0.14 mg$_{Pt}$ cm^{-2}). The results line up well with the GDE data where 20 wt% Pt/C appeared more active than the ionothermally prepared materials, which shows that GDE analysis provides a more reliable prediction of AEMFC performance compared to RDE

measurements. The performance was slightly lower than that obtained in our previous work, where P_{max} of 355 mW cm^{-2} was achieved [III]. Further optimizing the AEMFC conditions could lead to better fuel cell performance for the ionothermally prepared catalysts. For example, the ionomer content (I/C ratio) and type have been shown to have a large effect on the performance of AEMFCs [185–187].

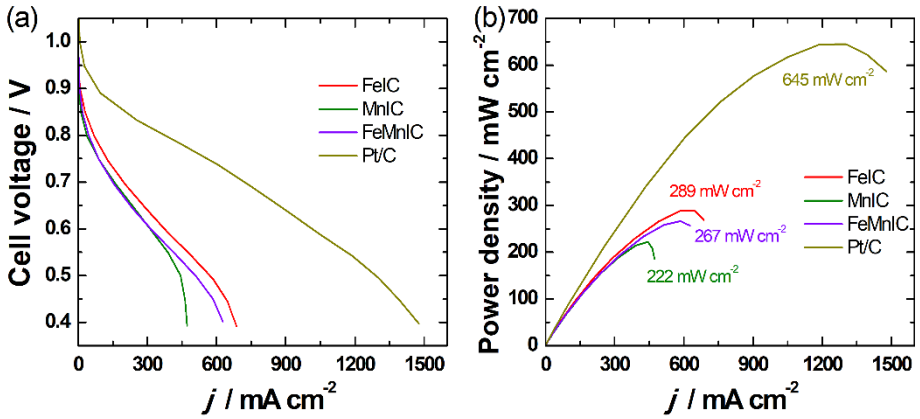

Figure 42. (a) AEMFC polarization and (b) power density curves for FeIC, MnIC, FeMnIC, and 20 wt% Pt/C catalysts. Fully humidified H_2/O_2 gases, 200 kPa backpressure, T = 80 °C. Anode loading 0.8 mg cm^{-2} of 40:20 PtRu/C (0.48 mg$_{PtRu}$ cm^{-2}). Cathode loading 0.7 mg cm^{-2} for Pt/C (0.14 mg$_{Pt}$ cm^{-2}) and 0.9 ± 0.1 mg cm^{-2} for FeIC, MnIC, and FeMnIC.

7. SUMMARY

The aim of the work presented in this PhD thesis was to develop and characterize platinum group metal (PGM)-free electrocatalysts for the oxygen reduction reaction (ORR) and the oxygen evolution reaction (OER) for application in anion-exchange membrane fuel cells (AEMFCs) and metal–air batteries. Nanostructured carbon-based catalysts were synthesized via high-temperature pyrolysis using glucose and rapeseed press cake, a by-product of rapeseed oil production, as carbon precursors. The resulting catalyst materials were thoroughly characterized using various physicochemical and electrochemical techniques to establish relationships between their structure, composition, and electrocatalytic performance.

In the first part of the work, glucose was used as the carbon source in the catalyst synthesis, together with varying amounts of an iron precursor, a nitrogen source, and sodium chloride as a template material [I]. It was found that the ORR activity of the catalysts in alkaline media depended on both metal content and pyrolysis temperature but remained lower than that of a commercial 20% Pt/C catalyst.

In subsequent studies, rapeseed press cake was used as the carbon precursor instead of glucose. A similar synthesis procedure was used, but sodium chloride template was not employed, and in addition to iron-containing materials, cobalt-containing and bimetallic electrocatalysts were also prepared [II]. These materials exhibited significantly higher ORR activity in 0.1 M KOH compared to the glucose-derived catalysts. Furthermore, the effect of acid treatment was investigated, revealing that it significantly increased the specific surface area and also enhanced the ORR activity of the catalysts. However, the most active catalyst, FeCoNCR-a, showed only moderate performance in AEMFCs, achieving a maximum power density (P_{max}) of 131 mW cm^{-2}. Therefore, in the following study, the porous structure of the catalysts was further optimized by incorporating magnesium acetate as a template precursor into the synthesis process [III]. During pyrolysis, magnesium acetate decomposed to form magnesium oxide and magnesium cyanamide nanoparticles, which acted as a sacrificial template and were removed by acid treatment, thereby generating a porous carbon structure. As a result, the pore volume of the optimized material increased by approximately 50% and the specific surface area by about 20% compared to materials synthesized without a template. This led to a significant improvement in ORR activity, reaching that of a 20% Pt/C catalyst. The optimized catalyst, FeNCR-MgAc-3-1, achieved a substantially higher P_{max} of 355 mW cm^{-2} in an AEMFC.

Since this synthesis approach proved successful, it was further applied to the preparation of bifunctional iron- and nickel-containing catalysts for use as air electrode materials in rechargeable zinc–air batteries (RZABs) [IV]. The catalyst with optimized metal content, 4Fe4NiNCR, exhibited high activity for both ORR and OER. When used as an air electrode in RZABs, it achieved a P_{max} of 202 mW cm^{-2} and demonstrated stable cycling performance for 68 h (68 cycles) at

practically relevant conditions. In addition, the effect of RZAB design parameters was studied in detail, revealing that the ratio between the zinc electrode and air electrode areas had a significant influence on the observed P_{max}.

In the last part of the work, an ionothermal method using magnesium nitrate was employed to synthesize mesoporous carbon materials from rapeseed press cake. The carbon materials were subsequently doped with transition metals and nitrogen, to prepare bifunctional iron–nickel catalysts with varying metal ratios [V]. It was observed that their ORR activity decreased with decreasing iron content, while the OER activity remained nearly unchanged. When used as an air electrode catalyst in zinc–air batteries, the FeNiPhenIC material achieved a P_{max} of 179 mW cm^{-2}, which increased to 205 mW cm^{-2} after ball-milling. In addition, the RZAB using the 05Fe05NiPhenIC catalyst maintained stable operation for 65 h (33 cycles) at practically relevant conditions.

The same synthetic approach was further employed to prepare ORR catalysts containing iron and/or manganese [VI]. Rotating disk electrode (RDE) tests showed that these materials exhibited high ORR activity, even surpassing that of a 20% Pt/C catalyst. Gas diffusion electrode (GDE) analysis revealed that their performance differed under practical conditions compared to RDE measurements. The FeIC material achieved a P_{max} of 289 mW cm^{-2} in AEMFCs, which was slightly lower than that of the best-performing material in previous work [III].

The results of this work demonstrate that active PGM-free electrocatalysts can be prepared from biomass-based precursors using a variety of synthesis approaches. The electrocatalytic performance of the catalysts depends on their composition, pore size distribution, specific surface area, and the nature of the active sites. Catalysts with optimized properties can be obtained by carefully selecting the synthesis conditions, adjusting the precursor ratios, and applying templating strategies and post-treatment methods. Properly designed non-precious metal catalysts were shown to achieve ORR activity comparable to that of a 20% Pt/C reference material. When tested in practical systems, these materials enabled high power densities in AEMFCs and RZABs, demonstrating that sustainable, biomass-derived electrocatalysts represent a promising and realistic cost-effective alternative to PGM-based catalysts for future energy conversion and storage technologies.

8. REFERENCES

[1] G.S. Seck, E. Hache, J. Sabathier, F. Guedes, G.A. Reigstad, J. Straus, O. Wolfgang, J.A. Ouassou, M. Askeland, I. Hjorth, H.I. Skjelbred, L.E. Andersson, S. Douguet, M. Villavicencio, J. Trüby, J. Brauer, C. Cabot, Hydrogen and the decarbonization of the energy system in europe in 2050: A detailed model-based analysis, Renew. Sustain. Energy Rev. 167 (2022) 112779. https://doi.org/10.1016/j.rser.2022.112779.

[2] A. Hoogsteyn, J. Meus, K. Bruninx, E. Delarue, Interactions and distortions of different support policies for green hydrogen, Energy Econ. 141 (2025) 108042. https://doi.org/10.1016/j.eneco.2024.108042.

[3] A. Nuñez-Jimenez, N. De Blasio, Competitive and secure renewable hydrogen markets: Three strategic scenarios for the European Union, Int. J. Hydrogen Energy 47 (2022) 35553–35570. https://doi.org/10.1016/j.ijhydene.2022.08.170.

[4] Y. Wang, D.F. Ruiz Diaz, K.S. Chen, Z. Wang, X.C. Adroher, Materials, technological status, and fundamentals of PEM fuel cells – A review, Mater. Today 32 (2020) 178–203. https://doi.org/10.1016/j.mattod.2019.06.005.

[5] H. Lei, X. Yang, Z. Chen, D. Rawach, L. Du, Z. Liang, D. Li, G. Zhang, A.C. Tavares, S. Sun, Multiscale Understanding of Anion Exchange Membrane Fuel Cells: Mechanisms, Electrocatalysts, Polymers, and Cell Management, Adv. Mater. 37 (2025) 2410106. https://doi.org/10.1002/adma.202410106.

[6] A. Sarapuu, J. Lilloja, S. Akula, J.H. Zagal, S. Specchia, K. Tammeveski, Recent Advances in Non-Precious Metal Single-Atom Electrocatalysts for Oxygen Reduction Reaction in Low-Temperature Polymer-Electrolyte Fuel Cells, ChemCatChem 15 (2023) e202300849. https://doi.org/10.1002/cctc.202300849.

[7] H. Adabi, P.G. Santori, A. Shakouri, X. Peng, K. Yassin, I.G. Rasin, S. Brandon, D.R. Dekel, N.U. Hassan, M.-T. Sougrati, A. Zitolo, J.R. Varcoe, J.R. Regalbuto, F. Jaouen, W.E. Mustain, Understanding how single-atom site density drives the performance and durability of PGM-free Fe–N–C cathodes in anion exchange membrane fuel cells, Mater. Today Adv. 12 (2021) 100179. https://doi.org/10.1016/j.mtadv.2021.100179.

[8] Md.M. Hossen, Md.S. Hasan, Md.R.I. Sardar, J. bin Haider, Mottakin, K. Tammeveski, P. Atanassov, State-of-the-art and developmental trends in platinum group metal-free cathode catalyst for anion exchange membrane fuel cell (AEMFC), Appl. Catal. B 325 (2023) 121733. https://doi.org/10.1016/j.apcatb.2022.121733.

[9] T.B. Ferriday, P.H. Middleton, Alkaline fuel cell technology – A review, Int. J. Hydrogen Energy 46 (2021) 18489–18510. https://doi.org/10.1016/j.ijhydene.2021.02.203.

[10] I. Letchumanan, R. Mohamad Yunus, M.S. Mastar@Masdar, N.A. Karim, Advancements in electrocatalyst architecture for enhanced oxygen reduction reaction in anion exchange membrane fuel cells: A comprehensive review, Int. J. Hydrogen Energy 104 (2025) 527–546. https://doi.org/10.1016/j.ijhydene.2024.05.455.

[11] A.A. Kebede, T. Kalogiannis, J. Van Mierlo, M. Berecibar, A comprehensive review of stationary energy storage devices for large scale renewable energy sources grid integration, Renew. Sustain. Energy Rev. 159 (2022) 112213. https://doi.org/10.1016/j.rser.2022.112213.

[12] Y. Kumar, M. Mooste, K. Tammeveski, Recent progress of transition metal-based bifunctional electrocatalysts for rechargeable zinc–air battery application, Curr. Opin. Electrochem. 38 (2023) 101229. https://doi.org/10.1016/j.coelec.2023.101229.
[13] X. Lv, Z. Wang, Z. Lai, Y. Liu, T. Ma, J. Geng, Z. Yuan, Rechargeable Zinc–Air Batteries: Advances, Challenges, and Prospects, Small 20 (2024) 2306396. https://doi.org/10.1002/smll.202306396.
[14] S. Zago, L.C. Scarpetta-Pizo, J.H. Zagal, S. Specchia, PGM-Free Biomass-Derived Electrocatalysts for Oxygen Reduction in Energy Conversion Devices: Promising Materials, Electrochem. Energy Rev. 7 (2024) 1. https://doi.org/10.1007/s41918-023-00197-3.
[15] M. Borghei, J. Lehtonen, L. Liu, O.J. Rojas, Advanced Biomass-Derived Electrocatalysts for the Oxygen Reduction Reaction, Adv. Mater. 30 (2018) 1703691. https://doi.org/10.1002/adma.201703691.
[16] N.A.A. Qasem, G.A.Q. Abdulrahman, A Recent Comprehensive Review of Fuel Cells: History, Types, and Applications, Int. J. Energy Res. 2024 (2024) 7271748. https://doi.org/10.1155/2024/7271748.
[17] O.B. Inal, C. Deniz, Assessment of fuel cell types for ships: Based on multi-criteria decision analysis, J. Clean. Prod. 265 (2020) 121734. https://doi.org/10.1016/j.jclepro.2020.121734.
[18] W.-H. Chen, P.P. Biswas, H.C. Ong, A.T. Hoang, T.-B. Nguyen, C.-D. Dong, A critical and systematic review of sustainable hydrogen production from ethanol/bioethanol: Steam reforming, partial oxidation, and autothermal reforming, Fuel 333 (2023) 126526. https://doi.org/10.1016/j.fuel.2022.126526.
[19] M.A. Aminudin, S.K. Kamarudin, B.H. Lim, E.H. Majilan, M.S. Masdar, N. Shaari, An overview: Current progress on hydrogen fuel cell vehicles, Int. J. Hydrogen Energy 48 (2023) 4371–4388. https://doi.org/10.1016/j.ijhydene.2022.10.156.
[20] D.R. Dekel, Review of cell performance in anion exchange membrane fuel cells, J. Power Sources 375 (2018) 158–169. https://doi.org/10.1016/j.jpowsour.2017.07.117.
[21] K. Artyushkova, S. Rojas-Carbonell, C. Santoro, E. Weiler, A. Serov, R. Awais, R.R. Gokhale, P. Atanassov, Correlations between Synthesis and Performance of Fe-Based PGM-Free Catalysts in Acidic and Alkaline Media: Evolution of Surface Chemistry and Morphology, ACS Appl. Energy Mater. 2 (2019) 5406–5418. https://doi.org/10.1021/acsaem.9b00331.
[22] C. Wei, R.R. Rao, J. Peng, B. Huang, I.E.L. Stephens, M. Risch, Z.J. Xu, Y. Shao-Horn, Recommended Practices and Benchmark Activity for Hydrogen and Oxygen Electrocatalysis in Water Splitting and Fuel Cells, Adv. Mater. 31 (2019) 1806296. https://doi.org/10.1002/adma.201806296.
[23] S. Gottesfeld, D.R. Dekel, M. Page, C. Bae, Y. Yan, P. Zelenay, Y.S. Kim, Anion exchange membrane fuel cells: Current status and remaining challenges, J. Power Sources 375 (2018) 170–184. https://doi.org/10.1016/j.jpowsour.2017.08.010.
[24] B. Zhang, Y. Hua, Z. Gao, Strategies to optimize water management in anion exchange membrane fuel cells, J. Power Sources 525 (2022) 231141. https://doi.org/10.1016/j.jpowsour.2022.231141.
[25] H. Grimler, A. Carlson, H. Ekström, C. Lagergren, R. Wreland Lindström, G. Lindbergh, Determination of Kinetic Parameters for the Oxygen Reduction

Reaction on Platinum in an AEMFC, J. Electrochem. Soc. 168 (2021) 124501. https://doi.org/10.1149/1945-7111/ac38f8.
[26] O.E. Herrera, D.P. Wilkinson, W. Mérida, Anode and cathode overpotentials and temperature profiles in a PEMFC, J. Power Sources 198 (2012) 132–142. https://doi.org/10.1016/j.jpowsour.2011.09.042.
[27] N. Ramaswamy, S. Mukerjee, Alkaline Anion-Exchange Membrane Fuel Cells: Challenges in Electrocatalysis and Interfacial Charge Transfer, Chem. Rev. 119 (2019) 11945–11979. https://doi.org/10.1021/acs.chemrev.9b00157.
[28] M.-J. Kim, J.E. Park, S. Kim, M.S. Lim, A. Jin, O.-H. Kim, M.J. Kim, K.-S. Lee, J. Kim, S.-S. Kim, Y.-H. Cho, Y.-E. Sung, Biomass-Derived Air Cathode Materials: Pore-Controlled S,N-Co-doped Carbon for Fuel Cells and Metal–Air Batteries, ACS Catal. 9 (2019) 3389–3398. https://doi.org/10.1021/acscatal.8b03730.
[29] H.S. Kim, J. Lee, J.-H. Jang, H. Jin, V.K. Paidi, S.-H. Lee, K.-S. Lee, P. Kim, S.J. Yoo, Waste pig blood-derived 2D Fe single-atom porous carbon as an efficient electrocatalyst for zinc–air batteries and AEMFCs, Appl. Surf. Sci. 563 (2021) 150208. https://doi.org/10.1016/j.apsusc.2021.150208.
[30] I.J.R. Sarkar, S.G. Peera, R. Chetty, Fe–N–C catalyst derived from solid-state coordination complex as durable oxygen reduction electrocatalyst in alkaline electrolyte, Ionics 26 (2020) 5685–5696. https://doi.org/10.1007/s11581-020-03722-2.
[31] P. Teppor, R. Jäger, M. Koppel, O. Volobujeva, R. Palm, M. Månsson, E. Härk, Z. Kochovski, J. Aruväli, K. Kooser, S. Granroth, T. Käämbre, J. Nerut, E. Lust, Unlocking the porosity of Fe–N–C catalysts using hydroxyapatite as a hard template en route to eco-friendly high-performance AEMFCs, J. Power Sources 591 (2024) 233816. https://doi.org/10.1016/j.jpowsour.2023.233816.
[32] M. Muhyuddin, A. Friedman, F. Poli, E. Petri, H. Honig, F. Basile, A. Fasolini, R. Lorenzi, E. Berretti, M. Bellini, A. Lavacchi, L. Elbaz, C. Santoro, F. Soavi, Lignin-derived bimetallic platinum group metal-free oxygen reduction reaction electrocatalysts for acid and alkaline fuel cells, J. Power Sources 556 (2023) 232416. https://doi.org/10.1016/j.jpowsour.2022.232416.
[33] S. Pérez-Rodríguez, D. Torres, M.T. Izquierdo, A. Zitolo, N. Bibent, M. Sougrati, F. Jaouen, A. Celzard, V. Fierro, Hierarchical Porous Fe3C@Fe-N-C Catalysts from Tannin-Fe(III) Complexes for Efficient Oxygen Reduction, Small (2024) 2406887. https://doi.org/10.1002/smll.202406887.
[34] U. Sajjad, A. Sarapuu, J.C. Douglin, A. Kikas, A. Treshchalov, M. Käärik, J. Kozlova, J. Aruväli, J. Leis, V. Kisand, K. Kukli, D.R. Dekel, K. Tammeveski, Lignin-Derived Precious Metal-Free Electrocatalysts for Anion-Exchange Membrane Fuel Cell Application, ACS Catal. 14 (2024) 9224–9234. https://doi.org/10.1021/acscatal.4c02136.
[35] S. Ravichandran, A. Kausalya, X. Ji, S. Lakshmipathi, H. Su, D. Chen, J. Yu, Defect engineering coupled with N/O Co-doping in lignin-derived carbon for enhanced ORR in anion exchange membrane fuel cells, Carbon 247 (2026) 121057. https://doi.org/10.1016/j.carbon.2025.121057.
[36] M.S. Cho, Y. Zang, S.J. Park, B. An, H.J. Lee, A. Gaur, G. Ali, M. Kim, K.Y. Chung, S. Park, Y. Sung, D. Kim, K.J. Kim, C.W. Myung, H. Han, Synergistic Fe–Si Dual-Site Pathway Engineering in Biomass-Derived Carbon Matrix for High-Performance Oxygen Reduction Reaction, Carbon Energy 8 (2026) e70154. https://doi.org/10.1002/cey2.70154.

[37] D. Nagane, D. Nilegave, S. Girawale, S. Patil, G. Shaikh, V. Jadhav, P. Vairale, A. Pathak, S.P. Patole, S. Jadkar, Neem-derived carbon-cobalt oxide composite (Co3O4@NC): A sustainable and cost-effective catalyst for oxygen reduction in fuel cells, J. Power Sources 645 (2025) 237173. https://doi.org/10.1016/j.jpowsour.2025.237173.
[38] J. Yi, P. Liang, X. Liu, K. Wu, Y. Liu, Y. Wang, Y. Xia, J. Zhang, Challenges, mitigation strategies and perspectives in development of zinc-electrode materials and fabrication for rechargeable zinc–air batteries, Energy Environ. Sci. 11 (2018) 3075–3095. https://doi.org/10.1039/C8EE01991F.
[39] G. Nazir, A. Rehman, J.-H. Lee, C.-H. Kim, J. Gautam, K. Heo, S. Hussain, M. Ikram, A.A. AlObaid, S.-Y. Lee, S.-J. Park, A Review of Rechargeable Zinc–Air Batteries: Recent Progress and Future Perspectives, Nanomicro Lett. 16 (2024) 138. https://doi.org/10.1007/s40820-024-01328-1.
[40] W. Shao, R. Yan, M. Zhou, L. Ma, C. Roth, T. Ma, S. Cao, C. Cheng, B. Yin, S. Li, Carbon-Based Electrodes for Advanced Zinc-Air Batteries: Oxygen-Catalytic Site Regulation and Nanostructure Design, Electrochem. Energy Rev. 6 (2023) 11. https://doi.org/10.1007/s41918-023-00181-x.
[41] J. Fu, Z.P. Cano, M.G. Park, A. Yu, M. Fowler, Z. Chen, Electrically Rechargeable Zinc–Air Batteries: Progress, Challenges, and Perspectives, Adv. Mater. 29 (2017) 1604685. https://doi.org/10.1002/adma.201604685.
[42] J.F. Parker, J.S. Ko, D.R. Rolison, J.W. Long, Translating Materials-Level Performance into Device-Relevant Metrics for Zinc-Based Batteries, Joule 2 (2018) 2519–2527. https://doi.org/10.1016/j.joule.2018.11.007.
[43] X. Bi, Y. Jiang, R. Chen, Y. Du, Y. Zheng, R. Yang, R. Wang, J. Wang, X. Wang, Z. Chen, Rechargeable Zinc–Air versus Lithium–Air Battery: from Fundamental Promises Toward Technological Potentials, Adv. Energy Mater. 14 (2024) 2302388. https://doi.org/10.1002/aenm.202302388.
[44] J.-N. Liu, C.-X. Zhao, J. Wang, D. Ren, B.-Q. Li, Q. Zhang, A brief history of zinc–air batteries: 140 years of epic adventures, Energy Environ. Sci. 15 (2022) 4542–4553. https://doi.org/10.1039/D2EE02440C.
[45] D. Fuchs, C. Müller, M. Schaffeld, F. Mahlendorf, H.E. Hoster, New Insights Into Zinc Passivation Through Operando Measured Zincate Concentrations, Batter. Supercaps 7 (2024). https://doi.org/10.1002/batt.202400298.
[46] M. Bockelmann, L. Reining, U. Kunz, T. Turek, Electrochemical characterization and mathematical modeling of zinc passivation in alkaline solutions: A review, Electrochim. Acta 237 (2017) 276–298. https://doi.org/10.1016/j.electacta.2017.03.143.
[47] H. Wu, T. Zhang, J. Zhu, G. Li, H. Liu, Highly efficient corrosion inhibitor for low charge voltage and long lifespan rechargeable aqueous zinc-air battery, J. Chem Eng. 496 (2024) 153819. https://doi.org/10.1016/j.cej.2024.153819.
[48] Y. Zhao, D.P. Adiyeri Saseendran, C. Huang, C.A. Triana, W.R. Marks, H. Chen, H. Zhao, G.R. Patzke, Oxygen Evolution/Reduction Reaction Catalysts: From *In Situ* Monitoring and Reaction Mechanisms to Rational Design, Chem. Rev. 123 (2023) 6257–6358. https://doi.org/10.1021/acs.chemrev.2c00515.
[49] K. Wang, P. Pei, Z. Ma, H. Chen, H. Xu, D. Chen, H. Xing, Growth of oxygen bubbles during recharge process in zinc-air battery, J. Power Sources 296 (2015) 40–45. https://doi.org/10.1016/j.jpowsour.2015.07.039.

[50] Y. He, Z. Zhao, Y. Cui, W. Shang, Y. Chen, P. Tan, Boosting gaseous oxygen transport in a Zn-air battery for high-rate charging by a bubble diode-inspired air electrode, Energy Storage Mater. 57 (2023) 360–370. https://doi.org/10.1016/j.ensm.2023.02.030.
[51] Y. He, Y. Cui, W. Shang, Z. Zhao, P. Tan, Insight into the bubble-induced overpotential towards high-rate charging of Zn-air batteries, Chem. Eng. J. 448 (2022) 137782. https://doi.org/10.1016/j.cej.2022.137782.
[52] X. Zhong, X. Xiao, Q. Li, M. Zhang, Z. Li, L. Gao, B. Chen, Z. Zheng, Q. Fu, X. Wang, G. Zhou, B. Xu, Understanding the active site in chameleon-like bi-functional catalyst for practical rechargeable zinc-air batteries, Nat. Commun. 15 (2024) 9616. https://doi.org/10.1038/s41467-024-54019-1.
[53] Q. Wang, S. Kaushik, X. Xiao, Q. Xu, Sustainable zinc–air battery chemistry: advances, challenges and prospects, Chem. Soc. Rev. 52 (2023) 6139–6190. https://doi.org/10.1039/D2CS00684G.
[54] D. Jiao, Z. Ma, J. Li, Y. Han, J. Mao, T. Ling, S. Qiao, Test factors affecting the performance of zinc–air battery, J. Energy Chem. 44 (2020) 1–7. https://doi.org/10.1016/j.jechem.2019.09.008.
[55] S.S. Shinde, N.K. Wagh, C.H. Lee, D. Kim, S. Kim, H. Um, S.U. Lee, J. Lee, Scaling-Up Insights for Zinc–Air Battery Technologies Realizing Reversible Zinc Anodes, Adv. Mater. 35 (2023). https://doi.org/10.1002/adma.202303509.
[56] Y. Liu, K. Sun, X. Cui, B. Li, J. Jiang, Defect-Rich, Graphenelike Carbon Sheets Derived from Biomass as Efficient Electrocatalysts for Rechargeable Zinc–Air Batteries, ACS Sustain. Chem. Eng. 8 (2020) 2981–2989. https://doi.org/10.1021/acssuschemeng.9b07621.
[57] X. He, Y. Zhang, J. Wang, J. Li, L. Yu, F. Zhou, J. Li, X. Shen, X. Wang, S. Wang, H. Jin, Biomass-Derived Fe_2N@NCNTs from Bioaccumulation as an Efficient Electrocatalyst for Oxygen Reduction and Zn–Air Battery, ACS Sustain. Chem. Eng. 10 (2022) 9105–9112. https://doi.org/10.1021/acssuschemeng.2c01790.
[58] W. Chen, H. Yu, S. Chang, W. Li, R. Liu, Y. Wang, H. Zhang, Z. Zhang, Wheat straw as carbon source to prepare FeCoP2 / N, P Dual-Doped carbon matrix as bifunctional catalyst for application in rechargeable Zinc-air and Aluminum-air batteries, Appl. Surf. Sci. 573 (2022) 151486. https://doi.org/10.1016/j.apsusc.2021.151486.
[59] L. Xu, D. Deng, Y. Tian, H. Li, J. Qian, J. Wu, H. Li, Dual-active-sites design of CoNx anchored on zinc-coordinated nitrogen-codoped porous carbon with efficient oxygen catalysis for high-stable rechargeable zinc-air batteries, Chem Eng. J. 408 (2021) 127321. https://doi.org/10.1016/j.cej.2020.127321.
[60] P. Zhang, Y. Liu, S. Wang, L. Zhou, T. Liu, K. Sun, H. Cao, J. Jiang, X. Wu, B. Li, Wood-Derived Monolithic Catalysts with the Ability of Activating Water Molecules for Oxygen Electrocatalysis, Small 18 (2022) 2202725. https://doi.org/10.1002/smll.202202725.
[61] X. Xiao, W. Zhang, H. Zhao, L. Li, P. Deng, Y. Wu, S. Luo, B. Chen, Ultrathin amorphous MnO2 modified prawn shells-derived porous carbon towards robust oxygen electrocatalyst for rechargeable Zn-air battery, Ceram. Int. 48 (2022) 6506–6511. https://doi.org/10.1016/j.ceramint.2021.11.195.
[62] L. Zhong, C. Jiang, M. Zheng, X. Peng, T. Liu, S. Xi, X. Chi, Q. Zhang, L. Gu, S. Zhang, G. Shi, L. Zhang, K. Wu, Z. Chen, T. Li, M. Dahbi, J. Alami, K. Amine, J. Lu, Wood Carbon Based Single-Atom Catalyst for Rechargeable Zn–Air Batteries, ACS Energy Lett. 6 (2021) 3624–3633.

https://doi.org/10.1021/acsenergylett.1c01678.
[63] G. Zhang, X. Liu, L. Wang, F. Sun, Y. Yang, C. Tian, P. Yu, Q. Pan, H. Fu, B,N-Doped Defective Carbon Entangled Fe $_3$ C Nanoparticles as the Superior Oxygen Reduction Electrocatalyst for Zn–Air Batteries, ACS Sustain. Chem. Eng. 7 (2019) 19104–19112. https://doi.org/10.1021/acssuschemeng.9b05033.
[64] Z. Ma, Y. Han, X. Wang, G. Sun, Y. Li, Lignin-based nitrogen/sulfur dual-doped nanosheets decorated with Co1−xS nanoparticles as efficient bifunctional oxygen electrocatalysts, J. Colloid Interface Sci. 634 (2023) 469–480. https://doi.org/10.1016/j.jcis.2022.12.070.
[65] X. Xiao, X. Hu, Y. Liang, G. Zhang, X. Wang, Y. Yan, X. Li, G. Yan, J. Wang, Anchoring NiCo2O4 nanowhiskers in biomass-derived porous carbon as superior oxygen electrocatalyst for rechargeable Zn-air battery, J. Power Sources 476 (2020) 228684. https://doi.org/10.1016/j.jpowsour.2020.228684.
[66] Y. Wang, K. Sheng, R. Xu, Z. Chen, K. Shi, W. Li, J. Li, Efficient bifunctional 3D porous Co–N–C catalyst from spent Li–ion batteries and biomass for Zinc–Air batteries, Chem. Eng. Sci. 268 (2023) 118433. https://doi.org/10.1016/j.ces.2022.118433.
[67] Y. Zhao, X. Liu, Y. Liu, Y. Chen, S. Gao, Favorable pore size distribution of biomass-derived N, S dual-doped carbon materials for advanced oxygen reduction reaction, Int. J. Hydrogen Energy 47 (2022) 12964–12974. https://doi.org/10.1016/j.ijhydene.2022.02.064.
[68] J. Zhang, M. Zhang, Y. Zeng, J. Chen, L. Qiu, H. Zhou, C. Sun, Y. Yu, C. Zhu, Z. Zhu, Single Fe Atom on Hierarchically Porous S, N-Codoped Nanocarbon Derived from Porphyra Enable Boosted Oxygen Catalysis for Rechargeable Zn-Air Batteries, Small 15 (2019) 1900307. https://doi.org/10.1002/smll.201900307.
[69] J. Nie, M. Dong, G. Chen, N. Wang, J. Nie, G. Ma, Biomass-based Hierarchical Porous ORR and OER Bifunctional Catalysts with Strong Stability for Zn-Air Batteries, ACS Sustain. Chem. Eng. 11 (2023) 11161–11171. https://doi.org/10.1021/acssuschemeng.3c01866.
[70] S. Aralekallu, V. Singh, M-N-C-based non-precious metal catalyst materials for electrocatalytic ORR applications, Fuel 404 (2026) 136163. https://doi.org/10.1016/j.fuel.2025.136163.
[71] M.S. Thorum, J.M. Hankett, A.A. Gewirth, Poisoning the Oxygen Reduction Reaction on Carbon-Supported Fe and Cu Electrocatalysts: Evidence for Metal-Centered Activity, J. Phys. Chem. Lett. 2 (2011) 295–298. https://doi.org/10.1021/jz1016284.
[72] A. Sarapuu, E. Kibena-Põldsepp, M. Borghei, K. Tammeveski, Electrocatalysis of oxygen reduction on heteroatom-doped nanocarbons and transition metal–nitrogen–carbon catalysts for alkaline membrane fuel cells, J. Mater. Chem. A 6 (2018) 776–804. https://doi.org/10.1039/C7TA08690C.
[73] L. Yang, D. Cheng, H. Xu, X. Zeng, X. Wan, J. Shui, Z. Xiang, D. Cao, Unveiling the high-activity origin of single-atom iron catalysts for oxygen reduction reaction, Proc. Natl. Acad. Sci. U.S.A. 115 (2018) 6626–6631. https://doi.org/10.1073/pnas.1800771115.
[74] W. Chen, Y. Qin, C. Heng, S. Wang, M. Ge, Y. Li, X. Wan, X. Li, J. Shui, Y. Su, D. Su, Degradation of FeNC Electrocatalysts for Acidic and Alkaline Oxygen Reduction, J. Am. Chem. Soc. 147 (2025) 35730–35741. https://doi.org/10.1021/jacs.5c11985.

[75] H. Chang, Y.-F. Guo, X. Liu, P.-F. Wang, Y. Xie, T.-F. Yi, Dual MOF-derived Fe/N/P-tridoped carbon nanotube as high-performance oxygen reduction catalysts for zinc-air batteries, Appl. Catal. B 327 (2023) 122469. https://doi.org/10.1016/j.apcatb.2023.122469.
[76] D. Zhang, X. Zhang, X. Li, C. Feng, Y. Chu, C. Chen, Z. Kou, Modulating single-atom M-N-C electrocatalysts for the oxygen reduction: the insights beyond the first coordination shell, Energy Mater. 5 (2025) 500014. https://doi.org/10.20517/energymater.2024.42.
[77] J. Quílez-Bermejo, E. Morallón, D. Cazorla-Amorós, Metal-free heteroatom-doped carbon-based catalysts for ORR: A critical assessment about the role of heteroatoms, Carbon 165 (2020) 434–454. https://doi.org/10.1016/j.carbon.2020.04.068.
[78] M.A. Ahsan, A.R. Puente Santiago, A. Rodriguez, V. Maturano-Rojas, B. Alvarado-Tenorio, R. Bernal, J.C. Noveron, Biomass-derived ultrathin carbon-shell coated iron nanoparticles as high-performance tri-functional HER, ORR and Fenton-like catalysts, J. Clean. Prod. 275 (2020) 124141. https://doi.org/10.1016/j.jclepro.2020.124141.
[79] Z. Wang, Z. Lu, Q. Ye, Z. Yang, R. Xu, K. Kong, Y. Zhang, T. Yan, Y. Liu, Z. Pan, Y. Huang, X. Lu, Construction of Fe Nanoclusters/Nanoparticles to Engineer FeN_4 Sites on Multichannel Porous Carbon Fibers for Boosting Oxygen Reduction Reaction, Adv. Funct. Mater. 34 (2024) 2315150. https://doi.org/10.1002/adfm.202315150.
[80] J.M. Yoo, H. Shin, D.Y. Chung, Y.-E. Sung, Carbon Shell on Active Nanocatalyst for Stable Electrocatalysis, Acc. Chem. Res. 55 (2022) 1278–1289. https://doi.org/10.1021/acs.accounts.1c00727.
[81] M. Sharma, J.-H. Jang, D.Y. Shin, J.A. Kwon, D.-H. Lim, D. Choi, H. Sung, J. Jang, S.-Y. Lee, K.Y. Lee, H.-Y. Park, N. Jung, S.J. Yoo, Work function-tailored graphene *via* transition metal encapsulation as a highly active and durable catalyst for the oxygen reduction reaction, Energy Environ. Sci. 12 (2019) 2200–2211. https://doi.org/10.1039/C9EE00381A.
[82] H. Yang, L. Shang, Q. Zhang, R. Shi, G.I.N. Waterhouse, L. Gu, T. Zhang, A universal ligand mediated method for large scale synthesis of transition metal single atom catalysts, Nat. Commun. 10 (2019) 4585. https://doi.org/10.1038/s41467-019-12510-0.
[83] Y. Wang, N. Katyal, Y. Tang, H. Li, K. Shin, W. Liu, R. He, M. Xu, G. Henkelman, S. Bao, One-Step Pyrolysis Construction of Bimetallic Atom-Cluster Sites for Boosting Bifunctional Catalytic Activity in Zn-Air Batteries, Small 20 (2024) 2306504. https://doi.org/10.1002/smll.202306504.
[84] L. Trotochaud, S.L. Young, J.K. Ranney, S.W. Boettcher, Nickel–Iron Oxy-hydroxide Oxygen-Evolution Electrocatalysts: The Role of Intentional and Incidental Iron Incorporation, J. Am. Chem. Soc. 136 (2014) 6744–6753. https://doi.org/10.1021/ja502379c.
[85] G.-L. Chai, K. Qiu, M. Qiao, M.-M. Titirici, C. Shang, Z. Guo, Active sites engineering leads to exceptional ORR and OER bifunctionality in P,N Co-doped graphene frameworks, Energy Environ. Sci. 10 (2017) 1186–1195. https://doi.org/10.1039/C6EE03446B.
[86] X.-L. Zhou, H. Zhang, L.-M. Shao, F. Lü, P.-J. He, Preparation and Application of Hierarchical Porous Carbon Materials from Waste and Biomass: A Review, Waste

Biomass Valorization 12 (2021) 1699–1724. https://doi.org/10.1007/s12649-020-01109-y.
[87] S. Schrettl, B. Schulte, H. Frauenrath, Templating for hierarchical structure control in carbon materials, Nanoscale 8 (2016) 18828–18848. https://doi.org/10.1039/C6NR06695J.
[88] S.H. Lee, J. Kim, D.Y. Chung, J.M. Yoo, H.S. Lee, M.J. Kim, B.S. Mun, S.G. Kwon, Y.-E. Sung, T. Hyeon, Design Principle of Fe–N–C Electrocatalysts: How to Optimize Multimodal Porous Structures?, J. Am. Chem. Soc. 141 (2019) 2035–2045. https://doi.org/10.1021/jacs.8b11129.
[89] N. Díez, M. Sevilla, A.B. Fuertes, Synthesis strategies of templated porous carbons beyond the silica nanocasting technique, Carbon 178 (2021) 451–476. https://doi.org/10.1016/j.carbon.2021.03.029.
[90] H. Nishihara, T. Kyotani, Templated Nanocarbons for Energy Storage, Adv. Mater. 24 (2012) 4473–4498. https://doi.org/10.1002/adma.201201715.
[91] J. Lilloja, M. Mooste, E. Kibena-Põldsepp, A. Sarapuu, B. Zulevi, A. Kikas, H.-M. Piirsoo, A. Tamm, V. Kisand, S. Holdcroft, A. Serov, K. Tammeveski, Mesoporous iron-nitrogen co-doped carbon material as cathode catalyst for the anion exchange membrane fuel cell, J. Power Source Adv. 8 (2021) 100052. https://doi.org/10.1016/j.powera.2021.100052.
[92] K. Kisand, A. Sarapuu, J.C. Douglin, A. Kikas, A. Treshchalov, M. Käärik, H.-M. Piirsoo, P. Paiste, J. Aruväli, J. Leis, V. Kisand, A. Tamm, D.R. Dekel, K. Tammeveski, Templated Nitrogen-, Iron-, and Cobalt-Doped Mesoporous Nanocarbon Derived from an Alkylresorcinol Mixture for Anion-Exchange Membrane Fuel Cell Application, ACS Catal. 12 (2022) 14050–14061. https://doi.org/10.1021/acscatal.2c03683.
[93] X.F. Lu, B.Y. Xia, S. Zang, X.W. (David) Lou, Metal–Organic Frameworks Based Electrocatalysts for the Oxygen Reduction Reaction, Angew. Chem. 132 (2020) 4662–4678. https://doi.org/10.1002/ange.201910309.
[94] N. Sun, S.S.A. Shah, Z. Lin, Y.-Z. Zheng, L. Jiao, H.-L. Jiang, MOF-Based Electrocatalysts: An Overview from the Perspective of Structural Design, Chem. Rev. 125 (2025) 2703–2792. https://doi.org/10.1021/acs.chemrev.4c00664.
[95] R. Kumar, M. Mooste, I. Zekker, J. Kozlova, M. Käärik, M. Otsus, A. Treshchalov, J. Aruväli, J. Leis, A. Kikas, V. Kisand, K. Kukli, K. Tammeveski, Mn-N-C material with high-density and accessible Mn-Nx sites emerging as an efficient oxygen reduction reaction electrocatalyst for AEMFCs, J. Power Sources 667 (2026) 239191. https://doi.org/10.1016/j.jpowsour.2025.239191.
[96] R. Kumar, M. Mooste, Z. Ahmed, S. Akula, I. Zekker, M. Marandi, M. Käärik, J. Leis, A. Kikas, A. Treshchalov, M. Otsus, J. Aruväli, V. Kisand, A. Tamm, K. Tammeveski, Highly active ZIF-8@CNT composite catalysts as cathode materials for anion exchange membrane fuel cells, Ind. Chem. Mater. 1 (2023) 526–541. https://doi.org/10.1039/D3IM00081H.
[97] S. Lee, S. Pyun, S. Lee, S.L. Kang, Fundamentals of Rotating Disc and Ring–Disc Electrode Techniques and their Applications to Study of the Oxygen Reduction Mechanism at Pt/C Electrode for Fuel Cells, Isr. J. Chem. 48 (2008) 215–228. https://doi.org/10.1560/IJC.48.3-4.215.
[98] K.-A. Kasuk, J. Nerut, V. Grozovski, E. Lust, A. Kucernak, Design and Impact: Navigating the Electrochemical Characterization Methods for Supported Catalysts, ACS Catal. 14 (2024) 11949–11966. https://doi.org/10.1021/acscatal.4c03271.

[99] J. Masa, C. Batchelor-McAuley, W. Schuhmann, R.G. Compton, Koutecky-Levich analysis applied to nanoparticle modified rotating disk electrodes: Electrocatalysis or misinterpretation, Nano Res. 7 (2014) 71–78. https://doi.org/10.1007/s12274-013-0372-0.
[100] L. Bouleau, S. Pérez-Rodríguez, J. Quílez-Bermejo, M.T. Izquierdo, F. Xu, V. Fierro, A. Celzard, Best practices for ORR performance evaluation of metal-free porous carbon electrocatalysts, Carbon 189 (2022) 349–361. https://doi.org/10.1016/j.carbon.2021.12.078.
[101] V. Gridin, J. Du, S. Haller, P. Theis, K. Hofmann, G.K.H. Wiberg, U.I. Kramm, M. Arenz, GDE vs RDE: Impact of operation conditions on intrinsic catalytic parameters of FeNC catalyst for the oxygen reduction reaction, Electrochim. Acta 444 (2023) 142012. https://doi.org/10.1016/j.electacta.2023.142012.
[102] M. Inaba, A.W. Jensen, G.W. Sievers, M. Escudero-Escribano, A. Zana, M. Arenz, Benchmarking high surface area electrocatalysts in a gas diffusion electrode: measurement of oxygen reduction activities under realistic conditions, Energy Environ. Sci. 11 (2018) 988–994. https://doi.org/10.1039/C8EE00019K.
[103] K. Ehelebe, N. Schmitt, G. Sievers, A.W. Jensen, A. Hrnjić, P. Collantes Jiménez, P. Kaiser, M. Geuß, Y.-P. Ku, P. Jovanovič, K.J.J. Mayrhofer, B. Etzold, N. Hodnik, M. Escudero-Escribano, M. Arenz, S. Cherevko, Benchmarking Fuel Cell Electrocatalysts Using Gas Diffusion Electrodes: Inter-lab Comparison and Best Practices, ACS Energy Lett. 7 (2022) 816–826. https://doi.org/10.1021/acsenergylett.1c02659.
[104] C.-T. Lu, Z.-Y. Zhu, S.-W. Chen, Y.-L. Chang, K.-L. Hsueh, Effects of Cell Design Parameters on Zinc-Air Battery Performance, Batteries 8 (2022) 92. https://doi.org/10.3390/batteries8080092.
[105] S.M. Zahan, A.A. Baranov, K. Yassin, J. Zhong, J.C. Douglin, S. Willdorf-Cohen, S. Bhowmick, J. Lilloja, K. Tammeveski, Y. Tsur, D.R. Dekel, Can Anion-Exchange Membrane Fuel Cells Operate with Ambient Air?, ACS Energy Lett. 11 (2026) 1688–1695. https://doi.org/10.1021/acsenergylett.5c03124.
[106] C. Han, W. Shi, M. Huang, Q. Wang, J. Yang, J. Chen, R. Ding, X. Yin, Solvent Effects on the Catalyst Ink and Layer Microstructure for Anion Exchange Membrane Fuel Cells, ACS Appl. Mater. Interfaces 16 (2024) 4550–4560. https://doi.org/10.1021/acsami.3c14404.
[107] H.N. Anchan, N.S. Bhat, N. Vinod, P.S. Prabhakar, S. Dutta, Catalytic conversion of glucose and its biopolymers into renewable compounds by inducing C–C bond scission and formation, Biomass Convers. Biorefin. 14 (2024) 9915–9948. https://doi.org/10.1007/s13399-022-03105-9.
[108] J. Cao, H. Zhuang, M. Guo, H. Wang, J. Xu, Z. Chen, Facile preparation of mesoporous graphenes by the sacrificial template approach for direct methanol fuel cell application, J. Mater. Chem. A 2 (2014) 19914–19919. https://doi.org/10.1039/C4TA05100A.
[109] C. Hu, Y. Zhou, R. Ma, Q. Liu, J. Wang, Reactive template synthesis of nitrogen-doped graphene-like carbon nanosheets derived from hydroxypropyl methyl-cellulose and dicyandiamide as efficient oxygen reduction electrocatalysts, J. Power Sources 345 (2017) 120–130. https://doi.org/10.1016/j.jpowsour.2017.01.124.
[110] M. Thommes, K. Kaneko, A.V. Neimark, J.P. Olivier, F. Rodriguez-Reinoso, J. Rouquerol, K.S.W. Sing, Physisorption of gases, with special reference to the

evaluation of surface area and pore size distribution (IUPAC Technical Report), Pure Appl. Chem. 87 (2015) 1051–1069. https://doi.org/10.1515/pac-2014-1117.
[111] J.F. Carneiro, M.J. Paulo, M. Siaj, A.C. Tavares, M.R.V. Lanza, Zirconia on Reduced Graphene Oxide Sheets: Synergistic Catalyst with High Selectivity for H_2O_2 Electrogeneration, ChemElectroChem 4 (2017) 508–513. https://doi.org/10.1002/celc.201600760.
[112] A. Sadezky, H. Muckenhuber, H. Grothe, R. Niessner, U. Pöschl, Raman micro-spectroscopy of soot and related carbonaceous materials: Spectral analysis and structural information, Carbon 43 (2005) 1731–1742. https://doi.org/10.1016/j.carbon.2005.02.018.
[113] H. Meng, B. Wu, D. Zhang, X. Zhu, S. Luo, Y. You, K. Chen, J. Long, J. Zhu, L. Liu, S. Xi, T. Petit, D. Wang, X.-M. Zhang, Z.J. Xu, L. Mai, Optimizing electronic synergy of atomically dispersed dual-metal Ni–N_4 and Fe–N_4 sites with adjacent Fe nanoclusters for high-efficiency oxygen electrocatalysis, Energy Environ. Sci. 17 (2024) 704–716. https://doi.org/10.1039/D3EE03383J.
[114] K. Artyushkova, A. Serov, S. Rojas-Carbonell, P. Atanassov, Chemistry of Multi-tudinous Active Sites for Oxygen Reduction Reaction in Transition Metal–Nitrogen–Carbon Electrocatalysts, J. Phys. Chem. C 119 (2015) 25917–25928. https://doi.org/10.1021/acs.jpcc.5b07653.
[115] D. Deng, L. Yu, X. Chen, G. Wang, L. Jin, X. Pan, J. Deng, G. Sun, X. Bao, Iron Encapsulated within Pod-like Carbon Nanotubes for Oxygen Reduction Reaction, Angew. Chem. Int. Ed. 52 (2013) 371–375. https://doi.org/10.1002/anie.201204958.
[116] G. Zuccante, M. Acciarri, C. Lo Vecchio, I. Gatto, V. Baglio, N. Pianta, R. Ruffo, L. Navarini, C. Santoro, Oxygen reduction reaction platinum group metal-free electrocatalysts derived from spent coffee grounds, Electrochim. Acta 492 (2024) 144353. https://doi.org/10.1016/j.electacta.2024.144353.
[117] T. Mineva, I. Matanovic, P. Atanassov, M.-T. Sougrati, L. Stievano, M. Clémancey, A. Kochem, J.-M. Latour, F. Jaouen, Understanding Active Sites in Pyrolyzed Fe–N–C Catalysts for Fuel Cell Cathodes by Bridging Density Functional Theory Calculations and ^{57} Fe Mössbauer Spectroscopy, ACS Catal. 9 (2019) 9359–9371. https://doi.org/10.1021/acscatal.9b02586.
[118] U. Tylus, Q. Jia, K. Strickland, N. Ramaswamy, A. Serov, P. Atanassov, S. Mukerjee, Elucidating Oxygen Reduction Active Sites in Pyrolyzed Metal–Nitrogen Coordinated Non-Precious-Metal Electrocatalyst Systems, J. Phys. Chem. C 118 (2014) 8999–9008. https://doi.org/10.1021/jp500781v.
[119] F. Pan, A. Liang, Y. Duan, Q. Liu, J. Zhang, Y. Li, Self-growth-templating synthesis of 3D N,P,Co-doped mesoporous carbon frameworks for efficient bifunctional oxygen and carbon dioxide electroreduction, J. Mater. Chem. A 5 (2017) 13104–13111. https://doi.org/10.1039/C7TA03005C.
[120] L. Lin, Q. Zhu, A.-W. Xu, Noble-Metal-Free Fe–N/C Catalyst for Highly Efficient Oxygen Reduction Reaction under Both Alkaline and Acidic Conditions, J. Am. Chem. Soc. 136 (2014) 11027–11033. https://doi.org/10.1021/ja504696r.
[121] Q. Zhou, L. Zhao, X. Sui, X. Gong, J. Li, X. Li, Z. Wang, Cobalt and Nitrogen Codoped Carbon Nanosheets Templated from NaCl as Efficient Oxygen Reduction Electrocatalysts, Chem. Asian J. 13 (2018) 3057–3062. https://doi.org/10.1002/asia.201801134.

[122] T.K. Mukhopadhyay, L. Leherte, A. Datta, Molecular Mechanism for the Self-Supported Synthesis of Graphitic Carbon Nitride from Urea Pyrolysis, J. Phys. Chem. Lett. 12 (2021) 1396–1406. https://doi.org/10.1021/acs.jpclett.0c03559.
[123] R. Sgarbi, K. Kumar, F. Jaouen, A. Zitolo, E.A. Ticianelli, F. Maillard, Oxygen reduction reaction mechanism and kinetics on M-NxCy and M@N-C active sites present in model M-N-C catalysts under alkaline and acidic conditions, J. Solid State Electrochem. 25 (2021) 45–56. https://doi.org/10.1007/s10008-019-04436-w.
[124] W.-J. Jiang, L. Gu, L. Li, Y. Zhang, X. Zhang, L.-J. Zhang, J.-Q. Wang, J.-S. Hu, Z. Wei, L.-J. Wan, Understanding the High Activity of Fe–N–C Electrocatalysts in Oxygen Reduction: Fe/Fe_3C Nanoparticles Boost the Activity of Fe–N_x , J. Am. Chem. Soc. 138 (2016) 3570–3578. https://doi.org/10.1021/jacs.6b00757.
[125] M.A. Ud Din, M. Idrees, S. Jamil, S. Irfan, G. Nazir, M.A. Mudassir, M.S. Saleem, S. Batool, N. Cheng, R. Saidur, Advances and challenges of methanol-tolerant oxygen reduction reaction electrocatalysts for the direct methanol fuel cell, J. Energy Chem. 77 (2023) 499–513. https://doi.org/10.1016/j.jechem.2022.11.023.
[126] B. Zhang, R. Chen, Z. Yang, Y. Chen, L. Zhou, Y. Yuan, Rapeseed meal-based autochthonous N and S-doped non-metallic porous carbon electrode material for oxygen reduction reaction catalysis, Int. J. Hydrogen Energy 46 (2021) 508–517. https://doi.org/10.1016/j.ijhydene.2020.09.198.
[127] K. Kisand, A. Sarapuu, D. Danilian, A. Kikas, V. Kisand, M. Rähn, A. Treshchalov, M. Käärik, M. Merisalu, P. Paiste, J. Aruväli, J. Leis, V. Sammelselg, S. Holdcroft, K. Tammeveski, Transition metal-containing nitrogen-doped nanocarbon catalysts derived from 5-methylresorcinol for anion exchange membrane fuel cell application, J. Colloid Interface Sci. 584 (2021) 263–274. https://doi.org/10.1016/j.jcis.2020.09.114.
[128] J. Lilloja, E. Kibena-Põldsepp, A. Sarapuu, J.C. Douglin, M. Käärik, J. Kozlova, P. Paiste, A. Kikas, J. Aruväli, J. Leis, V. Sammelselg, D.R. Dekel, K. Tammeveski, Transition-Metal- and Nitrogen-Doped Carbide-Derived Carbon/Carbon Nanotube Composites as Cathode Catalysts for Anion-Exchange Membrane Fuel Cells, ACS Catal. 11 (2021) 1920–1931. https://doi.org/10.1021/acscatal.0c03511.
[129] J. Wu, A. Mehmood, G. Zhang, S. Wu, G. Ali, A. Kucernak, Highly Selective O_2 Reduction to H_2O_2 Catalyzed by Cobalt Nanoparticles Supported on Nitrogen-Doped Carbon in Alkaline Solution, ACS Catal. 11 (2021) 5035–5046. https://doi.org/10.1021/acscatal.0c05701.
[130] K. Strickland, E. Miner, Q. Jia, U. Tylus, N. Ramaswamy, W. Liang, M.-T. Sougrati, F. Jaouen, S. Mukerjee, Highly active oxygen reduction non-platinum group metal electrocatalyst without direct metal–nitrogen coordination, Nat. Commun. 6 (2015) 7343. https://doi.org/10.1038/ncomms8343.
[131] Y. Lin, L. Yang, Y. Zhang, H. Jiang, Z. Xiao, C. Wu, G. Zhang, J. Jiang, L. Song, Defective Carbon–CoP Nanoparticles Hybrids with Interfacial Charges Polarization for Efficient Bifunctional Oxygen Electrocatalysis, Adv. Energy Mater. 8 (2018) 1703623. https://doi.org/10.1002/aenm.201703623.
[132] S.H. Ahn, A. Manthiram, Cobalt Phosphide Coupled with Heteroatom-Doped Nanocarbon Hybrid Electroctalysts for Efficient, Long-Life Rechargeable Zinc–Air Batteries, Small 13 (2017) 1702068. https://doi.org/10.1002/smll.201702068.
[133] K. Hu, Z. Xiao, Y. Cheng, D. Yan, R. Chen, J. Huo, S. Wang, Iron phosphide/N, P-doped carbon nanosheets as highly efficient electrocatalysts for oxygen reduction

reaction over the whole pH range, Electrochim. Acta 254 (2017) 280–286. https://doi.org/10.1016/j.electacta.2017.09.131.
[134] X. Xu, C. Shi, R. Chen, T. Chen, Iron phosphide nanocrystals decorated in situ on heteroatom-doped mesoporous carbon nanosheets used for an efficient oxygen reduction reaction in both alkaline and acidic media, RSC Adv. 7 (2017) 22263–22269. https://doi.org/10.1039/C7RA02349A.
[135] Y. Wu, Z. Xiao, Z. Jin, X. Li, Y. Chen, The cobalt carbide/bimetallic CoFe phosphide dispersed on carbon nanospheres as advanced bifunctional electrocatalysts for the ORR, OER, and rechargeable Zn–air batteries, J. Colloid Interface Sci. 590 (2021) 321–329. https://doi.org/10.1016/j.jcis.2021.01.055.
[136] M. Sevilla, C. Sanchís, T. Valdés-Solís, E. Morallón, A.B. Fuertes, Synthesis of Graphitic Carbon Nanostructures from Sawdust and Their Application as Electrocatalyst Supports, J. Phys. Chem. C 111 (2007) 9749–9756. https://doi.org/10.1021/jp072246x.
[137] J. Hyun, H.-T. Kim, Powering the hydrogen future: current status and challenges of anion exchange membrane fuel cells, Energy Environ. Sci. 16 (2023) 5633–5662. https://doi.org/10.1039/D3EE01768K.
[138] J. Lilloja, E. Kibena-Põldsepp, A. Sarapuu, A. Konovalova, M. Käärik, J. Kozlova, P. Paiste, A. Kikas, A. Treshchalov, J. Aruväli, A. Zitolo, J. Leis, A. Tamm, V. Kisand, S. Holdcroft, K. Tammeveski, Transition-Metal and Nitrogen-Doped Carbon Nanotube/Graphene Composites as Cathode Catalysts for Anion-Exchange Membrane Fuel Cells, ACS Appl. Energy Mater. 6 (2023) 5519–5529. https://doi.org/10.1021/acsaem.3c00613.
[139] C. Zhu, M. Takata, Y. Aoki, H. Habazaki, Nitrogen-doped porous carbon as-mediated by a facile solution combustion synthesis for supercapacitor and oxygen reduction electrocatalyst, Chem. Eng. J. 350 (2018) 278–289. https://doi.org/10.1016/j.cej.2018.06.001.
[140] T. Morishita, T. Tsumura, M. Toyoda, J. Przepiórski, A.W. Morawski, H. Konno, M. Inagaki, A review of the control of pore structure in MgO-templated nanoporous carbons, Carbon 48 (2010) 2690–2707. https://doi.org/10.1016/j.carbon.2010.03.064.
[141] Y. Wang, S. Zuo, J. Yang, S.-H. Yoon, Evolution of Phosphorus-Containing Groups on Activated Carbons during Heat Treatment, Langmuir 33 (2017) 3112–3122. https://doi.org/10.1021/acs.langmuir.7b00095.
[142] X. Zhan, X. Tong, M. Gu, J. Tian, Z. Gao, L. Ma, Y. Xie, Z. Chen, H. Ranganathan, G. Zhang, S. Sun, Phosphorus-Doped Graphene Electrocatalysts for Oxygen Reduction Reaction, Nanomaterials 12 (2022) 1141. https://doi.org/10.3390/nano12071141.
[143] W.E. Mustain, M. Chatenet, M. Page, Y.S. Kim, Durability challenges of anion exchange membrane fuel cells, Energy Environ. Sci. 13 (2020) 2805–2838. https://doi.org/10.1039/D0EE01133A.
[144] S. Rathinavel, K. Priyadharshini, D. Panda, A review on carbon nanotube: An overview of synthesis, properties, functionalization, characterization, and the application, Mater. Sci. Eng. B 268 (2021) 115095. https://doi.org/10.1016/j.mseb.2021.115095.
[145] L. Wu, J. Liu, B.R. Reddy, J. Zhou, Preparation of coal-based carbon nanotubes using catalytical pyrolysis: A brief review, Fuel Process. Technol. 229 (2022) 107171. https://doi.org/10.1016/j.fuproc.2022.107171.

[146] J. Zhao, Y. Liu, X. Quan, S. Chen, H. Yu, H. Zhao, Nitrogen-doped carbon with a high degree of graphitization derived from biomass as high-performance electrocatalyst for oxygen reduction reaction, Appl. Surf. Sci. 396 (2017) 986–993. https://doi.org/10.1016/j.apsusc.2016.11.073.
[147] I. Childres, L.A. Jauregui, J. Tian, Y.P. Chen, Effect of oxygen plasma etching on graphene studied using Raman spectroscopy and electronic transport measurements, New J. Phys. 13 (2011) 025008. https://doi.org/10.1088/1367-2630/13/2/025008.
[148] Z. Li, X. Zhong, L. Gao, J. Hu, W. Peng, X. Wang, G. Zhou, B. Xu, Asymmetric Coordination of Bimetallic Fe–Co Single-Atom Pairs toward Enhanced Bifunctional Activity for Rechargeable Zinc–Air Batteries, ACS Nano 18 (2024) 13006–13018. https://doi.org/10.1021/acsnano.4c01342.
[149] V. Vij, S. Sultan, A.M. Harzandi, A. Meena, J.N. Tiwari, W.-G. Lee, T. Yoon, K.S. Kim, Nickel-Based Electrocatalysts for Energy-Related Applications: Oxygen Reduction, Oxygen Evolution, and Hydrogen Evolution Reactions, ACS Catal. 7 (2017) 7196–7225. https://doi.org/10.1021/acscatal.7b01800.
[150] X. Zhang, J. Wang, C. Dai, X. Jin, Y. Zhao, L. Qu, Binary active sites of nickel–iron alloy bonded in nitrogen-doped carbon nanocage for robust durability and low polarization zinc-air batteries, J. Power Sources 538 (2022) 231563. https://doi.org/10.1016/j.jpowsour.2022.231563.
[151] X. Xie, L. Du, L. Yan, S. Park, Y. Qiu, J. Sokolowski, W. Wang, Y. Shao, Oxygen Evolution Reaction in Alkaline Environment: Material Challenges and Solutions, Adv. Funct. Mater. 32 (2022) 2110036. https://doi.org/10.1002/adfm.202110036.
[152] M. Labbe, M.P. Clark, K. Cadien, D.G. Ivey, Bifunctional Mn-Fe Oxide Catalysts for Zn-Air Battery Air Electrodes Fabricated Through Atomic Layer Deposition, Batter. Supercaps (2024). https://doi.org/10.1002/batt.202400133.
[153] M.-I. Jamesh, P. Moni, A.S. Prakash, M. Harb, ORR/OER activity and zinc-air battery performance of various kinds of graphene-based air catalysts, Mater. Sci. Energy Technol. 4 (2021) 1–22. https://doi.org/10.1016/j.mset.2020.12.001.
[154] M.M. Hantel, M.J. Armstrong, F. DaRosa, R. l'Abee, Characterization of Tortuosity in Polyetherimide Membranes Based on Gurley and Electrochemical Impedance Spectroscopy, J. Electrochem. Soc. 164 (2017) A334–A339. https://doi.org/10.1149/2.1071702jes.
[155] D. Dong, T. Wang, Y. Sun, J. Fan, Y.-C. Lu, Hydrotropic solubilization of zinc acetates for sustainable aqueous battery electrolytes, Nat. Sustain. 6 (2023) 1474–1484. https://doi.org/10.1038/s41893-023-01172-y.
[156] A.G. Briggs, N.A. Hampson, A. Marshall, Concentrated potassium zincate solutions studied using laser Raman spectroscopy and potentiometry, J. Chem. Soc., Faraday Trans. 2 70 (1974) 1978–1990. https://doi.org/10.1039/f29747001978.
[157] M. Mooste, Z. Ahmed, P. Kapitulskis, R. Ivanov, A. Treshchalov, H.-M. Piirsoo, A. Kikas, V. Kisand, K. Kukli, I. Hussainova, K. Tammeveski, Bifunctional oxygen electrocatalyst based on Fe, Co, and nitrogen co-doped graphene-coated alumina nanofibers for Zn-air battery air electrode, Appl. Surf. Sci. 660 (2024) 160024. https://doi.org/10.1016/j.apsusc.2024.160024.
[158] K. Muuli, R. Kumar, M. Mooste, V. Gudkova, A. Treshchalov, H.-M. Piirsoo, A. Kikas, J. Aruväli, V. Kisand, A. Tamm, A. Krumme, P. Moni, M. Wilhelm, K. Tammeveski, Iron, Cobalt, and Nickel Phthalocyanine Tri-Doped Electrospun

Carbon Nanofibre-Based Catalyst for Rechargeable Zinc–Air Battery Air Electrode, Materials 16 (2023) 4626. https://doi.org/10.3390/ma16134626.
[159] J. Zhang, Q. Zhou, Y. Tang, L. Zhang, Y. Li, Zinc–air batteries: are they ready for prime time?, Chem. Sci. 10 (2019) 8924–8929. https://doi.org/10.1039/C9SC04221K.
[160] Y. He, W. Shang, M. Ni, Y. Huang, H. Zhao, P. Tan, In-situ observation of the gas evolution process on the air electrode of Zn-air batteries during charging, J. Chem. Eng. 427 (2022) 130862. https://doi.org/10.1016/j.cej.2021.130862.
[161] C. Zhang, G. Zhang, H. Li, Y. Chang, Z. Chang, J. Liu, X. Sun, Interfacial dehalogenation-enabled hollow N-doped carbon network as bifunctional catalysts for rechargeable Zn-air battery, Electrochim. Acta 247 (2017) 1044–1051. https://doi.org/10.1016/j.electacta.2017.07.099.
[162] E. Davari, A.D. Johnson, A. Mittal, M. Xiong, D.G. Ivey, Manganese-cobalt mixed oxide film as a bifunctional catalyst for rechargeable zinc-air batteries, Electrochim. Acta 211 (2016) 735–743. https://doi.org/10.1016/j.electacta.2016.06.085.
[163] M. Wu, Y. Wang, Z. Wei, L. Wang, M. Zhuo, J. Zhang, X. Han, J. Ma, Ternary doped porous carbon nanofibers with excellent ORR and OER performance for zinc–air batteries, J. Mater. Chem. A 6 (2018) 10918–10925. https://doi.org/10.1039/C8TA02416B.
[164] K. Kisand, A. Sarapuu, J.C. Douglin, A. Kikas, M. Käärik, J. Kozlova, J. Aruväli, A. Treshchalov, J. Leis, V. Kisand, K. Kukli, D.R. Dekel, K. Tammeveski, Hierarchically Porous Fe−N−C Single-Atom Catalysts via Ionothermal Synthesis for Oxygen Reduction Reaction, ChemSusChem 18 (2025) e202401332. https://doi.org/10.1002/cssc.202401332.
[165] F.O. Ibrahim, K. Kisand, J.C. Douglin, A. Sarapuu, A. Kikas, M. Käärik, J. Kozlova, J. Aruväli, A. Treshchalov, J. Leis, V. Kisand, K. Kukli, K. Yassin, D.R. Dekel, K. Tammeveski, Ionothermal synthesis of mesoporous FeNC electro-catalysts for high-performance anion-exchange membrane fuel cells, Chem. Eng. J. 510 (2025) 161560. https://doi.org/10.1016/j.cej.2025.161560.
[166] M. Zhang, X. Chen, H. Dong, A study on multistep thermal decomposition behavior and kinetics of magnesium nitrate hydrate, Thermochim. Acta 701 (2021) 178951. https://doi.org/10.1016/j.tca.2021.178951.
[167] Y.P. Zhu, C. Guo, Y. Zheng, S.-Z. Qiao, Surface and Interface Engineering of Noble-Metal-Free Electrocatalysts for Efficient Energy Conversion Processes, Acc. Chem. Res. 50 (2017) 915–923. https://doi.org/10.1021/acs.accounts.6b00635.
[168] S. Liu, Z. Li, C. Wang, W. Tao, M. Huang, M. Zuo, Y. Yang, K. Yang, L. Zhang, S. Chen, P. Xu, Q. Chen, Turning main-group element magnesium into a highly active electrocatalyst for oxygen reduction reaction, Nat. Commun. 11 (2020) 938. https://doi.org/10.1038/s41467-020-14565-w.
[169] R.D. Hunter, J. Ramírez-Rico, Z. Schnepp, Iron-catalyzed graphitization for the synthesis of nanostructured graphitic carbons, J. Mater. Chem. A 10 (2022) 4489–4516. https://doi.org/10.1039/D1TA09654K.
[170] O.Y. Bisen, K.K. Nanda, Alkaline earth metal based single atom catalyst for the highly durable oxygen reduction reaction, Appl. Mater. Today 21 (2020) 100846. https://doi.org/10.1016/j.apmt.2020.100846.
[171] Z. Zhu, H. Yin, Y. Wang, C. Chuang, L. Xing, M. Dong, Y. Lu, G. Casillas-Garcia, Y. Zheng, S. Chen, Y. Dou, P. Liu, Q. Cheng, H. Zhao, Coexisting Single-Atomic

Fe and Ni Sites on Hierarchically Ordered Porous Carbon as a Highly Efficient ORR Electrocatalyst, Adv. Mater. 32 (2020) 2004670. https://doi.org/10.1002/adma.202004670.
[172] Y.-P. Ku, K. Ehelebe, A. Hutzler, M. Bierling, T. Böhm, A. Zitolo, M. Vorokhta, N. Bibent, F.D. Speck, D. Seeberger, I. Khalakhan, K.J.J. Mayrhofer, S. Thiele, F. Jaouen, S. Cherevko, Oxygen Reduction Reaction in Alkaline Media Causes Iron Leaching from Fe–N–C Electrocatalysts, J. Am. Chem. Soc. 144 (2022) 9753–9763. https://doi.org/10.1021/jacs.2c02088.
[173] L. Li, X. Tang, B. Wu, B. Huang, K. Yuan, Y. Chen, Advanced Architectures of Air Electrodes in Zinc–Air Batteries and Hydrogen Fuel Cells, Adv. Mater. 36 (2024) 2308326. https://doi.org/10.1002/adma.202308326.
[174] K. Chuluunbandi, S. Thiele, A.T.S. Freiberg, Comparison of Different Ionomers for the Anode Catalyst Layer of Anion Exchange Membrane Water Electrolysis, ECS Meeting Abstracts MA2024-02 (2024) 3148–3148. https://doi.org/10.1149/MA2024-02453148mtgabs.
[175] L. Xia, M. Ni, Q. Xu, H. Xu, K. Zheng, Optimization of catalyst layer thickness for achieving high performance and low cost of high temperature proton exchange membrane fuel cell, Appl. Energy 294 (2021) 117012. https://doi.org/10.1016/j.apenergy.2021.117012.
[176] J. Zhang, W. Zhu, T. Huang, C. Zheng, Y. Pei, G. Shen, Z. Nie, D. Xiao, Y. Yin, M.D. Guiver, Recent Insights on Catalyst Layers for Anion Exchange Membrane Fuel Cells, Adv. Sci. 8 (2021) 2100284. https://doi.org/10.1002/advs.202100284.
[177] K. Muuli, X. Lyu, M. Mooste, M. Käärik, B. Zulevi, J. Leis, H. Yu, D.A. Cullen, A. Serov, K. Tammeveski, Outstanding platinum group metal-free bifunctional catalysts for rechargeable zinc-air batteries, Electrochim. Acta 446 (2023) 142126. https://doi.org/10.1016/j.electacta.2023.142126.
[178] Y. Kumar, E. Kibena-Põldsepp, M. Mooste, J. Kozlova, A. Kikas, J. Aruväli, M. Käärik, V. Kisand, J. Leis, A. Tamm, S. Holdcroft, J.H. Zagal, K. Tammeveski, Iron and Nickel Phthalocyanine-Modified Nanocarbon Materials as Cathode Catalysts for Anion-Exchange Membrane Fuel Cells and Zinc-Air Batteries, ChemElectroChem 9 (2022) e202200717. https://doi.org/10.1002/celc.202200717.
[179] T. Wang, M. Kunimoto, T. Mori, M. Yanagisawa, J. Niikura, I. Takahashi, M. Morita, T. Abe, T. Homma, Carbonate formation on carbon electrode in rechargeable zinc-air battery revealed by in-situ Raman measurements, J. Power Sources 533 (2022) 231237. https://doi.org/10.1016/j.jpowsour.2022.231237.
[180] S. Möller, S. Barwe, J. Masa, D. Wintrich, S. Seisel, H. Baltruschat, W. Schuhmann, Online Monitoring of Electrochemical Carbon Corrosion in Alkaline Electrolytes by Differential Electrochemical Mass Spectrometry, Angew. Chem. Int. Ed. 59 (2020) 1585–1589. https://doi.org/10.1002/anie.201909475.
[181] Y. Guo, M. Massen-Hane, G. Endy, T.A. Hatton, Porous Polymeric Electrodes for Electrochemical Carbon Dioxide Capture, Adv. Mater. 36 (2024) 2407567. https://doi.org/10.1002/adma.202407567.
[182] H. Rabiee, B. Ma, Y. Yang, F. Li, P. Yan, Y. Wu, X. Zhang, S. Hu, H. Wang, L. Ge, Z. Zhu, Advances and Challenges of Carbon-Free Gas-Diffusion Electrodes (GDEs) for Electrochemical CO_2 Reduction, Adv. Funct. Mater. 35 (2025) 2411195. https://doi.org/10.1002/adfm.202411195.
[183] G. Yang, J. Zhu, P. Yuan, Y. Hu, G. Qu, B.-A. Lu, X. Xue, H. Yin, W. Cheng, J. Cheng, W. Xu, J. Li, J. Hu, S. Mu, J.-N. Zhang, Regulating Fe-spin state by atomically dispersed Mn-N in Fe-N-C catalysts with high oxygen reduction

activity, Nat. Commun. 12 (2021) 1734. https://doi.org/10.1038/s41467-021-21919-5.
[184] Z. Chen, X. Liao, C. Sun, K. Zhao, D. Ye, J. Li, G. Wu, J. Fang, H. Zhao, J. Zhang, Enhanced performance of atomically dispersed dual-site Fe-Mn electrocatalysts through cascade reaction mechanism, Appl. Catal. B 288 (2021) 120021. https://doi.org/10.1016/j.apcatb.2021.120021.
[185] J. Liu, M. Secanell, Exploring the impact of ionomer content and distribution on inkjet printed cathodes for anion exchange membrane fuel cells, Electrochim. Acta 509 (2025) 145293. https://doi.org/10.1016/j.electacta.2024.145293.
[186] Y. Zhou, H. Yu, F. Xie, Y. Zhao, X. Sun, D. Yao, G. Jiang, J. Geng, Z. Shao, Improving cell performance for anion exchange membrane fuel cells with FeNC cathode by optimizing ionomer content, Int. J. Hydrogen Energy 48 (2023) 5266–5275. https://doi.org/10.1016/j.ijhydene.2022.11.057.
[187] N. Ul Hassan, M. Mandal, G. Huang, H.A. Firouzjaie, P.A. Kohl, W.E. Mustain, Achieving High-Performance and 2000 h Stability in Anion Exchange Membrane Fuel Cells by Manipulating Ionomer Properties and Electrode Optimization, Adv. Energy Mater. 10 (2020) 2001986. https://doi.org/10.1002/aenm.202001986.

9. SUMMARY IN ESTONIAN

Biomassist saadud süsinikul põhinevad mitteväärismetallkatalüsaatorid elektrokatalüütilisteks rakendusteks

Doktoritöö eesmärk oli arendada ja iseloomustada väärismetallivabu elektrokatalüsaatoreid hapniku elektrokeemilise redutseerumisreaktsiooni ja eraldumisreaktsiooni jaoks, mida võiks rakendada anioonivahetusmembraaniga kütuseelemendis ja metall-õhk-akudes. Nanostruktuursetel süsinikmaterjalidel põhinevad katalüsaatorid valmistati kõrgtemperatuurse pürolüüsi teel, kasutades süsiniku lähteainena glükoosi ja rapsiõli tootmisjääki – kuumpressitud rapsikooki. Saadud katalüsaatormaterjale uuriti erinevate füüsikalis-keemiliste ja elektrokeemiliste analüüsimeetoditega, et leida seoseid nende struktuuri, koostise ja elektrokatalüütilise aktiivsuse vahel.

Töö esimeses osas kasutati materjalide sünteesil süsinikuallikana glükoosi, millele lisati erinevates kogustes raua soola, lämmastikuallikat ning matriitsina naatriumkloriidi [I]. Leiti, et katalüsaatorite aktiivsus hapniku redutseerumisel sõltus nende metallisisaldusest ja pürolüüsitemperatuurist, kuid oli siiski madalam kui 20% Pt/C võrdlusmaterjalil.

Järgnevates töödes kasutati glükoosi asemel süsiniku lähteainena rapsikooki. Sünteesiprotseduur jäi esialgu samaks, kuid tahket NaCl matriitsi pürolüüsi käigus ei lisatud ning lisaks rauda sisaldavatele materjalidele valmistati ka koobaltit sisaldavad ning bimetalsed katalüsaatorid [II]. Saadud materjalid olid hapniku redutseerumisel oluliselt aktiivsemad kui glükoosist valmistatud katalüsaatorid. Lisaks uuriti happetöötluse mõju katalüsaatoritele ning leiti, et see suurendas oluliselt nende eripinda ja mõnevõrra ka elektrokatalüütilist aktiivsust. Parima katalüsaatori FeCoNCR-a kasutamisel anioonivahetusmembraaniga kütuseelemendis saavutati üsna tagasihoidlik maksimaalne võimsustihedus P_{max} = 131 mW cm^{-2}. Seetõttu optimeeriti järgmises töös katalüsaatori poorsust, kasutades sünteesiprotsessis magneesiumatsetaati, mis laguneb pürolüüsi käigus, moodustades magneesiumoksiidi ja magneesiumtsüaanamiidi nanoosakesed [III]. Need toimivad tahke matriitsina, mis eemaldatakse happetöötluse käigus, tekitades materjalides poorse struktuuri. Optimeeritud materjali pooride ruumala suurenes võrreldes ilma matriitsita valmistatud materjaliga peaaegu 50% ning eripind ligikaudu 20%. Selle tulemusena paranes ka katalüsaatorite aktiivsus hapniku redutseerumisel, olles võrreldav 20% Pt/C katalüsaatoriga. FeNCR-MgAc-3-1 katoodiga saavutati anioonivahetusmembraaniga kütuseelemendis oluliselt kõrgem maksimaalne võimsustihedus (P_{max} = 355 mW cm^{-2}).

Kuna see sünteesimeetod osutus edukaks, kasutati seda ka tsink-õhk-aku õhuelektroodil rakendatavate rauda ja niklit sisaldavate bifunktsionaalsete katalüsaatorite valmistamiseks [IV]. Optimaalse metallisisaldusega materjal 4Fe4NiNCR oli kõrge bifunktsionaalse aktiivsusega hapniku redutseerumis- ja eraldumisreaktsioonil. Selle materjali kasutamisel tsink-õhk-aku õhuelektroodina saavutati

kõrge maksimaalne võimsustihedus P_{max}= 202 mW cm^{-2} ning aku oli laadimisel stabiilne 68 tunni (68 tsükli) jooksul. Lisaks leiti, et tsinkelektroodi ja õhuelektroodi pindalade suhtel on suur mõju maksimaalsele võimsustihedusele.

Töö viimases osas kasutati ionotermilist meetodit rapsikoogist mesopoorse süsiniku valmistamiseks, mida seejärel dopeeriti metallide ja lämmastikuga. Sel viisil sünteesiti bifunktsionaalsed rauda ja niklit sisaldavad katalüsaatorid, varieerides raua ja nikli massisuhet [V]. Leiti, et katalüsaatorite hapniku redutseerumise aktiivsus vähenes suhtelise rauasisalduse vähenedes, kuid hapniku eraldumisreaktsiooni aktiivsus jäi peaaegu muutumatuks. Materjali FeNiPhenIC kasutamisel tsink-õhk-akus õhuelektroodina saavutati maksimaalne võimsustihedus P_{max} = 179 mW cm^{-2}, mis pärast materjali kuulveskis töötlemist suurenes väärtuseni P_{max} = 205 mW cm^{-2}. Lisaks püsis tsink-õhk-aku materjali 05Fe05NiPhenIC õhuelektroodina kasutades stabiilsena 65 tundi (33 tsüklit).

Järgnevalt rakendati sama meetodit rauda ja/või mangaani sisaldavate hapniku redutseerumisreaktsiooni katalüsaatormaterjalide valmistamiseks [VI]. Pöörleva ketaselektroodi mõõtmised näitasid, et saadud materjalid on aktiivsed hapniku redutseerumisel, ületades aktiivsuselt ka 20% Pt/C katalüsaatorit. Materjalide iseloomustamisel kasutati ka gaasidifusioonelektroodi, mis näitas, et materjalide aktiivsus võib praktilistes tingimustes erineda pöörleva ketaselektroodiga saadud tulemustest. Anioonivahetusmembraaniga kütuseelemendis saadi materjaliga FeIC P_{max} = 289 mW cm^{-2}, mis oli varasematest tulemustest [III] veidi madalam.

Doktoritöö tulemused näitavad, et biomassil põhinevast lähteainest on võimalik eri meetoditega valmistada aktiivseid väärismetallivabu elektrokatalüsaatoreid. Katalüsaatorite elektrokatalüütiline aktiivsus sõltub nende koostisest, pooride suurusjaotusest, eripinnast ja aktiivtsentrite loomusest. Optimaalsete omadustega katalüsaatoreid saab valmistada, valides sobivad sünteesitingimused, varieerides lähteainete massisuhet ning kasutades tahkeid matriitse ja järeltöötlust. Sobivalt disainitud mitteväärismetallkatalüsaatoritega saavutati 20% Pt/C katalüsaatoriga võrdväärne elektrokatalüütiline aktiivsus hapniku elektroredutseerumisel. Testides materjale reaalsetes süsteemides – anioonivahetusmembraaniga kütuseelemendis ja tsink-õhk-akus – saavutati kõrged võimsustiheduse väärtused, mis näitab, et biomassist valmistatud elektrokatalüsaatorid on perspektiivikas ja realistlik alternatiiv kallitele väärismetallkatalüsaatoritele elektrokeemilise energiatehnoloogia seadmete arendamisel.

10. ACKNOWLEDGEMENTS

First, I would like to thank my supervisors Associate Professor Ave Sarapuu and Professor Kaido Tammeveski for their dedicated attention in supervising my scientific work, which has had a notable positive impact on my personal growth as a scientist. I would like to thank all of my co-workers and fellow Junior Researchers at the University of Tartu, with whom I have had interesting discussions in all sorts of areas.

I would like to specifically thank Dr. Uno Mäeorg for introducing the rapeseed press cake material, which became an integral part of this thesis. Additionally, I would like to thank all of my co-authors who have contributed to my work over the years: Jaan Aruväli, Dr. Arvo Kikas, Dr. Sergei Vlassov, Prof. Vambola Kisand, Dr. Marek Mooste, Dr. Kaarel Kisand, Dr. Maike Käärik, Dr. Mati Kook, Dr. Aleksei Treštšalov, Dr. Jekaterina Kozlova, Dr. Jaan Leis, Dr. Aile Tamm and Prof. Kaupo Kukli.

This work was financially supported by the Estonian Research Council (grants PRG723, PRG2569), by the Estonian Ministry of Education and Research (TK210, Centre of Excellence in Sustainable Green Hydrogen and Energy Technologies) and by the EU through the European Regional Development Fund (TK141, "Advanced materials and high-technology devices for energy recuperation systems").

11. PUBLICATIONS

12. CURRICULUM VITAE

Name: Silver Juvanen
Date of birth: November 17, 1995
Citizenship: Estonian
Adress: Ravila 14a, 50411, Tartu, Eesti
E-mail: silver.juvanen@ut.ee

Education:

2022–…	University of Tartu, PhD (Chemistry)
2019–2021	University of Tartu, MSc (Chemistry)
2015–2018	University of Tartu, BSc (Chemistry)

Professional experience:

2022–…	University of Tartu, Junior Research Fellow

Scientific publications:

1. S. Juvanen, A. Sarapuu, S. Vlassov, M. Kook, V. Kisand, M. Käärik, A. Treshchalov, J. Aruväli, J. Kozlova, A. Tamm, J. Leis, K. Tammeveski, Iron-Containing Nitrogen-Doped Carbon Nanomaterials Prepared via NaCl Template as Efficient Electrocatalysts for the Oxygen Reduction Reaction. ChemElectroChem 8 (12) (2021) 2288–2297.
2. S. Juvanen, A. Sarapuu, M. Mooste, M. Käärik, U. Mäeorg, A. Kikas, V. Kisand, J. Kozlova, A. Treshchalov, J. Aruväli, J. Leis, A. Tamm, K. Tammeveski, Electroreduction of Oxygen on Iron- and Cobalt-Containing Nitrogen-Doped Carbon Catalysts Prepared from the Rapeseed Press Cake. J. Electroanal. Chem. 920 (2022) 116599.
3. S. Juvanen, A. Sarapuu, K. Kisand, M. Käärik, A. Kikas, J. Kozlova, A. Treshchalov, J. Aruväli, J. Leis, V. Kisand, K. Kukli, K. Tammeveski, Templated Rapeseed-Press-Cake-Based Materials as Efficient Oxygen Reduction Reaction Electrocatalysts. ACS Sustain. Resour. Manag. 2 (3) (2025) 446–454.
4. M. Mooste, R. Kumar, S. Juvanen, J. Kozlova, A. Kikas, A. Treshchalov, M. Käärik, J. Aruväli, J. Leis, V. Kisand, K. Kukli, D. Schonvogel, P. Wagner, M. Wilhelm, K. Tammeveski, K.A. Friedrich, Binary Transition Metal and Nitrogen Functionalised Silicon Oxycarbide Electrocatalysts for Zn–Air Battery Air Electrode Application. Int. J. Energy Res. 2025 (1) (2025) 4252866.
5. S. Juvanen, A. Sarapuu, M. Käärik, A. Kikas, J. Kozlova, A. Treshchalov, J. Aruväli, J. Leis, V. Kisand, K. Kukli, K. Tammeveski, Investigation of Rechargeable Zinc-Air Battery Performance Using a Bifunctional Biomass-Derived Catalyst Material for the Air Electrode. J. Energy Storage 148 (2026) 120293.

6. S. Juvanen, A. Sarapuu, M. Käärik, A. Kikas, J. Kozlova, A. Treshchalov, J. Aruväli, J. Leis, V. Kisand, K. Kukli, K. Tammeveski, Bifunctional Bimetallic Biomass-Derived Electrocatalyst Materials for Usage as Air Electrode Catalysts in Rechargeable Zinc-Air Batteries, Energy & Fuels 40 (20) (2026) 11116–11127.

13. ELULOOKIRJELDUS

Nimi: Silver Juvanen
Sünniaeg: 17. november 1995
Kodakondsus: Eesti
Aadress: Ravila 14a, 50411, Tartu, Eesti
E-post: silver.juvanen@ut.ee

Hariduskäik:

2022–…	Tartu Ülikool, doktorantuur (keemia)
2019–2021	Tartu Ülikool, MSc (keemia)
2015–2018	Tartu Ülikool, BSc (keemia)

Töökogemus:

2022–…	Tartu Ülikool, kolloid- ja keskkonnakeemia nooremteadur

Publikatsioonide loetelu:

1. S. Juvanen, A. Sarapuu, S. Vlassov, M. Kook, V. Kisand, M. Käärik, A. Treshchalov, J. Aruväli, J. Kozlova, A. Tamm, J. Leis, K. Tammeveski, Iron-Containing Nitrogen-Doped Carbon Nanomaterials Prepared via NaCl Template as Efficient Electrocatalysts for the Oxygen Reduction Reaction. ChemElectroChem 8 (12) (2021) 2288–2297.
2. S. Juvanen, A. Sarapuu, M. Mooste, M. Käärik, U. Mäeorg, A. Kikas, V. Kisand, J. Kozlova, A. Treshchalov, J. Aruväli, J. Leis, A. Tamm, K. Tammeveski, Electroreduction of Oxygen on Iron- and Cobalt-Containing Nitrogen-Doped Carbon Catalysts Prepared from the Rapeseed Press Cake. J. Electroanal. Chem. 920 (2022) 116599.
3. S. Juvanen, A. Sarapuu, K. Kisand, M. Käärik, A. Kikas, J. Kozlova, A. Treshchalov, J. Aruväli, J. Leis, V. Kisand, K. Kukli, K. Tammeveski, Templated Rapeseed-Press-Cake-Based Materials as Efficient Oxygen Reduction Reaction Electrocatalysts. ACS Sustain. Resour. Manag. 2 (3) (2025) 446–454.
4. M. Mooste, R. Kumar, S. Juvanen, J. Kozlova, A. Kikas, A. Treshchalov, M. Käärik, J. Aruväli, J. Leis, V. Kisand, K. Kukli, D. Schonvogel, P. Wagner, M. Wilhelm, K. Tammeveski, K.A. Friedrich, Binary Transition Metal and Nitrogen Functionalised Silicon Oxycarbide Electrocatalysts for Zn–Air Battery Air Electrode Application. Int. J. Energy Res. 2025 (1) (2025) 4252866.
5. S. Juvanen, A. Sarapuu, M. Käärik, A. Kikas, J. Kozlova, A. Treshchalov, J. Aruväli, J. Leis, V. Kisand, K. Kukli, K. Tammeveski, Investigation of Rechargeable Zinc-Air Battery Performance Using a Bifunctional Biomass-Derived Catalyst Material for the Air Electrode. J. Energy Storage 148 (2026) 120293.

6. S. Juvanen, A. Sarapuu, M. Käärik, A. Kikas, J. Kozlova, A. Treshchalov, J. Aruväli, J. Leis, V. Kisand, K. Kukli, K. Tammeveski, Bifunctional Bimetallic Biomass-Derived Electrocatalyst Materials for Usage as Air Electrode Catalysts in Rechargeable Zinc-Air Batteries, Energy & Fuels 40 (20) (2026) 11116–11127.

DISSERTATIONES CHIMICAE UNIVERSITATIS TARTUENSIS

1. **Toomas Tamm.** Quantum-chemical simulation of solvent effects. Tartu, 1993, 110 p.
2. **Peeter Burk.** Theoretical study of gas-phase acid-base equilibria. Tartu, 1994, 96 p.
3. **Victor Lobanov.** Quantitative structure-property relationships in large descriptor spaces. Tartu, 1995, 135 p.
4. **Vahur Mäemets.** The ^{17}O and ^{1}H nuclear magnetic resonance study of H_2O in individual solvents and its charged clusters in aqueous solutions of electrolytes. Tartu, 1997, 140 p.
5. **Andrus Metsala.** Microcanonical rate constant in nonequilibrium distribution of vibrational energy and in restricted intramolecular vibrational energy redistribution on the basis of slater's theory of unimolecular reactions. Tartu, 1997, 150 p.
6. **Uko Maran.** Quantum-mechanical study of potential energy surfaces in different environments. Tartu, 1997, 137 p.
7. **Alar Jänes.** Adsorption of organic compounds on antimony, bismuth and cadmium electrodes. Tartu, 1998, 219 p.
8. **Kaido Tammeveski.** Oxygen electroreduction on thin platinum films and the electrochemical detection of superoxide anion. Tartu, 1998, 139 p.
9. **Ivo Leito.** Studies of Brønsted acid-base equilibria in water and non-aqueous media. Tartu, 1998, 101 p.
10. **Jaan Leis.** Conformational dynamics and equilibria in amides. Tartu, 1998, 131 p.
11. **Toonika Rinken.** The modelling of amperometric biosensors based on oxidoreductases. Tartu, 2000, 108 p.
12. **Dmitri Panov.** Partially solvated Grignard reagents. Tartu, 2000, 64 p.
13. **Kaja Orupõld.** Treatment and analysis of phenolic wastewater with microorganisms. Tartu, 2000, 123 p.
14. **Jüri Ivask.** Ion Chromatographic determination of major anions and cations in polar ice core. Tartu, 2000, 85 p.
15. **Lauri Vares.** Stereoselective Synthesis of Tetrahydrofuran and Tetrahydropyran Derivatives by Use of Asymmetric Horner-Wadsworth-Emmons and Ring Closure Reactions. Tartu, 2000, 184 p.
16. **Martin Lepiku.** Kinetic aspects of dopamine D_2 receptor interactions with specific ligands. Tartu, 2000, 81 p.
17. **Katrin Sak.** Some aspects of ligand specificity of P2Y receptors. Tartu, 2000, 106 p.
18. **Vello Pällin.** The role of solvation in the formation of iotsitch complexes. Tartu, 2001, 95 p.
19. **Katrin Kollist.** Interactions between polycyclic aromatic compounds and humic substances. Tartu, 2001, 93 p.

20. **Ivar Koppel.** Quantum chemical study of acidity of strong and superstrong Brønsted acids. Tartu, 2001, 104 p.
21. **Viljar Pihl.** The study of the substituent and solvent effects on the acidity of OH and CH acids. Tartu, 2001, 132 p.
22. **Natalia Palm.** Specification of the minimum, sufficient and significant set of descriptors for general description of solvent effects. Tartu, 2001, 134 p.
23. **Sulev Sild.** QSPR/QSAR approaches for complex molecular systems. Tartu, 2001, 134 p.
24. **Ruslan Petrukhin.** Industrial applications of the quantitative structure-property relationships. Tartu, 2001, 162 p.
25. **Boris V. Rogovoy.** Synthesis of (benzotriazolyl)carboximidamides and their application in relations with *N*- and *S*-nucleophyles. Tartu, 2002, 84 p.
26. **Koit Herodes.** Solvent effects on UV-vis absorption spectra of some solvatochromic substances in binary solvent mixtures: the preferential solvation model. Tartu, 2002, 102 p.
27. **Anti Perkson.** Synthesis and characterisation of nanostructured carbon. Tartu, 2002, 152 p.
28. **Ivari Kaljurand.** Self-consistent acidity scales of neutral and cationic Brønsted acids in acetonitrile and tetrahydrofuran. Tartu, 2003, 108 p.
29. **Karmen Lust.** Adsorption of anions on bismuth single crystal electrodes. Tartu, 2003, 128 p.
30. **Mare Piirsalu.** Substituent, temperature and solvent effects on the alkaline hydrolysis of substituted phenyl and alkyl esters of benzoic acid. Tartu, 2003, 156 p.
31. **Meeri Sassian.** Reactions of partially solvated Grignard reagents. Tartu, 2003, 78 p.
32. **Tarmo Tamm.** Quantum chemical modelling of polypyrrole. Tartu, 2003. 100 p.
33. **Erik Teinemaa.** The environmental fate of the particulate matter and organic pollutants from an oil shale power plant. Tartu, 2003. 102 p.
34. **Jaana Tammiku-Taul.** Quantum chemical study of the properties of Grignard reagents. Tartu, 2003. 120 p.
35. **Andre Lomaka.** Biomedical applications of predictive computational chemistry. Tartu, 2003. 132 p.
36. **Kostyantyn Kirichenko.** Benzotriazole – Mediated Carbon–Carbon Bond Formation. Tartu, 2003. 132 p.
37. **Gunnar Nurk.** Adsorption kinetics of some organic compounds on bismuth single crystal electrodes. Tartu, 2003, 170 p.
38. **Mati Arulepp.** Electrochemical characteristics of porous carbon materials and electrical double layer capacitors. Tartu, 2003, 196 p.
39. **Dan Cornel Fara.** QSPR modeling of complexation and distribution of organic compounds. Tartu, 2004, 126 p.
40. **Riina Mahlapuu.** Signalling of galanin and amyloid precursor protein through adenylate cyclase. Tartu, 2004, 124 p.

41. **Mihkel Kerikmäe.** Some luminescent materials for dosimetric applications and physical research. Tartu, 2004, 143 p.
42. **Jaanus Kruusma.** Determination of some important trace metal ions in human blood. Tartu, 2004, 115 p.
43. **Urmas Johanson.** Investigations of the electrochemical properties of polypyrrole modified electrodes. Tartu, 2004, 91 p.
44. **Kaido Sillar.** Computational study of the acid sites in zeolite ZSM-5. Tartu, 2004, 80 p.
45. **Aldo Oras.** Kinetic aspects of dATPαS interaction with $P2Y_1$ receptor. Tartu, 2004, 75 p.
46. **Erik Mölder.** Measurement of the oxygen mass transfer through the air-water interface. Tartu, 2005, 73 p.
47. **Thomas Thomberg.** The kinetics of electroreduction of peroxodisulfate anion on cadmium (0001) single crystal electrode. Tartu, 2005, 95 p.
48. **Olavi Loog.** Aspects of condensations of carbonyl compounds and their imine analogues. Tartu, 2005, 83 p.
49. **Siim Salmar.** Effect of ultrasound on ester hydrolysis in aqueous ethanol. Tartu, 2006, 73 p.
50. **Ain Uustare.** Modulation of signal transduction of heptahelical receptors by other receptors and G proteins. Tartu, 2006, 121 p.
51. **Sergei Yurchenko.** Determination of some carcinogenic contaminants in food. Tartu, 2006, 143 p.
52. **Kaido Tämm.** QSPR modeling of some properties of organic compounds. Tartu, 2006, 67 p.
53. **Olga Tšubrik.** New methods in the synthesis of multisubstituted hydrazines. Tartu. 2006, 183 p.
54. **Lilli Sooväli.** Spectrophotometric measurements and their uncertainty in chemical analysis and dissociation constant measurements. Tartu, 2006, 125 p.
55. **Eve Koort.** Uncertainty estimation of potentiometrically measured ph and pK_a values. Tartu, 2006, 139 p.
56. **Sergei Kopanchuk.** Regulation of ligand binding to melanocortin receptor subtypes. Tartu, 2006, 119 p.
57. **Silvar Kallip.** Surface structure of some bismuth and antimony single crystal electrodes. Tartu, 2006, 107 p.
58. **Kristjan Saal.** Surface silanization and its application in biomolecule coupling. Tartu, 2006, 77 p.
59. **Tanel Tätte.** High viscosity $Sn(OBu)_4$ oligomeric concentrates and their applications in technology. Tartu, 2006, 91 p.
60. **Dimitar Atanasov Dobchev**. Robust QSAR methods for the prediction of properties from molecular structure. Tartu, 2006, 118 p.
61. **Hannes Hagu**. Impact of ultrasound on hydrophobic interactions in solutions. Tartu, 2007, 81 p.
62. **Rutha Jäger.** Electroreduction of peroxodisulfate anion on bismuth electrodes. Tartu, 2007, 142 p.

63. **Kaido Viht.** Immobilizable bisubstrate-analogue inhibitors of basophilic protein kinases: development and application in biosensors. Tartu, 2007, 88 p.
64. **Eva-Ingrid Rõõm.** Acid-base equilibria in nonpolar media. Tartu, 2007, 156 p.
65. **Sven Tamp.** DFT study of the cesium cation containing complexes relevant to the cesium cation binding by the humic acids. Tartu, 2007, 102 p.
66. **Jaak Nerut.** Electroreduction of hexacyanoferrate(III) anion on Cadmium (0001) single crystal electrode. Tartu, 2007, 180 p.
67. **Lauri Jalukse.** Measurement uncertainty estimation in amperometric dissolved oxygen concentration measurement. Tartu, 2007, 112 p.
68. **Aime Lust.** Charge state of dopants and ordered clusters formation in CaF_2:Mn and CaF_2:Eu luminophors. Tartu, 2007, 100 p.
69. **Iiris Kahn**. Quantitative Structure-Activity Relationships of environmentally relevant properties. Tartu, 2007, 98 p.
70. **Mari Reinik.** Nitrates, nitrites, N-nitrosamines and polycyclic aromatic hydrocarbons in food: analytical methods, occurrence and dietary intake. Tartu, 2007, 172 p.
71. **Heili Kasuk.** Thermodynamic parameters and adsorption kinetics of organic compounds forming the compact adsorption layer at Bi single crystal electrodes. Tartu, 2007, 212 p.
72. **Erki Enkvist.** Synthesis of adenosine-peptide conjugates for biological applications. Tartu, 2007, 114 p.
73. **Svetoslav Hristov Slavov**. Biomedical applications of the QSAR approach. Tartu, 2007, 146 p.
74. **Eneli Härk.** Electroreduction of complex cations on electrochemically polished Bi(*hkl*) single crystal electrodes. Tartu, 2008, 158 p.
75. **Priit Möller.** Electrochemical characteristics of some cathodes for medium temperature solid oxide fuel cells, synthesized by solid state reaction technique. Tartu, 2008, 90 p.
76. **Signe Viggor.** Impact of biochemical parameters of genetically different pseudomonads at the degradation of phenolic compounds. Tartu, 2008, 122 p.
77. **Ave Sarapuu.** Electrochemical reduction of oxygen on quinone-modified carbon electrodes and on thin films of platinum and gold. Tartu, 2008, 134 p.
78. **Agnes Kütt.** Studies of acid-base equilibria in non-aqueous media. Tartu, 2008, 198 p.
79. **Rouvim Kadis.** Evaluation of measurement uncertainty in analytical chemistry: related concepts and some points of misinterpretation. Tartu, 2008, 118 p.
80. **Valter Reedo.** Elaboration of IVB group metal oxide structures and their possible applications. Tartu, 2008, 98 p.
81. **Aleksei Kuznetsov.** Allosteric effects in reactions catalyzed by the cAMP-dependent protein kinase catalytic subunit. Tartu, 2009, 133 p.

82. **Aleksei Bredihhin.** Use of mono- and polyanions in the synthesis of multisubstituted hydrazine derivatives. Tartu, 2009, 105 p.
83. **Anu Ploom.** Quantitative structure-reactivity analysis in organosilicon chemistry. Tartu, 2009, 99 p.
84. **Argo Vonk.** Determination of adenosine A_{2A}- and dopamine D_1 receptor-specific modulation of adenylate cyclase activity in rat striatum. Tartu, 2009, 129 p.
85. **Indrek Kivi.** Synthesis and electrochemical characterization of porous cathode materials for intermediate temperature solid oxide fuel cells. Tartu, 2009, 177 p.
86. **Jaanus Eskusson.** Synthesis and characterisation of diamond-like carbon thin films prepared by pulsed laser deposition method. Tartu, 2009, 117 p.
87. **Marko Lätt.** Carbide derived microporous carbon and electrical double layer capacitors. Tartu, 2009, 107 p.
88. **Vladimir Stepanov.** Slow conformational changes in dopamine transporter interaction with its ligands. Tartu, 2009, 103 p.
89. **Aleksander Trummal.** Computational Study of Structural and Solvent Effects on Acidities of Some Brønsted Acids. Tartu, 2009, 103 p.
90. **Eerold Vellemäe.** Applications of mischmetal in organic synthesis. Tartu, 2009, 93 p.
91. **Sven Parkel.** Ligand binding to 5-HT_{1A} receptors and its regulation by Mg^{2+} and Mn^{2+}. Tartu, 2010, 99 p.
92. **Signe Vahur.** Expanding the possibilities of ATR-FT-IR spectroscopy in determination of inorganic pigments. Tartu, 2010, 184 p.
93. **Tavo Romann**. Preparation and surface modification of bismuth thin film, porous, and microelectrodes. Tartu, 2010, 155 p.
94. **Nadežda Aleksejeva.** Electrocatalytic reduction of oxygen on carbon nanotube-based nanocomposite materials. Tartu, 2010, 147 p.
95. **Marko Kullapere.** Electrochemical properties of glassy carbon, nickel and gold electrodes modified with aryl groups. Tartu, 2010, 233 p.
96. **Liis Siinor.** Adsorption kinetics of ions at Bi single crystal planes from aqueous electrolyte solutions and room-temperature ionic liquids. Tartu, 2010, 101 p.
97. **Angela Vaasa.** Development of fluorescence-based kinetic and binding assays for characterization of protein kinases and their inhibitors. Tartu 2010, 101 p.
98. **Indrek Tulp.** Multivariate analysis of chemical and biological properties. Tartu 2010, 105 p.
99. **Aare Selberg.** Evaluation of environmental quality in Northern Estonia by the analysis of leachate. Tartu 2010, 117 p.
100. **Darja Lavõgina.** Development of protein kinase inhibitors based on adenosine analogue-oligoarginine conjugates. Tartu 2010, 248 p.
101. **Laura Herm.** Biochemistry of dopamine D_2 receptors and its association with motivated behaviour. Tartu 2010, 156 p.

102. **Terje Raudsepp.** Influence of dopant anions on the electrochemical properties of polypyrrole films. Tartu 2010, 112 p.
103. **Margus Marandi.** Electroformation of Polypyrrole Films: *In-situ* AFM and STM Study. Tartu 2011, 116 p.
104. **Kairi Kivirand.** Diamine oxidase-based biosensors: construction and working principles. Tartu, 2011, 140 p.
105. **Anneli Kruve.** Matrix effects in liquid-chromatography electrospray mass-spectrometry. Tartu, 2011, 156 p.
106. **Gary Urb.** Assessment of environmental impact of oil shale fly ash from PF and CFB combustion. Tartu, 2011, 108 p.
107. **Nikita Oskolkov.** A novel strategy for peptide-mediated cellular delivery and induction of endosomal escape. Tartu, 2011, 106 p.
108. **Dana Martin.** The QSPR/QSAR approach for the prediction of properties of fullerene derivatives. Tartu, 2011, 98 p.
109. **Säde Viirlaid.** Novel glutathione analogues and their antioxidant activity. Tartu, 2011, 106 p.
110. **Ülis Sõukand.** Simultaneous adsorption of Cd^{2+}, Ni^{2+}, and Pb^{2+} on peat. Tartu, 2011, 124 p.
111. **Lauri Lipping.** The acidity of strong and superstrong Brønsted acids, an outreach for the "limits of growth": a quantum chemical study. Tartu, 2011, 124 p.
112. **Heisi Kurig.** Electrical double-layer capacitors based on ionic liquids as electrolytes. Tartu, 2011, 146 p.
113. **Marje Kasari.** Bisubstrate luminescent probes, optical sensors and affinity adsorbents for measurement of active protein kinases in biological samples. Tartu, 2012, 126 p.
114. **Kalev Takkis.** Virtual screening of chemical databases for bioactive molecules. Tartu, 2012, 122 p.
115. **Ksenija Kisseljova**. Synthesis of aza-β^3-amino acid containing peptides and kinetic study of their phosphorylation by protein kinase A. Tartu, 2012, 104 p.
116. **Riin Rebane.** Advanced method development strategy for derivatization LC/ESI/MS. Tartu, 2012, 184 p.
117. **Vladislav Ivaništšev.** Double layer structure and adsorption kinetics of ions at metal electrodes in room temperature ionic liquids. Tartu, 2012, 128 p.
118. **Irja Helm.** High accuracy gravimetric Winkler method for determination of dissolved oxygen. Tartu, 2012, 139 p.
119. **Karin Kipper.** Fluoroalcohols as Components of LC-ESI-MS Eluents: Usage and Applications. Tartu, 2012, 164 p.
120. **Arno Ratas.** Energy storage and transfer in dosimetric luminescent materials. Tartu, 2012, 163 p.
121. **Reet Reinart-Okugbeni**. Assay systems for characterisation of subtype-selective binding and functional activity of ligands on dopamine receptors. Tartu, 2012, 159 p.

122. **Lauri Sikk.** Computational study of the Sonogashira cross-coupling reaction. Tartu, 2012, 81 p.
123. **Karita Raudkivi.** Neurochemical studies on inter-individual differences in affect-related behaviour of the laboratory rat. Tartu, 2012, 161 p.
124. **Indrek Saar.** Design of GalR2 subtype specific ligands: their role in depression-like behavior and feeding regulation. Tartu, 2013, 126 p.
125. **Ann Laheäär.** Electrochemical characterization of alkali metal salt based non-aqueous electrolytes for supercapacitors. Tartu, 2013, 127 p.
126. **Kerli Tõnurist.** Influence of electrospun separator materials properties on electrochemical performance of electrical double-layer capacitors. Tartu, 2013, 147 p.
127. **Kaija Põhako-Esko.** Novel organic and inorganic ionogels: preparation and characterization. Tartu, 2013, 124 p.
128. **Ivar Kruusenberg.** Electroreduction of oxygen on carbon nanomaterial-based catalysts. Tartu, 2013, 191 p.
129. **Sander Piiskop.** Kinetic effects of ultrasound in aqueous acetonitrile solutions. Tartu, 2013, 95 p.
130. **Ilona Faustova**. Regulatory role of L-type pyruvate kinase N-terminal domain. Tartu, 2013, 109 p.
131. **Kadi Tamm.** Synthesis and characterization of the micro-mesoporous anode materials and testing of the medium temperature solid oxide fuel cell single cells. Tartu, 2013, 138 p.
132. **Iva Bozhidarova Stoyanova-Slavova.** Validation of QSAR/QSPR for regulatory purposes. Tartu, 2013, 109 p.
133. **Vitali Grozovski**. Adsorption of organic molecules at single crystal electrodes studied by *in situ* STM method. Tartu, 2014, 146 p.
134. **Santa Veikšina**. Development of assay systems for characterisation of ligand binding properties to melanocortin 4 receptors. Tartu, 2014, 151 p.
135. **Jüri Liiv.** PVDF (polyvinylidene difluoride) as material for active element of twisting-ball displays. Tartu, 2014, 111 p.
136. **Kersti Vaarmets.** Electrochemical and physical characterization of pristine and activated molybdenum carbide-derived carbon electrodes for the oxygen electroreduction reaction. Tartu, 2014, 131 p.
137. **Lauri Tõntson**. Regulation of G-protein subtypes by receptors, guanine nucleotides and Mn^{2+}. Tartu, 2014, 105 p.
138. **Aiko Adamson.** Properties of amine-boranes and phosphorus analogues in the gas phase. Tartu, 2014, 78 p.
139. **Elo Kibena**. Electrochemical grafting of glassy carbon, gold, highly oriented pyrolytic graphite and chemical vapour deposition-grown graphene electrodes by diazonium reduction method. Tartu, 2014, 184 p.
140. **Teemu Näykki.** Novel Tools for Water Quality Monitoring – From Field to Laboratory. Tartu, 2014, 202 p.
141. **Karl Kaupmees.** Acidity and basicity in non-aqueous media: importance of solvent properties and purity. Tartu, 2014, 128 p.

142. **Oleg Lebedev**. Hydrazine polyanions: different strategies in the synthesis of heterocycles. Tartu, 2015, 118 p.
143. **Geven Piir.** Environmental risk assessment of chemicals using QSAR methods. Tartu, 2015, 123 p.
144. **Olga Mazina.** Development and application of the biosensor assay for measurements of cyclic adenosine monophosphate in studies of G protein-coupled receptor signalinga. Tartu, 2015, 116 p.
145. **Sandip Ashokrao Kadam.** Anion receptors: synthesis and accurate binding measurements. Tartu, 2015, 116 p.
146. **Indrek Tallo.** Synthesis and characterization of new micro-mesoporous carbide derived carbon materials for high energy and power density electrical double layer capacitors. Tartu, 2015, 148 p.
147. **Heiki Erikson.** Electrochemical reduction of oxygen on nanostructured palladium and gold catalysts. Tartu, 2015, 204 p.
148. **Erik Anderson.** *In situ* Scanning Tunnelling Microscopy studies of the interfacial structure between Bi(111) electrode and a room temperature ionic liquid. Tartu, 2015, 118 p.
149. **Girinath G. Pillai.** Computational Modelling of Diverse Chemical, Biochemical and Biomedical Properties. Tartu, 2015, 140 p.
150. **Piret Pikma.** Interfacial structure and adsorption of organic compounds at Cd(0001) and Sb(111) electrodes from ionic liquid and aqueous electrolytes: an *in situ* STM study. Tartu, 2015, 126 p.
151. **Ganesh babu Manoharan.** Combining chemical and genetic approaches for photoluminescence assays of protein kinases. Tartu, 2016, 126 p.
152. **Carolin Siimenson**. Electrochemical characterization of halide ion adsorption from liquid mixtures at Bi(111) and pyrolytic graphite electrode surface. Tartu, 2016, 110 p.
153. **Asko Laaniste.** Comparison and optimisation of novel mass spectrometry ionisation sources. Tartu, 2016, 156 p.
154. **Hanno Evard.** Estimating limit of detection for mass spectrometric analysis methods. Tartu, 2016, 224 p.
155. **Kadri Ligi.** Characterization and application of protein kinase-responsive organic probes with triplet-singlet energy transfer. Tartu, 2016, 122 p.
156. **Margarita Kagan.** Biosensing penicillins' residues in milk flows. Tartu, 2016, 130 p.
157. **Marie Kriisa.** Development of protein kinase-responsive photoluminescent probes and cellular regulators of protein phosphorylation. Tartu, 2016, 106 p.
158. **Mihkel Vestli.** Ultrasonic spray pyrolysis deposited electrolyte layers for intermediate temperature solid oxide fuel cells. Tartu, 2016, 156 p.
159. **Silver Sepp**. Influence of porosity of the carbide-derived carbon on the properties of the composite electrocatalysts and characteristics of polymer electrolyte fuel cells. Tartu, 2016, 137 p.
160. **Kristjan Haav**. Quantitative relative equilibrium constant measurements in supramolecular chemistry. Tartu, 2017, 158 p.

161. **Anu Teearu**. Development of MALDI-FT-ICR-MS methodology for the analysis of resinous materials. Tartu, 2017, 205 p.
162. **Taavi Ivan**. Bifunctional inhibitors and photoluminescent probes for studies on protein complexes. Tartu, 2017, 140 p.
163. **Maarja-Liisa Oldekop**. Characterization of amino acid derivatization reagents for LC-MS analysis. Tartu, 2017, 147 p.
164. **Kristel Jukk**. Electrochemical reduction of oxygen on platinum- and palladium-based nanocatalysts. Tartu, 2017, 250 p.
165. **Siim Kukk**. Kinetic aspects of interaction between dopamine transporter and *N*-substituted nortropane derivatives. Tartu, 2017, 107 p.
166. **Birgit Viira**. Design and modelling in early drug development in targeting HIV-1 reverse transcriptase and Malaria. Tartu, 2017, 172 p.
167. **Rait Kivi**. Allostery in cAMP dependent protein kinase catalytic subunit. Tartu, 2017, 115 p.
168. **Agnes Heering**. Experimental realization and applications of the unified acidity scale. Tartu, 2017, 123 p.
169. **Delia Juronen**. Biosensing system for the rapid multiplex detection of mastitis-causing pathogens in milk. Tartu, 2018, 85 p.
170. **Hedi Rahnel.** ARC-inhibitors: from reliable biochemical assays to regulators of physiology of cells. Tartu, 2018, 176 p.
171. **Anton Ruzanov.** Computational investigation of the electrical double layer at metal–aqueous solution and metal–ionic liquid interfaces. Tartu, 2018, 129 p.
172. **Katrin Kestav.** Crystal Structure-Guided Development of Bisubstrate-Analogue Inhibitors of Mitotic Protein Kinase Haspin. Tartu, 2018, 166 p.
173. **Mihkel Ilisson.** Synthesis of novel heterocyclic hydrazine derivatives and their conjugates. Tartu, 2018, 101 p.
174. **Anni Allikalt.** Development of assay systems for studying ligand binding to dopamine receptors. Tartu, 2018, 160 p.
175. **Ove Oll.** Electrical double layer structure and energy storage characteristics of ionic liquid based capacitors. Tartu, 2018, 187 p.
176. **Rasmus Palm.** Carbon materials for energy storage applications. Tartu, 2018, 114 p.
177. **Jörgen Metsik.** Preparation and stability of poly(3,4-ethylenedioxythiophene) thin films for transparent electrode applications. Tartu, 2018, 111 p.
178. **Sofja Tšepelevitš.** Experimental studies and modeling of solute-solvent interactions. Tartu, 2018, 109 p.
179. **Märt Lõkov.** Basicity of some nitrogen, phosphorus and carbon bases in acetonitrile. Tartu, 2018, 104 p.
180. **Anton Mastitski**. Preparation of α-aza-amino acid precursors and related compounds by novel methods of reductive one-pot alkylation and direct alkylation. Tartu, 2018, 155 p.
181. **Jürgen Vahter**. Development of bisubstrate inhibitors for protein kinase CK2. Tartu, 2019, 186 p.

182. **Piia Liigand.** Expanding and improving methodology and applications of ionization efficiency measurements. Tartu, 2019, 189 p.
183. **Sigrid Selberg.** Synthesis and properties of lipophilic phosphazene-based indicator molecules. Tartu, 2019, 74 p.
184. **Jaanus Liigand.** Standard substance free quantification for LC/ESI/MS analysis based on the predicted ionization efficiencies. Tartu, 2019, 254 p.
185. **Marek Mooste.** Surface and electrochemical characterisation of aryl film and nanocomposite material modified carbon and metal-based electrodes. Tartu, 2019, 304 p.
186. **Mare Oja.** Experimental investigation and modelling of pH profiles for effective membrane permeability of drug substances. Tartu, 2019, 306 p.
187. **Sajid Hussain.** Electrochemical reduction of oxygen on supported Pt catalysts. Tartu, 2019, 220 p.
188. **Ronald Väli.** Glucose-derived hard carbon electrode materials for sodium-ion batteries. Tartu, 2019, 180 p.
189. **Ester Tee.** Analysis and development of selective synthesis methods of hierarchical micro- and mesoporous carbons. Tartu, 2019, 210 p.
190. **Martin Maide.** Influence of the microstructure and chemical composition of the fuel electrode on the electrochemical performance of reversible solid oxide fuel cell. Tartu, 2020, 144 p.
191. **Edith Viirlaid.** Biosensing Pesticides in Water Samples. Tartu, 2020, 102 p.
192. **Maike Käärik.** Nanoporous carbon: the controlled nanostructure, and structure-property relationships. Tartu, 2020, 162 p.
193. **Artur Gornischeff.** Study of ionization efficiencies for derivatized compounds in LC/ESI/MS and their application for targeted analysis. Tartu, 2020, 124 p.
194. **Reet Link.** Ligand binding, allosteric modulation and constitutive activity of melanocortin-4 receptors. Tartu, 2020, 108 p.
195. **Pilleriin Peets.** Development of instrumental methods for the analysis of textile fibres and dyes. Tartu, 2020, 150 p.
196. **Larisa Ivanova.** Design of active compounds against neurodegenerative diseases. Tartu, 2020, 152 p.
197. **Meelis Härmas.** Impact of activated carbon microstructure and porosity on electrochemical performance of electrical double-layer capacitors. Tartu, 2020, 122 p.
198. **Ruta Hecht.** Novel Eluent Additives for LC-MS Based Bioanalytical Methods. Tartu, 2020, 202 p.
199. **Max Hecht.** Advances in the Development of a Point-of-Care Mass Spectrometer Test. Tartu, 2020, 168 p.
200. **Ida Rahu.** Bromine formation in inorganic bromide/nitrate mixtures and its application for oxidative aromatic bromination. Tartu, 2020, 116 p.
201. **Sander Ratso**. Electrocatalysis of oxygen reduction on non-precious metal catalysts. Tartu, 2020, 371 p.
202. **Astrid Darnell.** Computational design of anion receptors and evaluation of host-guest binding. Tartu, 2021, 150 p.

203. **Ove Korjus.** The development of ceramic fuel electrode for solid oxide cells. Tartu, 2021, 150 p.
204. **Merit Oss.** Ionization efficiency in electrospray ionization source and its relations to compounds' physico-chemical properties. Tartu, 2021, 124 p.
205. **Madis Lüsi**. Electroreduction of oxygen on nanostructured palladium catalysts. Tartu, 2021, 180 p.
206. **Eliise Tammekivi.** Derivatization and quantitative gas-chromatographic analysis of oils. Tartu, 2021, 122 p.
207. **Simona Selberg.** Development of Small-Molecule Regulators of Epi-transcriptomic Processes. Tartu, 2021, 122 p.
208. **Olivier Etebe Nonga.** Inhibitors and photoluminescent probes for in vitro studies on protein kinases PKA and PIM. Tartu, 2021, 189 p.
209. **Riinu Härmas.** The structure and H2 diffusion in porous carbide-derived carbon particles. Tartu, 2022, 123 p.
210. **Maarja Paalo.** Synthesis and characterization of novel carbon electrodes for high power density electrochemical capacitors. Tartu, 2022, 144 p.
211. **Jinfeng Zhao.** Electrochemical characteristics of Bi(hkl) and micro-meso-porous carbon electrodes in ionic liquid based electrolytes. Tartu, 2022, 134 p.
212. **Alar Heinsaar.** Investigation of oxygen electrode materials for high-temperature solid oxide cells in natural conditions. Tartu, 2022, 120 p.
213. **Jaana Lilloja.** Transition metal and nitrogen doped nanocarbon cathode catalysts for anion exchange membrane fuel cells. Tartu, 2022, 202 p.
214. **Maris-Johanna Tahk.** Novel fluorescence-based methods for illuminating transmembrane signal transduction by G-protein coupled receptors. Tartu, 2022, 200 p.
215. **Eerik Jõgi.** Development and Applications of E. coli Immunosensor. Tartu, 2022, 103 p.
216. **Alo Rüütel.** Design principles of synthetic molecular receptors for anion-selective electrodes. Tartu, 2022, 109 p.
217. **Tanel Sõrmus.** Development of stimuli-responsive and covalent bisubstrate inhibitors of protein kinases. Tartu, 2022, 148 p.
218. **Oleg Artemchuk.** Autotrophic nitrogen removal processes for nutrient removal from sidestream and mainstream wastewater. Tartu, 2022, 115 p.
219. **Andre Leesment.** Quantitative studies of Brønsted acidity in biphasic systems and gas-phase. Tartu, 2023, 83 p.
220. **Meeli Arujõe-Sado.** Structural effects in aza-peptide bond formation reaction. Tartu, 2023, 83 p.
221. **Jonas Mart Linge.** Electrochemical reduction of oxygen on silver-based catalysts. Tartu, 2023, 269 p.
222. **Tõnis Laasfeld.** Integrating Image Analysis and Quantitative Modeling for a Holistic View of GPCR Ligand Binding Dynamics. Tartu, 2023, 226 p.
223. **Ernesto de Jesus Zapata Flores.** Derivatization Reagents used in negative mode electrospray LC-MS. Tartu, 2023, 107 p.

224. **Patrick Teppor.** Obtaining platinum-free oxygen reduction catalysts through biomass valorization: a case study of peat. Tartu, 2023, 161 p.
225. **Peeter Valk.** Methanol Oxidation on Platinum-Rare-Earth Metal Oxide Activated Catalysts. Tartu, 2023, 162 p.
226. **Shidong Chen.** Unravelling prehistoric plant exploitation in eastern Baltic: organic residue analysis of plant-based materials by multi-method approach. Tartu, 2023, 245 p.
227. **Yogesh Kumar.** M-N_4 macrocycle-based catalysts for electrocatalysis of oxygen reduction and oxygen evolution. Tartu, 2023, 224 p.
228. **Kerli Martin.** Recognition of carboxylates by synthetic receptors – from structure-affinity studies to solid-contact anion-selective electrode prototyping. Tartu, 2024, 130 p.
229. **Huy Quí Vinh Nguyen.** Development of Carbon Supported Pt–CeO_2 Catalysts for Proton Exchange Membrane Fuel Cells. Tartu, 2024, 198 p.
230. **Heigo Ers**. Adsorption and Structuring Processes at Single Crystal Electrode – Ionic Liquid Interface – Insights from Simulations and *in situ* Studies. Tartu, 2024, 137 p.
231. **Ritums Cepitis.** Modelling Structural and Geometrical Effects in Carbon Dioxide and Oxygen Electrocatalysis. Tartu, 2024, 99 p.
232. **Kaarel Kisand.** Resorcinol-derived carbon-based catalysts for polymer electrolyte fuel cell cathodes. Tartu, 2024, 205 p.
233. **Akmal Kosimov**. Template-assisted Mechanosynthesis (TAMS) for the production of bifunctional transition metal-based catalysts. Tartu, 2024, 123 p.
234. **Larissa Silva Macieli.** Derivatization-targeted LC-MS analysis of compounds containing amino group. Tartu, 2024, 157 p.
235. **Silvester Jürjo.** Separation of rare earth elements from Estonian phosphorite ore using liquid extraction followed by electrochemical reduction. Tartu, 2024, 99 p.
236. **Jan-Michael C. Cayme.** Organic-inorganic interactions in experimental and archaeological ceramics. Tartu, 2025, 156 p.
237. **Miriam Koppel.** The diffusion of H2 adsorbed in carbide-derived carbons: a quasi-elastic neutron scattering study. Tartu, 2025, 138 p.
238. **Kenneth Tuul.** Evaluating lithium-ion pouch cells and hydrogen storage materials under extreme conditions using advanced techniques. Tartu, 2025, 188 p.
239. **Marta-Lisette Pikma.** Exploring the basicity of phosphanes and related compounds. Tartu, 2025, 100 p.
240. **Indrek Saar.** Development of novel on-site chemical analysis tests – from alternative materials and technologies to functional prototypes. Tartu, 2025, 214 p.
241. **Gulnara Yusibova.** TAL MOF-Derived M-N-C Electrocatalysts for Oxygen Reduction and Evolution Reactions. Tartu, 2025, 120 p.

242. **Karl Marti Toots.** Cheminformatics Approaches for Analyzing and Modeling the Gas-Ionic Liquid Distribution of Organic Solutes. Tartu, 2025, 249 p.
243. **Freddy Kukk.** Electrochemical Characterization of Structurally and Chemically Modified Solid Oxide Cells Operated in Electrolysis Mode. Tartu, 2026, 142 p.
244. **Shrikant Shivaji Pawade.** Metrological Aspects of Sampling and Water/ Moisture Determination on the Example of Lignin. Tartu, 2026, 146 p.
245. **Raegan Danielle Chambers.** Electrocatalysis of oxygen reduction on Pt nanoparticles deposited on novel support materials. Tartu, 2026, 172 p.
246. **John Paulo Aquino Samin.** Unified pH in aqueous-organic solvent mixtures and low-polarity solvents. Tartu, 2026, 132 p.